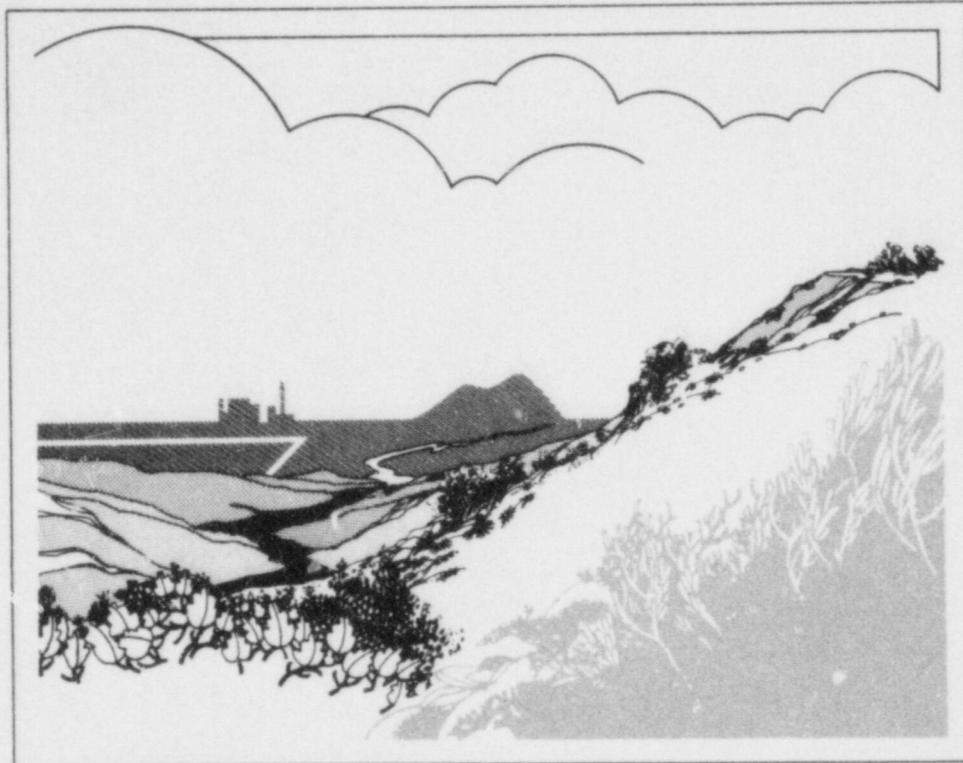


# An Assessment of Hydrogen Generation for the PBF Severe Fuel Damage Scoping and 1-1 Tests

NUREG/CR-4866  
EGG-2499  
April 1987

August W. Cronenberg  
Richard W. Miller  
Daniel J. Osetek

F O R M A L R E P O R T



**Idaho National  
Engineering Laboratory**

*Managed by the U.S. Department of Energy*



Work performed under  
DOE Contract No. DE-AC07-76ID01570

for the **U.S. Nuclear  
Regulatory Commission**

870612016B 870430  
PDR NUREG  
CR-4866 R PDR

Available from

Superintendent of Documents  
U.S. Government Printing Office  
Post Office Box 37082  
Washington, D.C. 20013-7982

and

National Technical Information Service  
Springfield, VA 22161

#### NOTICE

This report was prepared as an account of work sponsored by an agency of the United States Government. Neither the United States Government nor any agency thereof, nor any of their employees, makes any warranty, expressed or implied, or assumes any legal liability or responsibility for any third party's use, or the results of such use, of any information, apparatus, product or process disclosed in this report, or represents that its use by such third party would not infringe privately owned rights.



# **AN ASSESSMENT OF HYDROGEN GENERATION FOR THE PBF SEVERE FUEL DAMAGE SCOPING AND 1-1 TESTS**

August W. Cronenberg<sup>a</sup>  
Richard W. Miller  
Daniel J. Osetek

Published April 1987

EG&G Idaho, Inc.  
Idaho Falls, Idaho 83415

Prepared for the  
Division of Accident Evaluation  
Office of Nuclear Regulatory Research  
U. S. Nuclear Regulatory Commission  
Washington, D.C. 20555  
Under DOE Contract No. DE-AC07-761D01570  
FIN No. A6321

---

a. ESA, Inc., 836 Claire View Lane, Idaho Falls, ID 83402

## ABSTRACT

An evaluation of zircaloy oxidation and hydrogen generation data is presented for the first two Severe Fuel Damage (SFD) tests, conducted in the Power Burst Facility at the Idaho National Engineering Laboratory. This work is in support of an internationally sponsored severe accident research program, initiated by the U. S. Nuclear Regulatory Commission to advance the understanding and methodology for predicting light water reactor core degradation, hydrogen generation, and fission product behavior during severe accidents. The principal objective of this report is an assessment of in-vessel hydrogen generation issues using data provided by the SFD Scoping Test (SFD-ST) and SFD 1-1 test. The principal issues in question are the influence of zircaloy melting on oxidation behavior and fuel bundle reconfiguration effects which may alter steam flow and hydrogen generation characteristics.

A comparison of the  $H_2$  generation and cladding thermocouple data indicates that a significant amount of hydrogen was produced after the initiation of zircaloy melt-induced fuel dissolution at temperatures above 2170 K. Posttest metallographic observations indicate a high degree of oxidation of previously molten zircaloy-bearing debris, which corroborates the trend of the on-line data. Analyses also indicate that essentially complete flow area blockage ( $> 98\%$ ) would be required to diminish steam flow through the degraded test bundle so as to reduce hydrogen production. Neither on-line data nor posttest examination of the fuel bundles from the SFD-ST and SFD 1-1 tests indicate that such extreme flow area blockages occurred.

For the steam-rich SFD-ST experiment,  $UO_2$  fuel oxidation was also observed, which could have accounted for approximately 20% of the total hydrogen production. Fuel oxidation has also been noted from retrieved TMI-2 core debris samples. Thus, oxidation of  $UO_2$  to a hypostoichiometric condition may add to the total hydrogen burden for severe accidents.



## EXECUTIVE SUMMARY

During the Three Mile Island Unit 2 (TMI-2) accident, approximately 500 kg of hydrogen gas ( $H_2$ ) were generated, equivalent to full oxidation of about half the core inventory of zircaloy cladding. Although the TMI-2 containment survived a  $H_2$  burn without loss of integrity, the accident demonstrated that large quantities of  $H_2$  can be generated during severe accidents. In response to this accident, the United States Nuclear Regulatory Commission (NRC) initiated an internationally sponsored<sup>a</sup> research program on severe core damage for light water reactors (LWRs). One of the objectives of the NRC severe fuel damage (SFD) program is to obtain hydrogen generation data under prototypic accident conditions, which can be used to verify predictive mechanistic models that reflect governing phenomena. A major portion of the NRC-SFD in-pile experiments program involves the four SFD tests that were conducted in the Power Burst Facility (PBF) at the Idaho National Engineering Laboratory (INEL) during the period from October 1982 to February 1985. Although actual testing has been completed, posttest metallographic data on the nature and extent of zircaloy oxidation are now available only for the first two tests. Since such metallographic data are important to the final assay of bundle oxidation behavior, this report is limited to a discussion of the first two tests for which all data are now available, namely the Scoping Test (SFD-ST) and SFD 1-1.

The data from the first two tests are assessed here with respect to in-vessel processes affecting the hydrogen source term, where the principal outstanding issues concern (a) the effect of zircaloy melting and relocation on oxidation behavior, and (b) fuel bundle reconfiguration effects, which may alter steam flow and hydrogen generation characteristics. Observations from the SFD-ST and SFD 1-1 data relative to these issues can be summarized as follows.

---

a. Partners in the program include Belgium, Canada, Federal Republic of Germany, Italy, Japan, Netherlands, Republic of Korea, Spain, Sweden, United Kingdom, American Institute of Taiwan, and the United States Nuclear Regulatory Commission.

### Oxidation Behavior of Molten Zircaloy

The prediction of oxidation behavior after the initiation of zircaloy melting and  $UO_2$  dissolution (at  $\sim 2170$  K) is an unresolved issue and a principal point of interest in the assessment of the PBF-SFD test data. Specific information on the kinetics of molten zircaloy oxidation, oxidation during melt relocation, and the kinetics of molten zircaloy dissolution of  $UO_2$  cannot be obtained from the integral PBF-SFD experiments. However, gross changes in oxidation/hydrogen generation behavior after the onset of fuel dissolution can be assessed from a comparison of the measured on-line hydrogen generation with cladding thermocouple data. Additional insight on governing phenomena can also be obtained from posttest metallographic inspection of previously molten zircaloy-bearing test debris.

A best-estimate comparison of the  $H_2$  release and cladding thermocouple data for the SFD-ST experiment indicates that about 25-40% of the total hydrogen generated occurred after initiation of zircaloy melting and fuel dissolution ( $\sim 2170$  K). For the SFD 1-1 test, a hydrogen generation fraction prior to the onset of fuel dissolution of approximately 15% was obtained, the remaining 85% occurring after initiation of fuel dissolution. Post-test metallographic examinations show extensive oxidation of previously molten zircaloy-bearing test debris by steam for both tests, which corroborates the trend of the on-line, time-dependent data. The PBF SFD-ST and SFD 1-1 test data thus do not indicate a cutoff or severely diminished  $H_2$  production process upon initiation of zircaloy melting and fuel dissolution.

The difference in partitioning of  $H_2$  generation between the two tests is largely related to steam supply conditions. For the steam-rich SFD-ST experiment, oxidation over the entire bundle occurred during heatup. For the steam-starved SFD 1-1 test, oxidation

was limited to a local region of the bundle during bundle heatup, leaving a significant portion of the zircaloy relatively unoxidized after 2170 K was reached, and thus available for later reaction with steam.

## Flow Blockage/Steam Diversion Effects

It has been suggested by the Industry Degraded Core Rulemaking (IDCOR)<sup>a</sup> program that, due to fuel liquefaction at temperatures above 2170 K, loss of rod geometry in canned boiling water reactor (BWR) fuel assemblies results in fuel assembly blockage, sufficient in extent to cause steam pressurization below the blockage region and attendant coolant diversion to adjacent undamaged assemblies. Hydrogen production in a degraded BWR fuel bundle is thereby postulated to be substantially reduced or terminated above 2170 K.

Posttest inspections of the SFD-ST and SFD 1-1 test degraded fuel bundles indicate only partial flow area blockage. Analysis of bundle pressurization/flow diversion potential indicates that near-total flow area blockage (>98%) would be required to cause pressurization at the inlet of the degraded SFD-ST and SFD 1-1 test bundles. Such large-scale blockage conditions are not supported by the SFD-ST and SFD 1-1 posttest bundle examinations. Analysis also indicates

that steam flow may tend to cause hydrodynamic breakup of relocating molten zircaloy, thereby delaying or preventing complete flow area blockage. Likewise, the SFD 1-1 data indicate asymmetric bundle heatup conditions which appear exacerbated by the autocatalytic nature of the zircaloy oxidation process. Such asymmetry in bundle heatup can lead to incoherency of zircaloy melting, fuel dissolution, and debris relocation. It should be cautioned that although complete flow area blockages did not occur in the SFD-ST and SFD 1-1 tests, such limited blockage data do not prove that complete blockages in BWR fuel assemblies can never occur. Nevertheless, the SFD-ST and SFD 1-1 data do call into question the IDCOR presumption that complete flow area blockages always occur in BWR canned fuel assemblies upon melt relocation.

The argument for blockage and flow diversion in BWR cores also requires that the BWR fuel assembly channel wall remain intact. Evidence from the SFD-ST and SFD 1-1 tests, however, indicates that a BWR zircaloy channel wall may experience oxidation-driven heatup and failure similar to the cladding. The SFD bundles were shrouded in a 0.76-mm (~0.03-in.) thick zircaloy liner which was instrumented with thermocouples. Test data indicate that the liner experienced oxidation-driven heatup similar to the test fuel rods. Posttest metallographic examination of the liner also indicated melt failure and extensive oxidation of the liner material. The SFD-ST and SFD 1-1 observations on bundle liner behavior indicate that BWR channel wall failure may occur during severe accident boiloff sequences. Failure of the fuel assembly wall would diminish or negate flow diversion in BWR core geometries and allow coolant to reenter the flow channels and promote further oxidation.

---

a. The IDCOR program is an independent technical effort sponsored by the commercial nuclear power industry under the corporate auspices of the Atomic Industrial Forum. The purpose of this program is to develop a technical position to assist in deciding whether or not changes in licensing regulations are needed to reflect degraded core or core melt accidents.



## **ACKNOWLEDGMENTS**

The authors gratefully acknowledge the Severe Accident Research staff of EG&G Idaho, Inc., particularly B. A. Cook, D. A. Petti, and Z. R. Martinson, for their helpful discussions. The authors also express their appreciation to Dr. A. Knipe, Winfrith Atomic Energy Establishment, United Kingdom; Prof. D. Olander, of the University of California at Berkeley; and Dr. M. Picklesimer, consultant, for their review of this report.

# CONTENTS

ABSTRACT .....	ii
EXECUTIVE SUMMARY .....	iii
ACKNOWLEDGMENTS .....	v
INTRODUCTION .....	1
The PBF-SFD Test Program .....	2
SFD SCOPING TEST RESULTS .....	6
Test Conduct .....	6
On-Line Hydrogen Data .....	8
Thermocouple Data .....	11
Summary of Posttest Bundle Examination Data .....	13
Bundle Geometric Characteristics .....	13
Bundle Oxidation Characteristics .....	13
Code-Predicted Oxidation Behavior .....	15
SFD 1-1 TEST RESULTS .....	22
Test Conduct .....	22
On-Line Hydrogen Data .....	24
Thermocouple Data .....	27
Summary of Posttest Bundle Examination Data .....	29
Bundle Geometric Characteristics .....	29
Bundle Oxidation Characteristics .....	30
Code-Predicted Oxidation Behavior .....	32
SCDAP Predictions .....	32
MAAP Predictions .....	32
ANALYSIS OF THE SFD-ST AND SFD 1-1 HYDROGEN GENERATION DATA .....	38
Perspective on Hydrogen Source Term Issues .....	38
Oxidation Behavior of Molten Zircaloy .....	39
Fuel Bundle Reconfiguration Effects .....	43
Evaluation of the SFD-ST and SFD 1-1 Test Data .....	43



Oxidation Behavior of Molten Zircaloy .....	43
Fuel Bundle Reconfiguration Effects in BWRs .....	47
SUMMARY AND CONCLUSIONS .....	60
REFERENCES .....	62
APPENDIX A—ILLUSTRATIVE CALCULATIONS .....	A-1
APPENDIX B—DISCUSSION OF FLOW PERTURBATIONS DURING THE SFD-ST TRANSIENT .....	B-1
APPENDIX C—OXIDATION OF RELOCALIZED ZIRCALOY MELT .....	C-1

## FIGURES

1. Illustration of the SFD fuel bundle geometry and fission product monitoring system (not to scale) .....	4
2. Axial view of the SFD-ST test train components .....	7
3. Bundle nuclear power and system pressure for Test SFD-ST .....	9
4. Coolant liquid level and flow rate for Test SFD-ST .....	9
5. Comparison of SFD-ST fuel Rod D3 cladding temperatures at three axial locations .....	10
6. SFD-ST on-line in-bundle hydrogen generation behavior, adjusted for transport delay to the hydrogen monitor .....	11
7. Radially averaged thermocouple measurements of SFD-ST cladding and fuel centerline temperatures .....	12
8. Metallographic cross section of the SFD-ST bundle at the 0.170-m elevation .....	14
9. Comparison of the SFD-ST integrated on-line measurement of hydrogen release and estimates from posttest metallographic examination .....	16
10. Illustration of oxidation behavior of previously molten metallic SFD-ST debris which froze in the spacing between two ballooned cladding remnants at the 0.495-m elevation .....	17
11. Evidence of SFD-ST metallic melt penetration into a $\text{UO}_2$ fuel pellet crack at the 0.495-m elevation, where the melt subsequently froze and oxidized .....	18
12. Posttest SFD-ST fuel debris, indicating $\text{UO}_2$ oxidation to $\text{U}_4\text{O}_9$ precipitates .....	19
13. Comparison of the SFD-ST measured and SCDAP-calculated two-phase/steam interface elevation .....	19

14. Comparison of the SFD-ST measured and SCDAP-calculated cladding temperatures at three axial elevations .....	20
15. Test SFD 1-1 thermal-hydraulic conditions .....	23
16. Test SFD 1-1 bundle fission power and cladding temperature histories at the 0.35-m elevation .....	24
17. Test SFD 1-1 on-line in-bundle hydrogen generation behavior, adjusted for transport delay to the hydrogen monitor .....	25
18. Schematic of SFD 1-1 upper test train showing the stagnant volume which may have retained hydrogen .....	26
19. Comparison of the SFD 1-1 measured and SCDAP-calculated cladding temperatures at the 0.35-, 0.5-, and 0.7-m elevations .....	28
20. Comparison of the SFD 1-1 measured cladding and fuel centerline temperatures on Rod 4B at the 0.70-m elevation .....	29
21. SFD 1-1 measured cladding temperatures on Rod 3F .....	30
22. Posttest metallographic cross section of the SFD 1-1 bundle at 0.066 m .....	31
23. Illustration of deformed Rod 6D SFD 1-1 cladding and liner remnants at the 0.117-m elevation, where the fuel and oxidized cladding are shown to be partially dissolved by the previously molten metallic debris that has been oxidized by steam to a ceramic condition .....	33
24. Illustration of MAAP core geometry models for BWR and PWR systems .....	35
25. Comparison of SFD 1-1 measured and MAAP-calculated water level and cladding temperatures .....	37
26. Zirconium-oxygen equilibrium and pseudo-binary $\alpha$ -Zr(O)- $\text{UO}_2$ phase diagrams .....	40
27. Comparison of parabolic growth-rate constants for oxide-layer growth .....	41
28. Temperature dependence of the oxygen diffusivity in $\alpha$ -Zr(O) and $\text{ZrO}_2$ (Reference 27) ....	42
29. Illustration of potential enhanced oxidation due to exposure of molten $\alpha$ -Zr(O) to steam .....	44
30. Illustration of the IDCOR MAAP-BWR fuel assembly blockage/flow diversion model .....	45
31. Comparison of the SFD-ST thermocouple and best-estimate $\text{H}_2$ generation data, to assess $\text{H}_2$ partitioning before and after the initiation of $\alpha$ -Zr(O)/ $\text{UO}_2$ eutectic melting at 2170 K .....	46
32. Comparison of the SFD 1-1 thermocouple and on-line $\text{H}_2$ generation data, to assess $\text{H}_2$ partitioning before and after the initiation of $\alpha$ -Zr(O)/ $\text{UO}_2$ eutectic melting at 2170 K .....	47
33. Illustration of isentropic compressible flow through a blockage orifice .....	49



34. Comparison of flow area degradation in the SFD-ST and SFD 1-1 test bundles .....	50
35. Illustration of flooding-induced breakup of relocating melt debris .....	51
36. Illustration of asymmetric rod temperature conditions in the SFD 1-1 test bundle .....	53
37. Illustration of bypass flow area effects on bundle pressurization .....	54
38. Comparison of SFD-ST shroud liner and radially averaged fuel cladding temperatures at the 0.7-m elevation .....	55
39. Comparison of SFD 1-1 shroud liner and cladding temperatures at the 0.5-m elevation .....	55
40. Metallographic cross sections of the SFD-ST bundle at the 0.17- and 0.245-m elevations indicating liner failure above and at the maximum blockage location .....	57
41. Dissolution of the oxidized SFD 1-1 liner on the inner surface by a metallic (U,Zr,O) melt at the 0.066-m elevation .....	58
42. Illustration of reestablished steam flow through a failed channel wall in a degraded/blocked BWR fuel assembly .....	59
B-1. Comparison of the SFD-ST bundle differential temperature and signal from melt-through detector .....	B-4
B-2. The SFD-ST two-phase/steam interface level at the time of shroud failure .....	B-5
B-3. SFD-ST Rod 3D thermocouple response at the time of shroud failure .....	B-6
B-4. SFD-ST measured on-line hydrogen release rate .....	B-7
B-5. Bundle differential pressure, inlet flow rate, and separator pressure during the final phase of the SFD-ST transient .....	B-7
C-1. Intact section of cladding before $\alpha$ -Zr(O) melting and relocated refrozen $\alpha$ -Zr(O) at lower elevation .....	C-4
C-2. Illustration of oxygen diffusion problem for oxidatics of relocated $\alpha$ -Zr(O) .....	C-5

## TABLES

1. Inventory of containment types .....	2
2. The PBF severe fuel damage test series .....	3
3. Nominal design characteristics for SFD-ST .....	8
4. Potential SFD-ST sources of hydrogen generation and metallographic results .....	14
5. Estimated mass of hydrogen trapped in dead space above the fallback barrier .....	27

6. Potential sources of hydrogen generation and metallographic results for Test SFD 1-1 .....	31
7. Comparison of measured and SCDAP-calculated results .....	34
8. Arrhenius correlations for the parabolic rate constant .....	39
9. Thermophysical properties of zircaloy cladding .....	41
10. Arrhenius equations for oxygen diffusivity in zircaloy .....	42
11. Summary of zircaloy oxidation and hydrogen generation behavior noted in the PBF SFD-ST and SFD 1-1 experiments .....	61
A-1. Estimated steam-starvation height for the SFD-ST test conditions .....	A-4
A-2. Estimated steam-starvation height for the SFD 1-1 test conditions .....	A-5
A-3. Assessment of the differential pressure for steam removal capacity through a constricted orifice .....	A-6
A-4. Estimate of the flooding conditions for breakup of a liquid zircaloy film .....	A-7
A-5. Assessment of single-phase differential pressure for steam removal capacity through the constricted region of the SFD-ST bundle .....	A-8
C-1 Evaluation of the effect of oxygen content on the growth rate constant .....	C-5

# AN ASSESSMENT OF HYDROGEN GENERATION FOR THE PBF SEVERE FUEL DAMAGE SCOPING AND 1-1 TESTS

## INTRODUCTION

Zircaloy oxidation and attendant hydrogen generation in both the TMI-2 and Chernobyl accidents has increased awareness that large amounts of hydrogen ( $H_2$ ) can be released during severe accidents. For the TMI-2 accident, it has been estimated that about 500 kg of hydrogen<sup>1,2</sup> were generated, equivalent to full oxidation of about one-half the available core inventory of zircaloy cladding. Approximately 270 kg of  $H_2$  burned in the containment building, resulting in a 28-psi pressure rise. (The TMI-2 containment design pressure is 60 psi.) Although TMI-2 containment integrity was maintained, such was not the case at Chernobyl. Preliminary observations on the Chernobyl accident<sup>3,4</sup> indicate that failure of the reactor building occurred as a consequence of rapid steam pressurization due to a reactivity-initiated fuel-coolant thermal interaction, a hydrogen-air explosion, or a combination of both. Potentially large quantities of hydrogen could have been generated in this accident, due to the oxidation of the zircaloy fuel cladding and pressure tubes that comprise approximately 100 tons of core material, as compared to about 20 tons of zircaloy in typical PWRs. Loss of the low-pressure containment structure at Chernobyl resulted in release of radioactive fission products and site worker fatalities.

Such accidents emphasize the importance that hydrogen generation can exert on accident consequences. Uncertainty concerning the timing and rate of hydrogen evolution, as well as the maximum quantity of hydrogen produced, leads to large uncertainties relative to containment failure probabilities for severe accident sequences. Containment designs for U. S. nuclear plants can be classified into three major categories relative to their capability to accommodate large-scale hydrogen release and subsequent deflagrations.<sup>5</sup> These categories are listed in Table 1 for operating and future plants.

The small containments include the Mark-I and Mark-II BWR designs; however, hydrogen combustion is precluded for these containments since they are inerted. Because of the relatively high design pressures and large volumes, no near-term mitiga-

tion measures are likewise being required for hydrogen control in large dry containments. The issue of hydrogen-induced containment failure therefore centers primarily on intermediate-size Mark-III BWR's and ice condenser PWR's. Containment failure could result from hydrogen combustion equivalent to oxidation of about 25% of the zircaloy cladding.<sup>5</sup> Since approximately 50% of the TMI-2 zircaloy oxidized, the question arises as to containment survivability for intermediate-size containments subject to severe accident conditions.

Oxidation of solid zircaloy is reasonably well understood, where parabolic rate kinetics is governed by the oxygen concentration in the inner layer of metallic zircaloy and the oxygen diffusional resistance of the oxide ( $ZrO_2$ ) surface layer. However, once zircaloy melts, the potential exists for destruction of the protective  $ZrO_2$  layer and direct exposure of molten  $\alpha$ -Zr(O) to steam, which may tend to accelerate the reaction. On the other hand, molten zircaloy relocation and dissolution of  $UO_2$  may reduce the effective surface-to-volume ratio, which could decrease the oxidation rate. In addition, hydriding of unoxidized zircaloy may result in holdup of  $H_2$  in the metallic melt (or solid). These competing effects complicate the understanding of molten zircaloy oxidation.

Degradation of fuel rod geometry can also impact overall hydrogen generation behavior. For BWR canned fuel assemblies, it has been proposed by the Industry Degraded Core Rulemaking (IDCOR) program<sup>a</sup> that clad melting, fuel dissolution, and debris relocation will lead to blocked BWR fuel assemblies.<sup>6,7</sup> Steam pressure buildup below the blockage region is postulated to cause a diversion of the residual coolant to adjacent unblocked assemblies. As a result, boiloff and further oxidation in a degraded BWR assembly are

---

a. The IDCOR program is an independent technical effort sponsored by the commercial nuclear power industry under the corporate auspices of the Atomic Industrial Forum. The purpose of this program is to develop a technical position to assist in deciding whether or not changes in licensing regulations are needed to reflect degraded core or core melt accidents.



Table 1. Inventory of containment types

Category	Volume (m <sup>3</sup> )	Design Pressure (MPa)	Type	Approximate Number of Operating and Future Plants
1	Small (8,000)	0.30-0.42	Mark-I/BWR Mark-II/BWR	25 10
2	Intermediate (40,000)	0.08-0.12	Ice condenser/PWR Mark-III/BWR	10 21
3	Large (80,000)	0.30-0.42	Large Dry/PWR	90

considered terminated at or near the  $\alpha$ -Zr(O)/UO<sub>2</sub> dissolution temperature ( $\sim 2170$  K). The validity of this hypothesis hinges on two key assumptions, a high degree of flow area blockage and an intact BWR channel wall.

To assess unresolved issues, the NRC has initiated an internationally sponsored<sup>a</sup> research program on severe fuel damage (SFD) for light water reactors, where phenomena affecting zircaloy oxidation and the hydrogen source term are of primary concern. The three-part program<sup>8,9</sup> consists of: (1) integral (multi-effect) in-pile fuel behavior and hydrogen generation tests in the Power Burst Facility (PBF) and National Research Universal (NRU) reactor;<sup>b</sup> (2) separate-effects phenomenological laboratory experiments at Pacific Northwest Laboratory on zircaloy oxidation kinetics and at Sandia Laboratory on BWR control rod/channel box oxidation and melt interaction behavior; and (3) computer codes, including the Severe Core Damage Analysis Package (SCDAP) and Melt Progression Model (MELPROG), which integrate governing phenomena into predictive models. Although the PBF-SFD program was initiated in 1981, posttest examination data are now available only for the first two PBF-SFD tests, the Scoping Test (SFD-ST) and SFD 1-1. Since such metallographic data are paramount to the understanding of in-core processes affecting zircaloy oxidation and relocation

behavior, only data from these two PBF-SFD tests are analyzed here. A follow-on report will be issued once the necessary metallography information has been obtained for the remaining PBF-SFD tests (SFD 1-3 and SFD 1-4).

## The PBF-SFD Test Program

The principal test conditions for the PBF-SFD series are summarized in Table 2. For SFD-ST and SFD 1-1, each test bundle consists of 32 fuel rods 0.914 m in length, which are enclosed in an insulated zircaloy shroud and subjected to simulated decay-heat/loss-of-coolant accident conditions. The test sequence consisted of initial boiloff of coolant, resulting in fuel rod overheating, zircaloy-steam reaction, cladding melting and dissolution attack on fuel, release of fission products and hydrogen, and ultimate bundle destruction. Hydrogen and fission product release data were obtained via a monitoring system similar to that shown in Figure 1, although specific fission product detection instrumentation and locations are somewhat different for each test. Four separate measurements were used to assess for zircaloy-oxidation/H<sub>2</sub>-generation behavior; namely, cladding thermocouple data, an on-line measurement of H<sub>2</sub> generation, analysis of the collection tank gas contents for H<sub>2</sub> content, and posttest metallographic assay of zircaloy oxidation.

The data are assessed with respect to the principal outstanding questions of concern, namely: (a) the effect of zircaloy melting and fuel dissolution on oxidation behavior, and (b) fuel reconfiguration effects which may divert steam flow from the degraded region of the core and alter hydrogen

a. Partners in the program include Belgium, Canada, Federal Republic of Germany, Italy, Japan, Netherlands, Republic of Korea, Spain, Sweden, United Kingdom, American Institute of Taiwan, and the United States Nuclear Regulatory Commission.

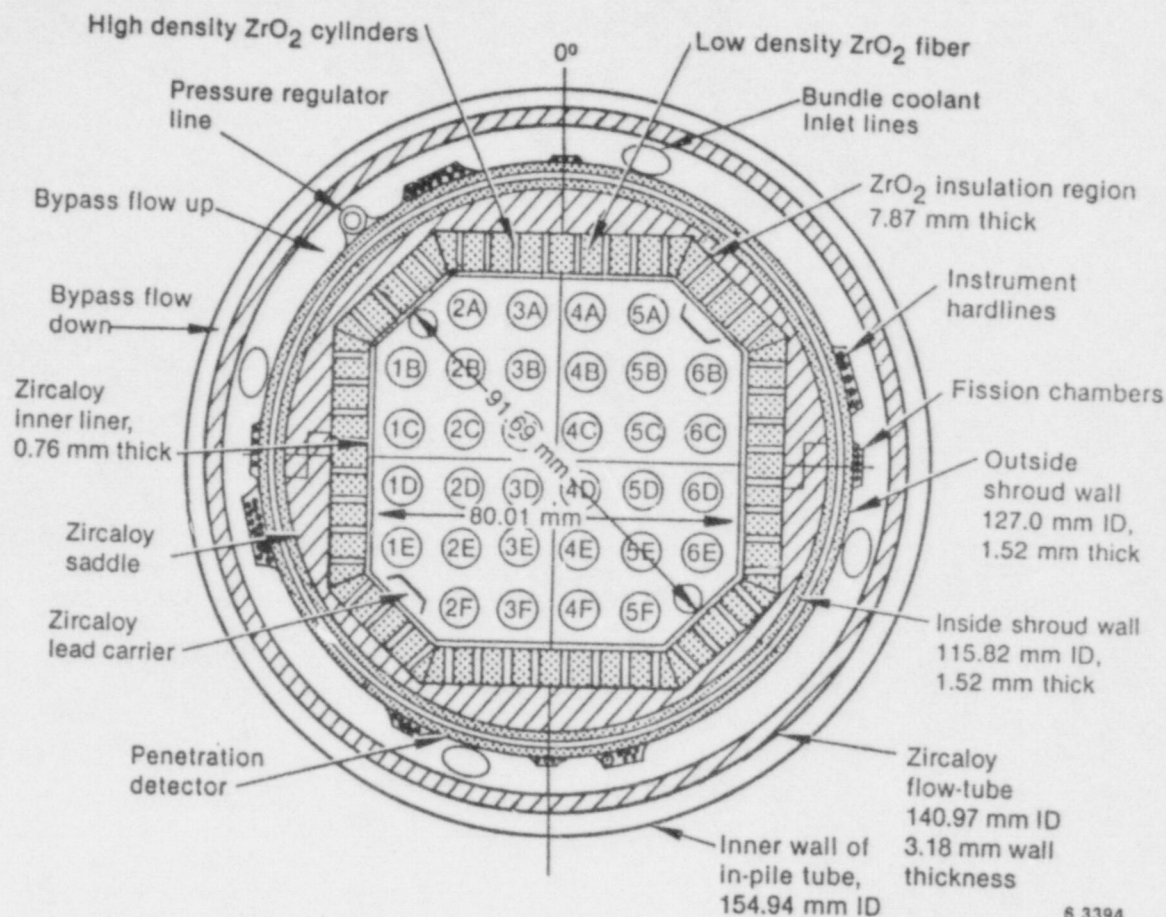
b. Operated by Atomic Energy of Canada Ltd. (AECL) at the Chalk River Nuclear Laboratories (CRNL), Ontario, Canada.

Table 2. The PBF severe fuel damage test series

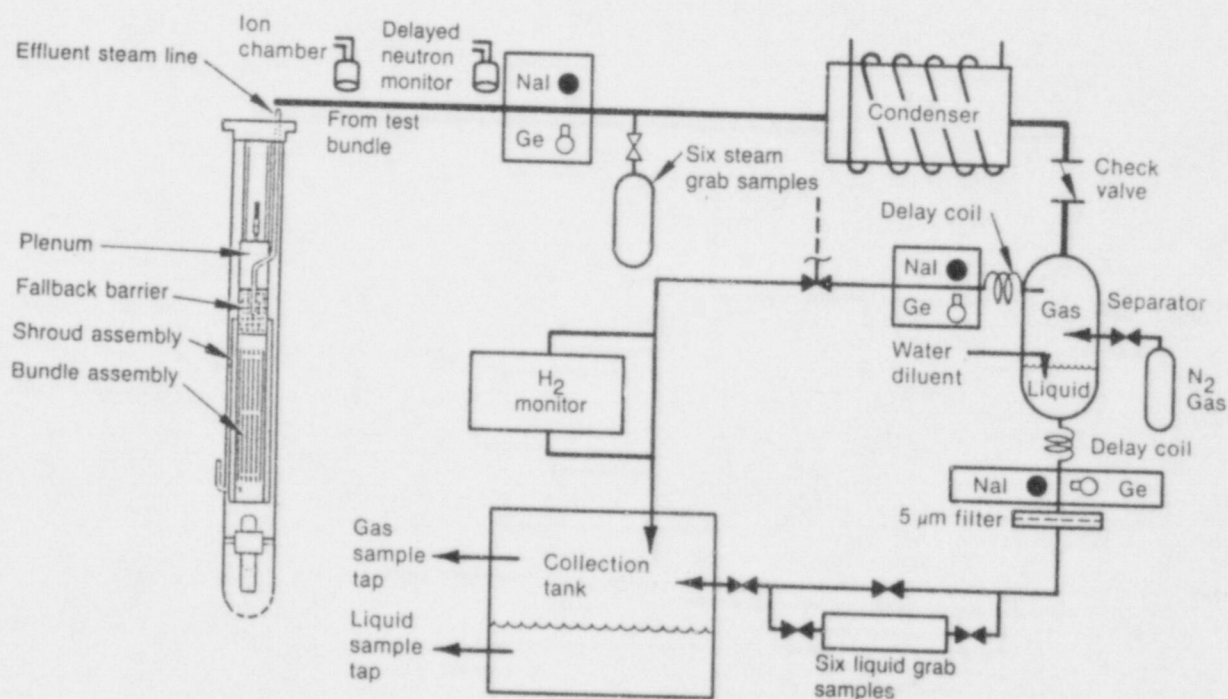
Test	Bundle Description	Nominal Inlet Flow Rate (g/s)	Approximate Steam Production Rate (g/s)	Approximate Heating Rate Prior to Rapid Oxidation <sup>a</sup> (K/s)	Cooldown Procedure
SFD-ST (28 Oct 1982)	32 fresh rods	16	16	0.1 to 0.15	Reactor scram, 16 g/s reflood increasing to ~30 g/s after 4 min. Whole bundle at $T_{\text{sat}}$ after ~8 min.
SFD 1-1 (8 Sept 1983)	32 fresh rods	0.6	0.7 to 1.0	0.46 to 1300 K 1.2 to 1600 K	Power reduction and associated cooldown over 20 min. prior to 17 g/s reflood.
SFD 1-3 (3 Aug 1984)	26 irradiated rods 2 fresh rods 4 guide tubes	0.6	0.6 to 2.4	0.5 to 1200 K 1.9 to 1600 K	Power reduction and argon- associated cooldown over at least 50 min.
SFD 1-4 (7 Feb 1985)	26 irradiated rods 2 fresh rods 4 Ag-In-Cd control rods in guide tubes	0.6	0.6 to 1.26	0.36 to 1200 K 1.4 to 1600 K	Power reduction and argon- associated cooldown over at least 50 min.

a. Above ~1500 K to 2000 K (depending on axial location) in SFD-ST, and about 1600 K in the other three tests, the heating rate was extremely rapid and driven by the metal-water reaction.





6 3394



7-3120

Figure 1. Illustration of the SFD fuel bundle geometry and fission product monitoring system (not to scale).



generation characteristics. To accomplish these objectives, this report is structured as follows. First, the SFD-ST and SFD 1-1 test data relative to zircaloy oxidation and hydrogen generation are presented, including an assessment of the on-line thermocouple and hydrogen generation data, as well as a summary of posttest metallographic observations. Interpretation of the SFD-ST and SFD 1-1 data in terms of hydrogen source term issues, the principal focus of this report, is then

presented, followed by a summary and conclusions. Since a large body of SFD data related to zircaloy-oxidation/hydrogen behavior has been published in prior SFD Test Results Reports,<sup>10,11</sup> much of the peripheral data will not be reiterated here. Rather, this report summarizes the principal relevant findings from each test and their impact on hydrogen source term issues. Supporting data from other documents are extensively referenced throughout this report.

## SFD SCOPING TEST RESULTS

In this section, the SFD-ST data relative to hydrogen production are presented. The test conduct and bundle response with respect to thermal-hydraulic conditions, fuel rod temperatures, and on-line hydrogen measurement (hydrogen monitor and collection tank data) are first given. Findings from posttest metallographic examinations are also summarized concerning the extent and nature of oxidized zircaloy test components. Code predictions are then compared with the data to help reconstruct the test sequence as it applies to oxidation behavior. A detailed interpretation of these data with respect to severe accident hydrogen generation issues is presented in a later section.

Four measurements were used to assess zircaloy oxidation/hydrogen generation behavior; namely, on-line gas analyses, cladding thermocouple data, determination of the collection tank gas contents, and posttest metallographic assay of the extent and nature of test debris oxidation.

On-line gas-sampling data for  $H_2$  content were obtained using a hydrogen monitor that measures the conductivity of the gas passing through the detector cell. Nitrogen carrier gas was used to sweep hydrogen from the liquid-vapor separator to the detector cell. Additionally, during the cooldown phase of the SFD I-I test, argon gas was used to purge residual released fission products and hydrogen from the bundle. Due to the fact that the test effluent must travel through approximately 50 m of piping before it reaches the hydrogen monitor, a delay time existed between the measured hydrogen concentration and the test bundle event that caused it. Real-time in-bundle oxidation and hydrogen release information, therefore, can only be obtained from the hydrogen monitor after a detailed analysis of the transport and mixing of the various gases ( $H_2$ , Ar,  $N_2$ ) in the system. Modeling the bundle and separator as well-mixed volumes and assuming plug flow in the sample line resulted in a reasonably consistent prediction of effluent transport delay, as benchmarked against short- and long-lived noble gas isotopic measurements of transport to various fission product detectors. The uncertainties in the hydrogen monitor data are generally expressed in terms of the uncertainty in the transport delay time from the bundle to the meter.

On-line real-time cladding thermocouple data were used to assess the time at which local heatup was driven by exothermic zircaloy-steam reaction, the progression of the oxidation front through the

bundle, and the time at which zircaloy melting occurred. The cladding thermocouples were sheathed in zircaloy and could measure accurately temperatures up to about 2200 K. Beyond this temperature, the sheath melted, causing virtual junctions to form along the leads and degrade the signal. The liner was also mounted with thermocouples to assess bundle periphery temperatures.

The third measurement involved assay of the collection tank gas contents by mass spectrometer analysis and provided a measurement of the total hydrogen released during each test. The accuracy of the collection tank data can be quantified from additional mass spectrometer measurements of the known helium fill-gas inventory in the test rods and the  $N_2$  gas supplied to the separator. The SFD-ST collection tank gas sample, extracted into a measurement cylinder for mass spectrometer analysis, leaked prior to measurement. Thus, no collection tank data are available for the SFD-ST experiment, although such data were obtained for the three subsequent SFD tests.

Final assay of the extent of zircaloy oxidation and associated hydrogen generation was determined from metallographic examination of zircaloy-bearing test debris. By measuring the thickness of the  $ZrO_2$  and  $\alpha$ -Zr(O) layers in representative debris samples, an estimate was made of the total amount of bundle oxidation. Inspection of the zircaloy debris also yielded information on oxidation behavior of both solid and previously molten debris.

### Test Conduct

Test SFD-ST, the first test of the PBF-SFD series, was conducted on October 29, 1982. Reference 10 presents detailed information on the overall test conduct and results. The test train consisted of thirty-two zircaloy-clad  $UO_2$  fuel rods, 0.914-m long, arranged in a 6 x 6 array without corner rods. The test bundle was contained in an insulating shroud consisting of low-density  $ZrO_2$  insulation material sandwiched between inner and outer zircaloy metal walls. Figure 1 shows a cross-sectional view of the test bundle and monitoring system, while Figure 2 presents an axial view of the in-pile test train components. The nominal design characteristics of the fuel rods used in SFD-ST are presented in Table 3. The test train was highly instrumented with fuel rod centerline, cladding,

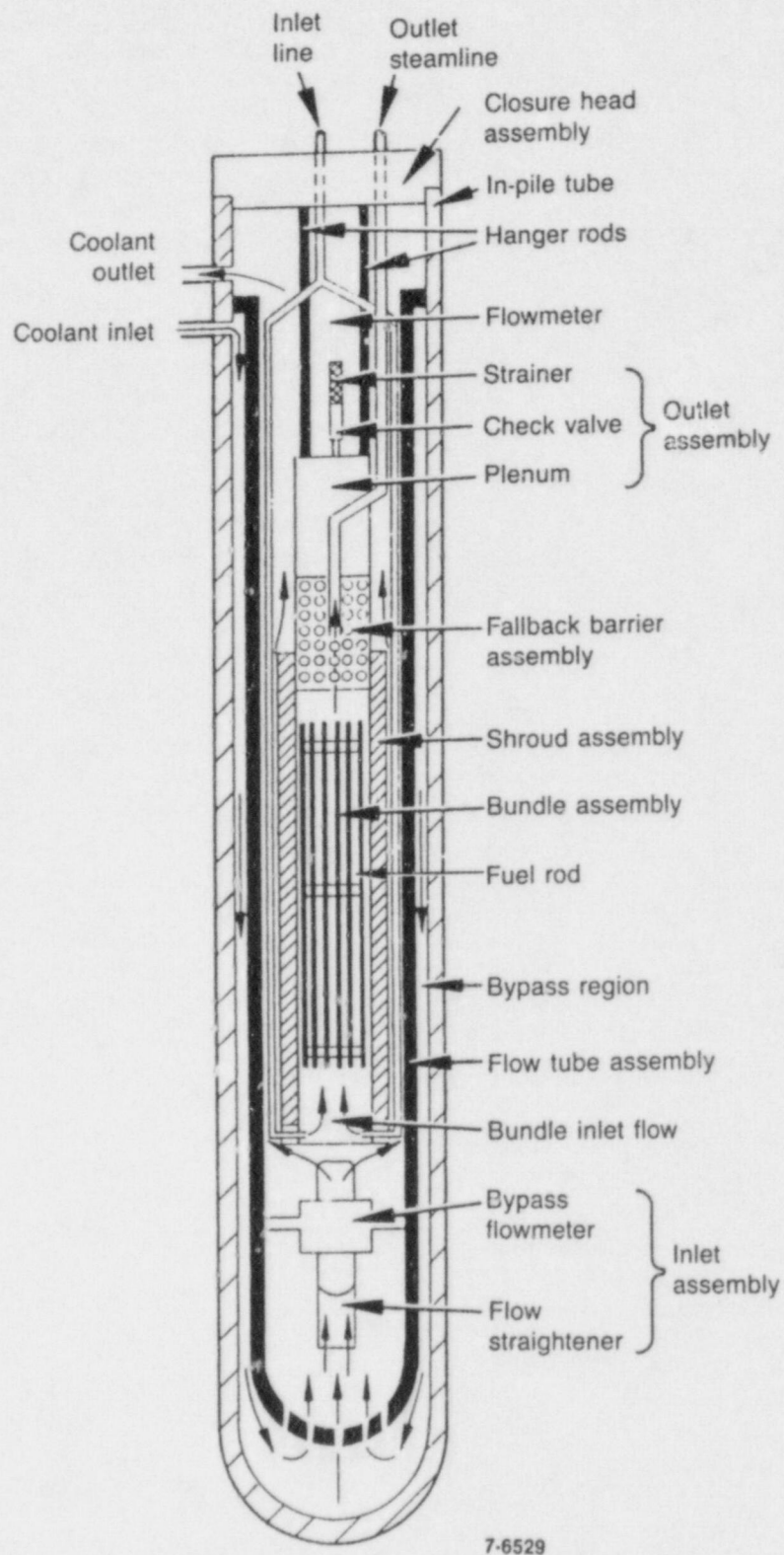


Figure 2. Axial view of the SFD-ST test train components.



and steam thermocouples, as well as flowmeters, pressure sensors, and fission chambers. The entire high-temperature effluent consisting of superheated steam, fission products, hydrogen, and other noncondensable gases was routed through an insulated line to the fission product and hydrogen monitoring and collection system.

**Table 3. Nominal design characteristics for SFD-ST**

**Fuel:**

Material:  $\text{UO}_2$  sintered pellets  
Pellet OD: 8.27 mm  
Pellet length: 9.53 mm  
Pellet enrichment (wt%  $^{235}\text{U}$  in total U): 6.2 wt%  
Density: 10.2 g/cm<sup>3</sup>  
Fuel stack length: 0.914 m  
End dish: 1% of pellet volume  
Total fuel mass (32 rods): 16.2 kg

**Cladding:**

Material: ASTM B353, grade RA-2 (zircaloy-4 tubing)  
Tube OD: 9.63 mm  
Tube wall thickness: 0.60 mm  
Tube ID: 8.43 mm  
Total zircaloy mass (32 rods): 4.4 kg

**Fuel Rod:**

Spring material: Inconel X-750  
Spring load on fuel stack: 22.2 to 66.7 N  
Filler gas: helium  
Fill gas volume: 9.68 cm<sup>3</sup>  
Initial gas pressure: 3.8 MPa  
Diametral gap: 0.16 mm  
Plenum volume: 2.79 cm<sup>3</sup>  
Pitch: 12.75 mm  
Insulator pellet material:  $\text{Al}_2\text{O}_3$   
Total fuel rod mass (32 rods): 20.6 kg

After initial fuel preconditioning and power calibration, the SFD-ST fuel bundle was subjected to a high-temperature transient leading to coolant boiloff and attendant exposure of the test fuel rods to steam. Boil-down was achieved by a reduction in water inlet flow to approximately 16 g/s and bundle nuclear power ramping from ~24 to 93 kW. The calculations presented in Appendix A (see Table A-1) indicate that at the nominal makeup flow of 16 g/s, a steam-rich environment over the entire bundle length can be expected during the initial heatup phase of the test ( $T < 1500$  K). Figure 3 shows the bundle nuclear power and pressure, while Figure 4 presents the coolant flow rate and liquid level as a function of test time.

Thermocouple measurements of temperatures on the inside surface of the cladding indicated that rapid cladding oxidation occurred in the bundle near the end of the test and propagated downward into the lower region of the bundle, where the heat of reaction drove fuel temperatures above 2400 K. This is illustrated in Figure 5, where rapid oxidation of the zircaloy is shown to begin at the 0.7-m elevation at 197 min into the transient, at the 0.5-m elevation at about 200 min, and at the 0.35-m elevation at about 203 min.

In addition to thermocouple data, on-line pressure and flow meter instrumentation also indicated test events which can be used to infer an overall test scenario and bundle oxidation behavior. Although the high makeup flow (16 g/s) in general ensured a steam-rich environment during most of the test, pressure and coolant flow variations did occur. Since at elevated cladding temperatures ( $> 1900$  K) zircaloy oxidation behavior is largely controlled by steam supply conditions, flow perturbations can have a significant effect on hydrogen generation characteristics. The most significant events affecting overall system thermal-hydraulics for the SFD-ST experiment occurred at the time of shroud failure (184 to 185 min) and relocation of molten material (204 to 206 min). The effects of these flow perturbations are discussed in Appendix B and can be summarized as follows. A temporary reduction in bundle pressure at the time of shroud failure resulted in a temporary increase in the coolant vaporization rate. However, since cladding temperatures were below 1800 K at this time, shroud failure and its attendant effects on bundle thermal-hydraulic behavior had little impact on overall hydrogen generation characteristics. At about 204 min into the test, fuel rod material relocation is indicated to have occurred, accompanied by pressure and flow anomalies. Reactor scram occurred shortly thereafter (206 min). The rapid sequence of events that occurred during these last few minutes of the test make it difficult to distinguish a cause-effect relationship between molten test debris relocation, thermal-hydraulic perturbations, and overall oxidation behavior. However, the flow anomalies at this time did not appear to significantly alter the oxidation-driven heating transient at the end of the test and the attendant high rate of hydrogen release.

## On-Line Hydrogen Data

As discussed in References 10 and 11, there is a significant delay time between the measured hydrogen concentration in the hydrogen monitor and the test bundle event that caused it. This is due to the

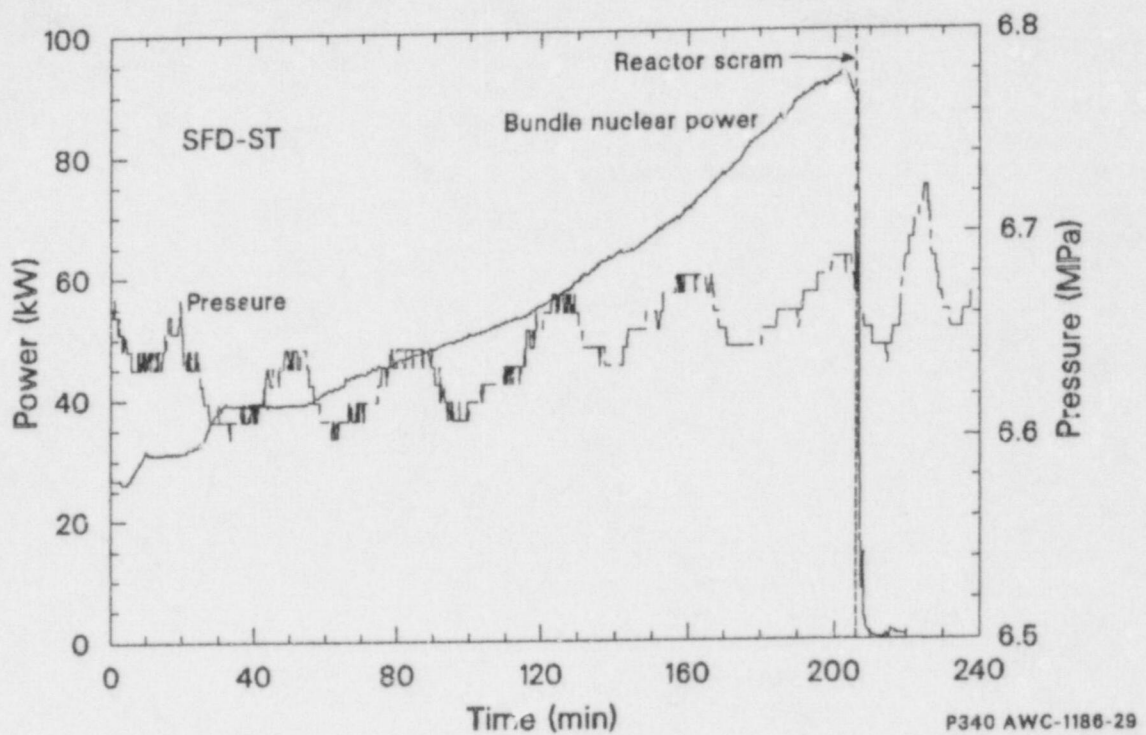


Figure 3. Bundle nuclear power and system pressure for Test SFD-ST.

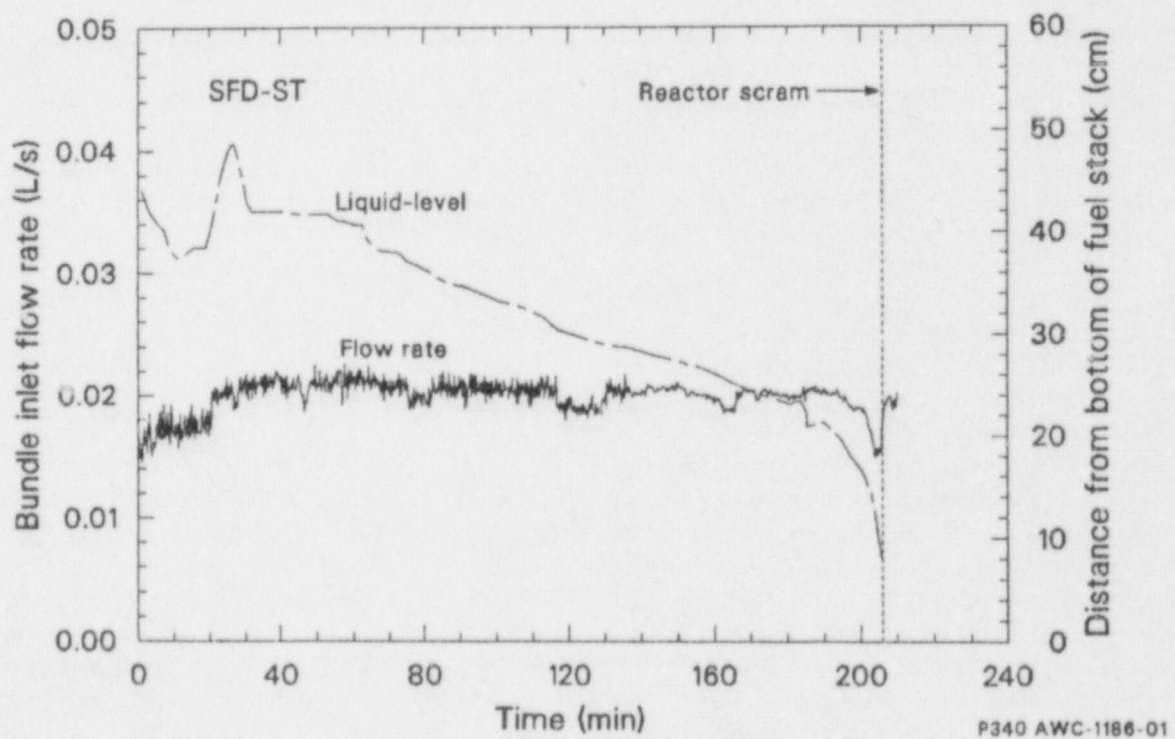


Figure 4. Coolant liquid level and flow rate for Test SFD-ST.

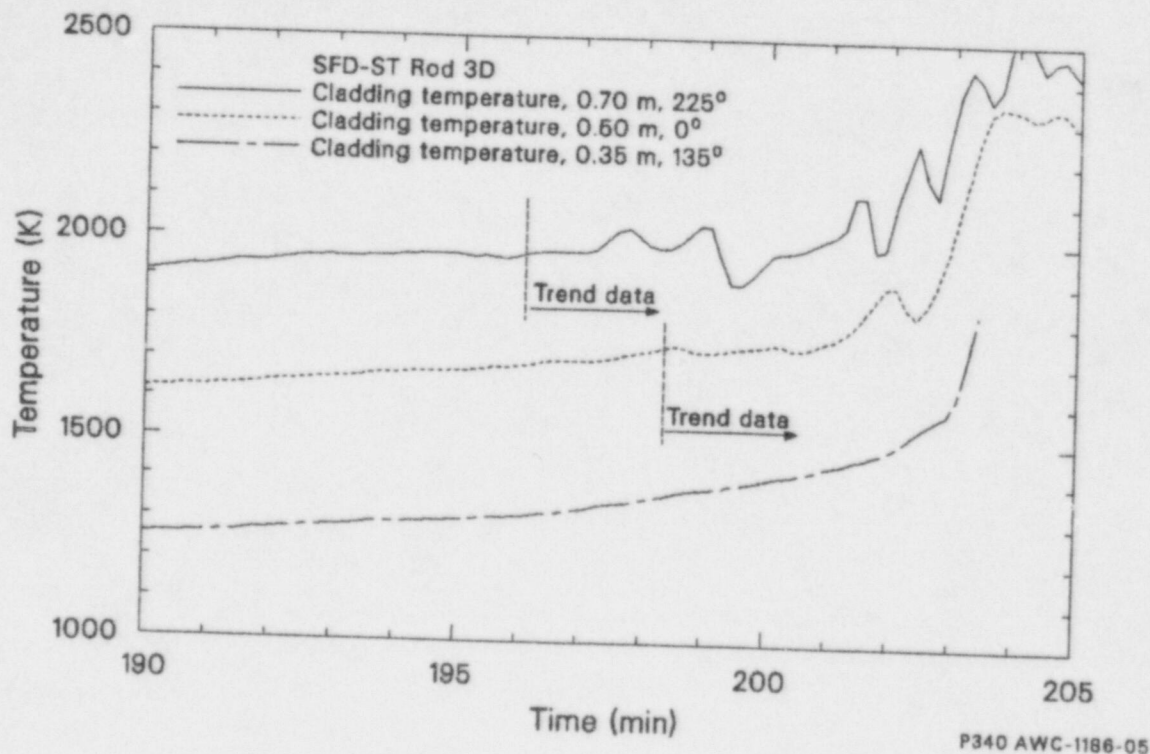


Figure 5. Comparison of SFD-ST fuel Rod D3 cladding temperatures at three axial locations.

fact that the test effluent must travel through approximately 50 m of piping before it reaches the hydrogen monitor. In addition,  $N_2$  gas is used to sweep hydrogen from the liquid/vapor separator to the measurement cell. Thus, measurement system conditions alter the hydrogen concentration, as detected by the hydrogen monitor, from conditions that existed in the test bundle. A fluid transport and mixing model was therefore developed to infer real-time hydrogen generation characteristics in the bundle from the measured response of the hydrogen monitor. The details of the transport and mixing model are discussed in Reference 10.

The SFD-ST on-line measurement of  $H_2$  release, corrected for transport delay to the hydrogen monitor, is shown as a function of time in Figure 6. A large spike in hydrogen release is noted near the time of reactor scram. The measured hydrogen concentration did not fall immediately to zero following reactor scram because it took several minutes to cool and reflood the bundle. Thus, hydrogen continued to exit the bundle, probably due to a combination of post-scram zircaloy and  $UO_2$  oxidation and flushing of stagnant spaces within the bundle, as well as from possible release from once-hydrated zircaloy. Integration of the mass release rate provided the cumulative hydrogen release curve shown, with a total nominal value of 375 g and an

uncertainty range of  $\pm 140$  g. The large uncertainty in the integral value is due to a diminished hydrogen monitor sensitivity at high  $H_2$  concentrations late in the test (see Appendix D of Reference 10). In addition, an uncertainty of  $\pm 3$  min is estimated in the effluent transit time<sup>10</sup> from the bundle to the detection system during the peak hydrogen generation period, based on a comparison of the ratio of isotopic activities measured at various spectrometer locations for short- and long-lived noble gas isotopes. Unfortunately, there was a leak in the sampling bomb containing gas extracted from the effluent collection tank, so that no data are available on the hydrogen collected in the effluent collection tank. Collection tank data would normally be used to benchmark the integrated on-line measurement.

As discussed in Reference 10, the total on-line measurement of  $375 \pm 140$  g hydrogen is greater than that produced by complete oxidation of the zircaloy cladding (155 g) and shroud inner liner (73 g). A total hydrogen generation value of  $\sim 220$  g ( $+40$  g,  $-88$  g) was estimated from the posttest metallographic assay of the test debris, which indicated extensive oxidation not only of the cladding and liner but also of other zircaloy test components (saddle fallback barrier, end caps), as well as fuel oxidation. This metallographic value is significantly below the nominal 375 g



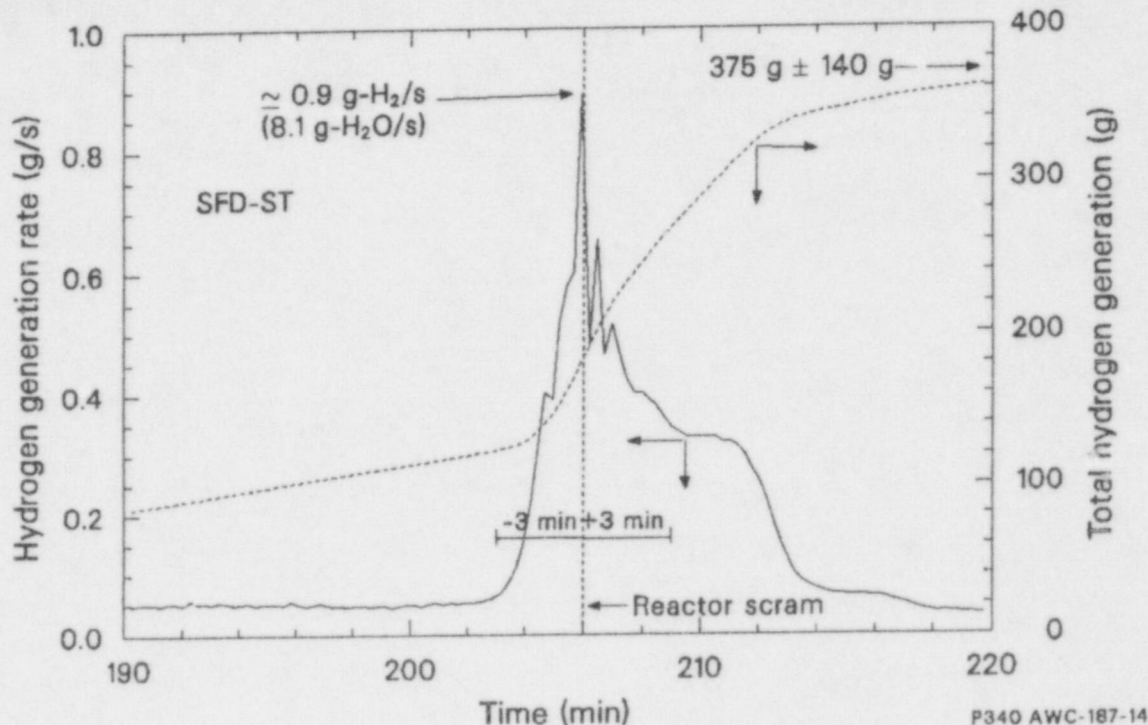


Figure 6. SFD-ST on-line in-bundle hydrogen generation behavior, adjusted for transport delay to the hydrogen monitor.

estimated from integration of the hydrogen monitor data. The error in the hydrogen monitor measurement can be attributed to a diminished sensitivity at high  $H_2/N_2$  molar ratio, where nitrogen carrier gas at a constant flow rate of 0.74 g/s was used to sweep gaseous effluent from the separator into the measurement cell. The low nitrogen flow rate diminished the meter sensitivity to hydrogen during the period of peak oxidation, i.e., beyond a test time of 200 min. Because of the uncertainties in the hydrogen monitor data late in the test, the metallographic results are considered more reliable after 200 min. Before 200 min, the hydrogen monitor data provide a reasonable time-dependent indication of hydrogen generation. Integration of the mass release curve during the first 200 min yields a hydrogen release value of  $113 \pm 10$  g.<sup>10</sup>

In addition to the on-line measurement of hydrogen release, a perspective of the overall time-dependence of zircaloy oxidation for the SFD-ST transient can be obtained from inspection of the cladding thermocouple data.

## Thermocouple Data

The cladding thermocouples provided reliable data only up to about 200 min into the test. After 200 min, most of the zircaloy-sheathed thermocouples shunted and formed virtual or new junctions as a result of relocation of molten material around the thermocouple leads. A radially averaged temperature history for the 0.35-m, 0.50-m and 0.70-m elevations has been computed from the qualified thermocouple data of the instrumented fuel rods distributed throughout the bundle.<sup>10</sup> These average temperature profiles are presented in Figure 7 and are terminated when the signals became erratic, indicating shunting. Inspection of the measured cladding temperatures indicates that during the first 190 min into the test transient fuel rod heatup was governed by nuclear heating at a rate of about 0.1 to 0.2 K/s; at times greater than 190 min, heatup is driven by oxidation. Prior to thermocouple failure, heatup rates in excess of 3 K/s were measured. Figure 7 also compares the average cladding and fuel

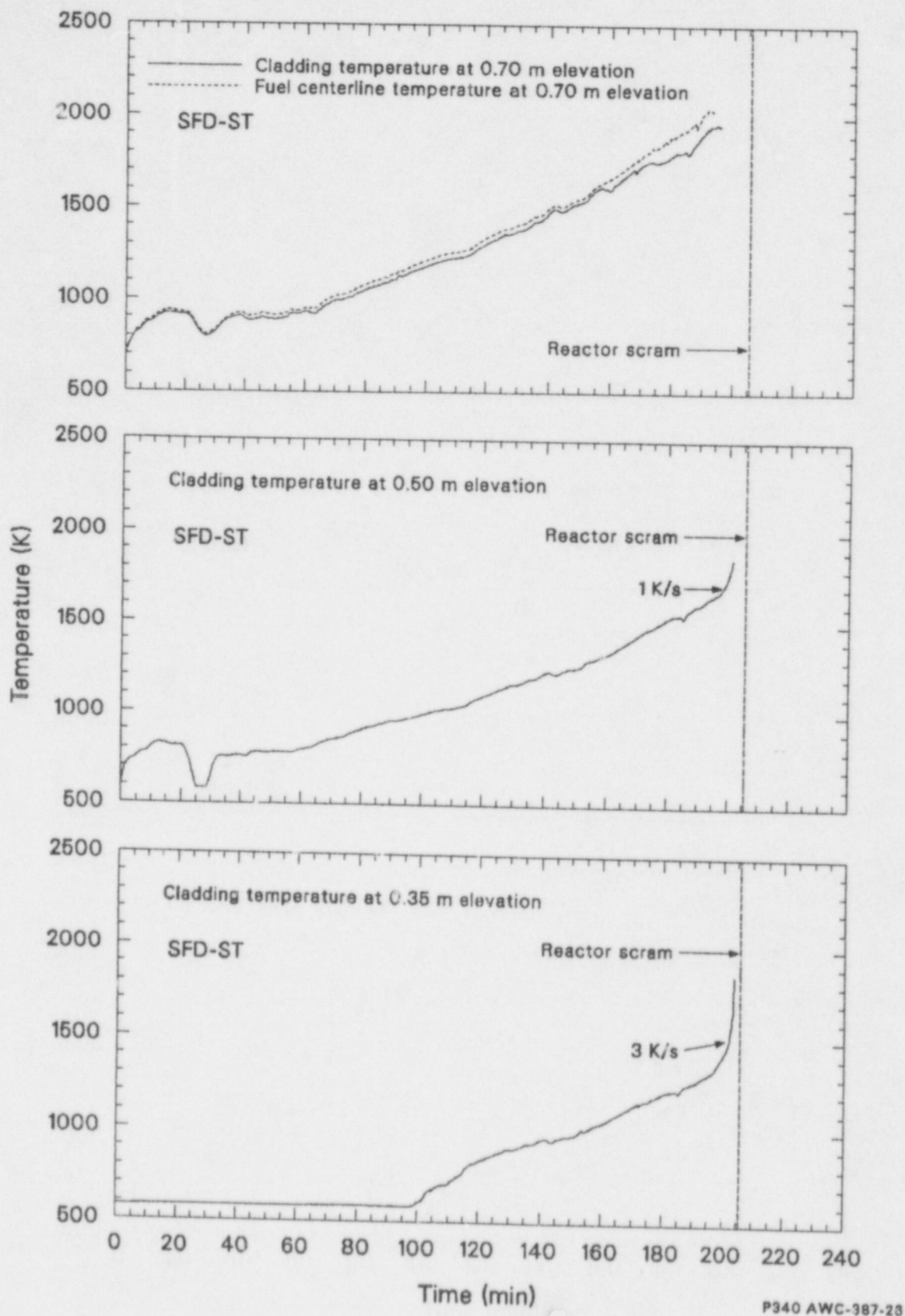


Figure 7. Radially averaged thermocouple measurements of SFD-ST cladding and fuel centerline temperatures.

centerline temperatures at the 0.7-m elevation. The six instrumented rods containing fuel centerline thermocouples agreed within  $\pm 50$  K with the cladding temperature through most of the transient.

## Summary of Posttest Bundle Examination Data

Posttest examination of bundle geometric characteristics and assay of zircaloy oxidation were also conducted and are summarized here. The detailed data are presented in Reference 10.

**Bundle Geometric Characteristics.** Extensive flow area blockage with a reduced zircaloy surface-to-volume ratio may tend to diminish the overall hydrogen production, so that this effect is of importance in the assessment of the PBF-SFD test data.

Although posttest pressure drop measurements over the bundle length and computerized tomographic reconstruction of the degraded bundle give qualitative information on the extent of flow area degradation, the most reliable blockage data were obtained from posttest metallographic examination. Nine cross-sectional samples of the bundle were examined, located at the 0.055-, 0.145-, 0.17-, 0.245-, 0.270-, 0.395-, 0.495-, 0.825-, and 0.915-m elevations above the bottom of the fuel stack. The 0.17-m sample, shown in Figure 8, was found to exhibit maximum blockage.

As discussed in Reference 10, definition of an effective bundle flow area from visual examination of end-of-test metallographic cross-section samples is complicated by the participation of the shroud liner and insulation material in bundle reconfiguration. Therefore, degradation of flow area was quoted in terms of changes in the area within the saddles. In the as-built geometry, the  $\text{UO}_2$  fuel occupied 19.9% of the intersaddle area, the cladding 6.3%, and the liner and insulation 31.2%, leaving a flow area of 42.6% (of which 0.8% is associated with the rod gap space). Measurement of the degree of flow area degradation within the confines of the original inner liner was not possible due to oxidation and melt failure of the zircaloy inner liner and fuel rod debris interaction with the  $\text{ZrO}_2$  insulation material. The percentage of flow area degradation within the liner was therefore taken as equivalent to the percentage of blockage within the confines of the saddle. Although this may not be totally satisfactory, the alternative would involve unquantifiable judgment as to that amount of a cross-section sample occupied by fuel rod debris versus liner and insulation debris, as well as judgment concerning interaction between these

two classes of bundle material. Based on this methodology, the residual flow area from metallographic examination of the sample at the 0.17-m elevation was found to be about 31.7% (see Ref. 10, Table 4), which converts to a nominal posttest open flow area of approximately 10.2  $\text{cm}^2$ . (The original bundle flow area within the liner was  $\sim 32.2$   $\text{cm}^2$ .)

As will be shown later in this report, flow area blockages greater than 98% would be required to inhibit the 16-g/s steam flow through the SFD-ST degraded bundle, which translates to a residual open flow area of less than 0.65  $\text{cm}^2$ . Although uncertainties exist with respect to the exact specification of a degraded flow area based on posttest metallographic examination, the metallographic data do not indicate such an extreme blockage condition. The uncertainty of the nominal degraded flow (10.2  $\text{cm}^2$ ) area can be as much as 9.55  $\text{cm}^2$  without alteration of the conclusions regarding blockage-induced flow diversion effects (see Analysis section of this report).

It should also be noted that the blockage data from cross-sectional examination yields information only with respect to the final reconfigured state of the bundle. During actual testing, a different transient blockage configuration most certainly occurred as test debris relocated from higher to lower bundle elevations. However, the extent of flow area blockage during testing cannot be ascertained, to any degree of accuracy, from the limited on-line data available. For example, the on-line pressure perturbations can be attributed not only to an increase in flow resistance but also to enhanced boiloff due to debris/coolant thermal interaction, so that the individual contributions to increased pressurization cannot be deduced with any degree of certainty. The blockage data nevertheless should give a reasonable estimate of the maximum extent of blockage, since it presents a picture of cumulative debris relocation for the entire experiment. For these reasons, the posttest cross-sectional measurement of material blockage is considered the best available estimate of flow area degradation.

**Bundle Oxidation Characteristics.** There were several components in the test train that had the potential to oxidize and release hydrogen, namely the fuel rod cladding, the zircaloy saddle, the zircaloy inner liner, the end caps, the fallback barrier, and the fuel. Table 4 presents the maximum possible  $\text{H}_2$  generation based on the available zirconium.<sup>10</sup> The final column in Table 4 lists the extent of oxidation of the various components estimated from metallographic examination of the test debris. The metallographic results were obtained from



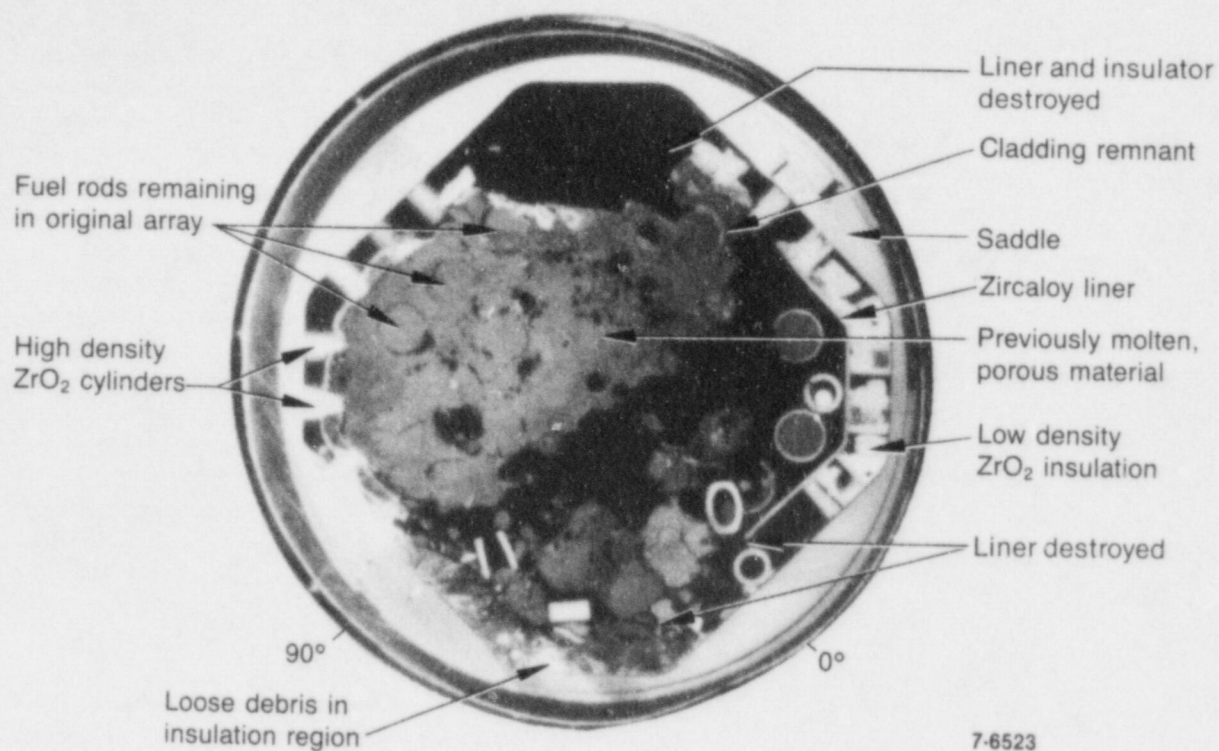


Figure 8. Metallographic cross section of the SFD-ST bundle at the 0.170-m elevation.

Table 4. Potential SFD-ST sources of hydrogen generation and metallographic results

Source	Hydrogen Generation (g)	
	Upper Limit	Metallographic Estimate
Cladding	155	112
Upper end caps	12	12
Lower end caps <sup>a</sup>	21	0
Shroud inner liner <sup>b</sup>	73	39
Lead carriers	6	4
Shroud saddle <sup>b</sup>	593	0
Fall-back barrier <sup>c</sup>	22	5
Total zirconium	882	172 ± 40 g
Fuel <sup>d</sup>	—	48 ± 0 48
Total zirconium plus fuel	—	220 ± 40 88

a. Based on the standard fuel rod end caps.

b. Based on the region between the bottom of the fuel stack and the steamline inlet elevations.

c. Portion of fallback barrier up to the elevation of the steamline.

d. Estimated based on two-thirds of the bundle oxidized to  $\text{UO}_{2.6}$  and considered as a maximum value.

ZrO<sub>2</sub> and  $\alpha$ -Zr(O) thickness measurements of zircaloy debris, where local sample measurements were used to ascribe representative values over a defined axial region of the bundle. Specific details of these measurements are given in Reference 10.

A total hydrogen generation value of 220 g (+40 g, -88 g) was assessed from this metallographic study, consisting of  $172 \pm 40$  g from oxidation of zirconium components and an upper limit of  $\sim 48$  g from fuel oxidation. Figure 9 presents a composite plot of the on-line measurement of hydrogen release up to 200 min and the end-of-test metallographic results. Such a comparison indicates that approximately  $113 \pm 10$  g of hydrogen were generated prior to 200 min, with the remainder being generated at some unquantified time after 200 min. This figure summarizes the most reliable SFD-ST hydrogen generation data that can be used for interpretation of test results.

A U-Zr-O metallic material can oxidize while in both the solid and liquid state, releasing hydrogen in the process.<sup>12,13</sup> If oxidation occurs for a solid U-Zr-O metallic material,  $\alpha$ -Zr(O) will transform to ZrO<sub>2</sub> and the (U,Zr) alloy will transform to (U,Zr)O<sub>2</sub>, where the two phases are distinguishable in posttest micrographs. However, oxidation of metallic U-Zr-O melt by steam will produce a ZrO<sub>2</sub> + (U,Zr)O<sub>2</sub> solid solution which appears homogeneous. Both types of oxidation products were found in the posttest metallographic inspection of the SFD-ST debris.

Figure 10 illustrates the oxidation behavior of previously molten metallic debris which froze in the spacing between two ballooned cladding remnants at the 0.495-m elevation. The previously molten metallic melt is shown to have partially dissolved the oxidized cladding (ZrO<sub>2</sub>). However, the previously molten, formerly metallic debris has been transformed to a ceramic phase, indicating that it was oxidized by steam, since complete metallic-to-ceramic phase transformation can occur only by steam-induced oxidation of the melt. This type of oxidation of previously molten debris is mainly evident in the lower regions of the bundle and is associated with relocated metallic melt.

Evidence of oxidation of previously molten metallic debris after it had solidified is shown in Figure 11. One can recognize the initially oxidized cladding with its typical columnar grain structure. The cladding was in contact with melts both on the outside and inside. The melt between the oxidized cladding and the fuel partially caused pellet disintegration. This metallic melt then solidified, forming

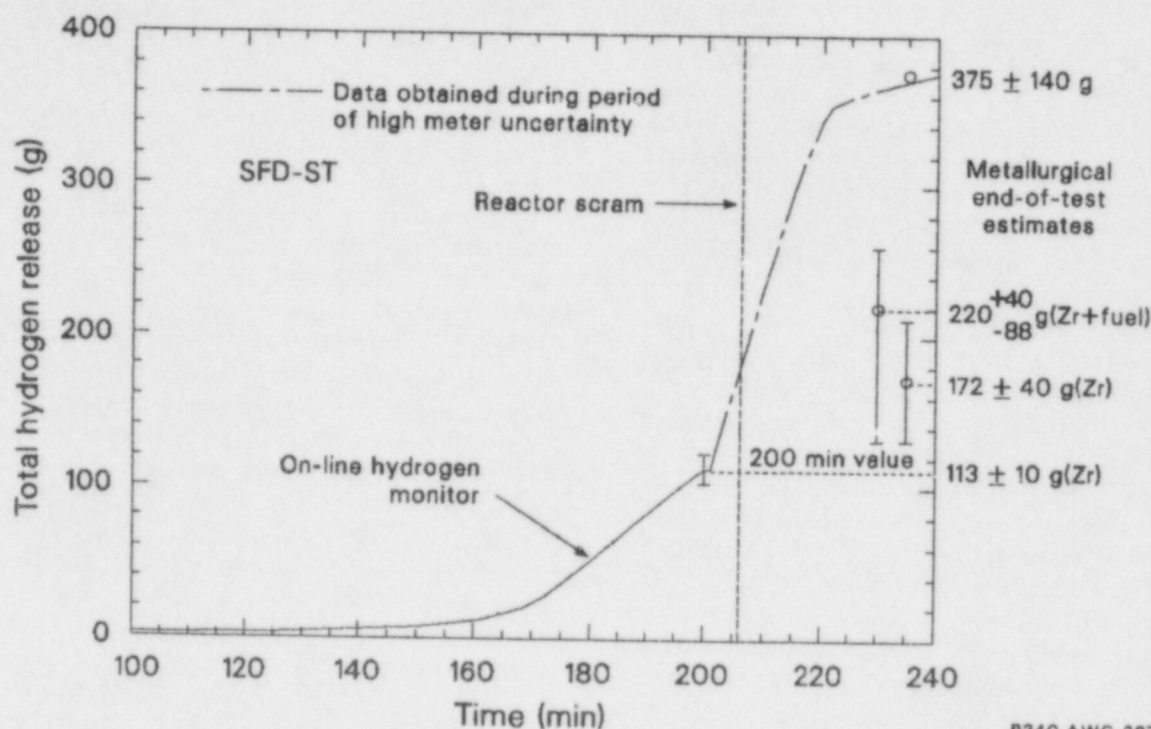
pores of various sizes, and apparently was oxidized later (in a solid state) by steam, as evidenced by two distinguishable heterogeneous phases of ZrO<sub>2</sub> and (U,Zr)O<sub>2</sub> near the pore surface.

In addition to oxidation of previously molten Zr-O-U material, examination of the SFD-ST fuel indicates UO<sub>2</sub> oxidation to a hyperstoichiometric condition, which adds to the overall hydrogen generated via the reaction  $\text{UO}_2 + x\text{H}_2\text{O} = \text{UO}_{2+x} + x\text{H}_2$ . Scanning Auger Spectroscopy (SAS) of three SFD-ST debris samples indicates an increase from as-fabricated stoichiometric UO<sub>2.0</sub> fuel to hyperstoichiometry in the range of UO<sub>2.4</sub> to UO<sub>2.6</sub>. Figure 12 is a photomicrograph of the SFD-ST fuel remains, indicating a change in fuel stoichiometry from initially UO<sub>2.0</sub> to UO<sub>2+x</sub>, which decomposes on cooling to form UO<sub>2.0</sub> plus U<sub>4</sub>O<sub>9</sub> precipitates.<sup>14</sup> Steam ingress into the failed rods is considered the cause of fuel oxidation. An upper estimate of hydrogen generation by fuel oxidation was presented in Reference 10, assuming that two-thirds of the fuel oxidized to UO<sub>2.6</sub>, with a net contribution of about 48 g hydrogen (see footnote d, Table 4). It is interesting to note that precipitates of U<sub>4</sub>O<sub>9</sub> were also found in the TMI-2 debris.<sup>15</sup>

## Code-Predicted Oxidation Behavior

Analysis of the SFD-Scoping Test was also performed with the Severe Core Damage Analysis Package (SCDAP);<sup>16</sup> details of the calculations performed for the SFD-ST experiment are presented in Reference 10. In this section, a summary description is given of such predictions relative to predicted zircaloy oxidation and hydrogen generation behavior. (No MAAP predictions for SFD-ST are available.)

To predict the transient nature of oxidation and attendant hydrogen generation, one must accurately model the test sequence leading to coolant boiloff and fuel rod overheating, as well as overall bundle thermal hydraulics (pressure and geometry conditions, heat sinks, heat sources, flow rates, etc.). Uncertainties in inlet flow and bundle power characteristics are dominant contributors to uncertainties in code predictions. The SCDAP-predicted oxidation and hydrogen generation histories are therefore sensitive to the calculated boil-down/fuel heatup transient, so that accurate modeling of oxidation behavior and attendant hydrogen release requires accurate modeling of the actual test boil-down and fuel rod heatup transient. Small differences between the predicted (SCDAP) and actual (test)



P340 AWC-287-12

Figure 9. Comparison of the SFD-ST integrated on-line measurement of hydrogen release and estimates from posttest metallographic examination.

boildown/heatup transient can lead to large differences in predicted versus actual oxidation behavior.

To assess modeling deficiencies versus errors arising from input data uncertainties, several SCDAP SFD-ST calculations have been performed. The SFD-ST test results report<sup>10</sup> presents two key SCDAP calculations; a "reference" calculation, using the posttest derived input data, and a "sensitivity" calculation, where the input boundary conditions were adjusted within the specified uncertainties to achieve agreement with the major reliably measured parameters (i.e., cladding temperatures, liquid level, bundle power). Here the sensitivity calculation is briefly summarized to illustrate predicted oxidation behavior for the SFD-ST test. The adjusted input boundary conditions for this sensitivity calculation were the inlet coolant enthalpy and the axial power profile.

A comparison of the measured and SCDAP-predicted coolant level is presented in Figure 13, while cladding temperatures at three axial elevations are shown in Figure 14. The measured and calculated coolant elevation, and fuel rod temperatures show good agreement from the steady-state period up to about 190 min into the transient. The ensuing underprediction of the coolant elevation, with a corresponding overprediction in fuel rod

temperature, is indicative of the additional effective bundle power resulting from accelerated oxidation late in the test (> 200 min).

A total zircaloy oxidation-induced hydrogen production value of 81 g was predicted by the SCDAP simulation of the SFD-ST experiment, versus  $172 \pm 40$  g based on metallographic data. Fuel oxidation is ignored in the present comparison because it is not modeled in the SCDAP code. As discussed in Reference 10, the final 6 min of the test were not well simulated by SCDAP, so that it may be of more value to extract a comparison for the initial 200 min. Integration of the hydrogen monitor mass release curve for this period provides a value of  $113 \pm 10$  g. The equivalent prediction from the SCDAP calculation is 74 g, with 71 g generated from oxidation of the cladding and 3 g from the shroud inner liner. Thus, prior to onset of high temperatures (> 2000 K) and attendant loss of rod geometry, the SCDAP calculation underpredicted the hydrogen measurement by about 35%.

Although adjustment of input boundary conditions eventually yielded a reasonable hydrogen generation history for the first 200 min of the test, the SCDAP-predicted oxidation behavior after initiation of zircaloy melting and loss of rod geometry





7-6526

Figure 10. Illustration of oxidation behavior of previously molten metallic SFD-ST debris which froze in the spacing between two ballooned cladding remnants at the 0.495-m elevation.

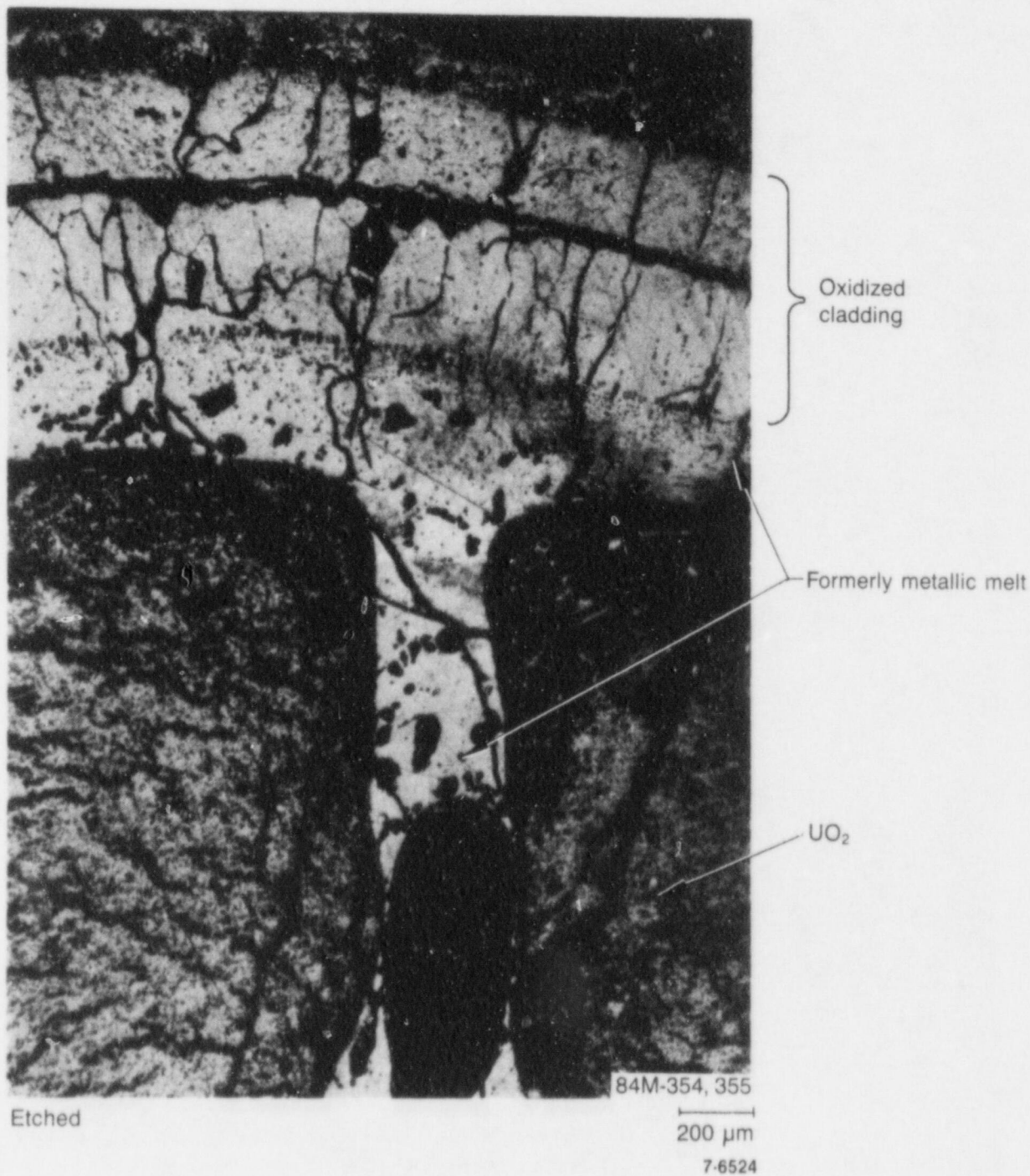
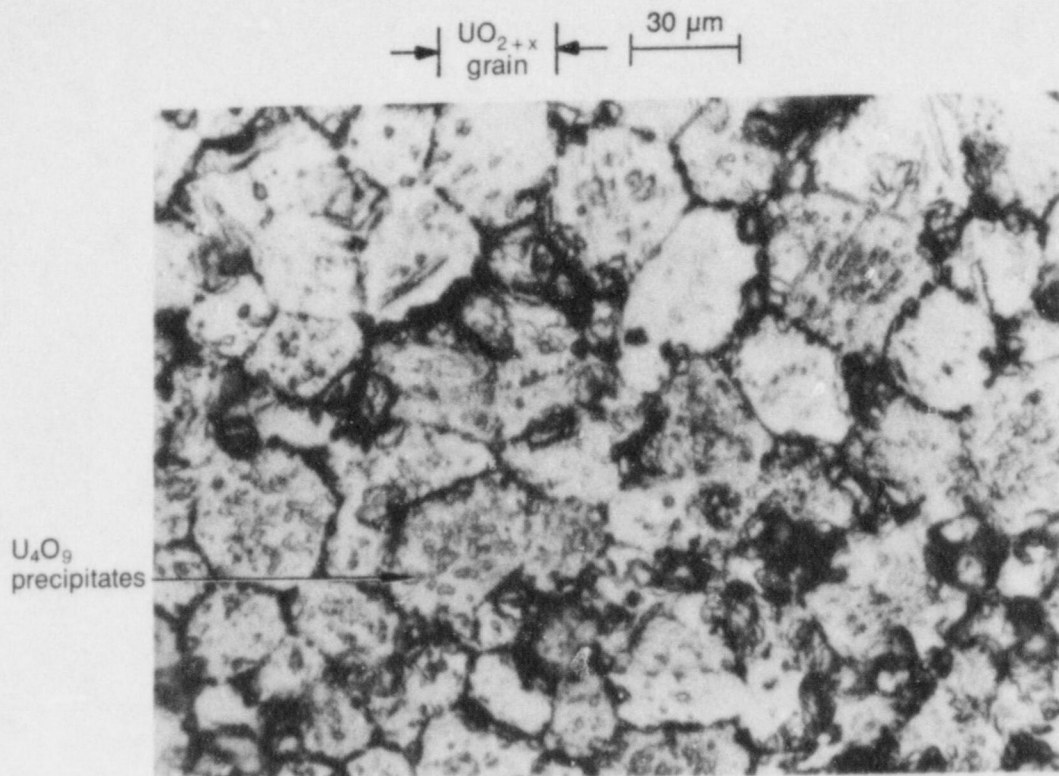


Figure 11. Evidence of SFD-ST metallic melt penetration into a UO<sub>2</sub> fuel pellet crack at the 0.495-m elevation, where the melt subsequently froze and oxidized.



7-6527

Figure 12. Posttest SFD-ST fuel debris, indicating  $\text{UO}_2$  oxidation to  $\text{U}_4\text{O}_9$  precipitates.

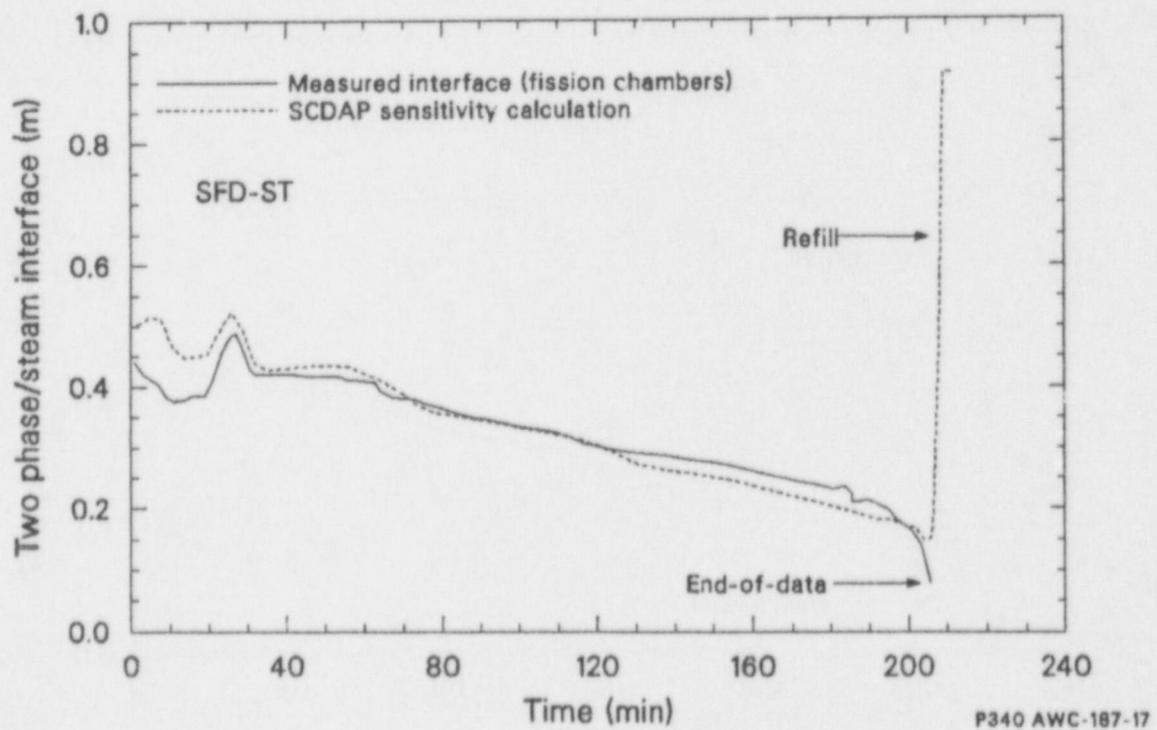


Figure 13. Comparison of the SFD-ST measured and SCDAP-calculated two-phase/steam interface elevation.



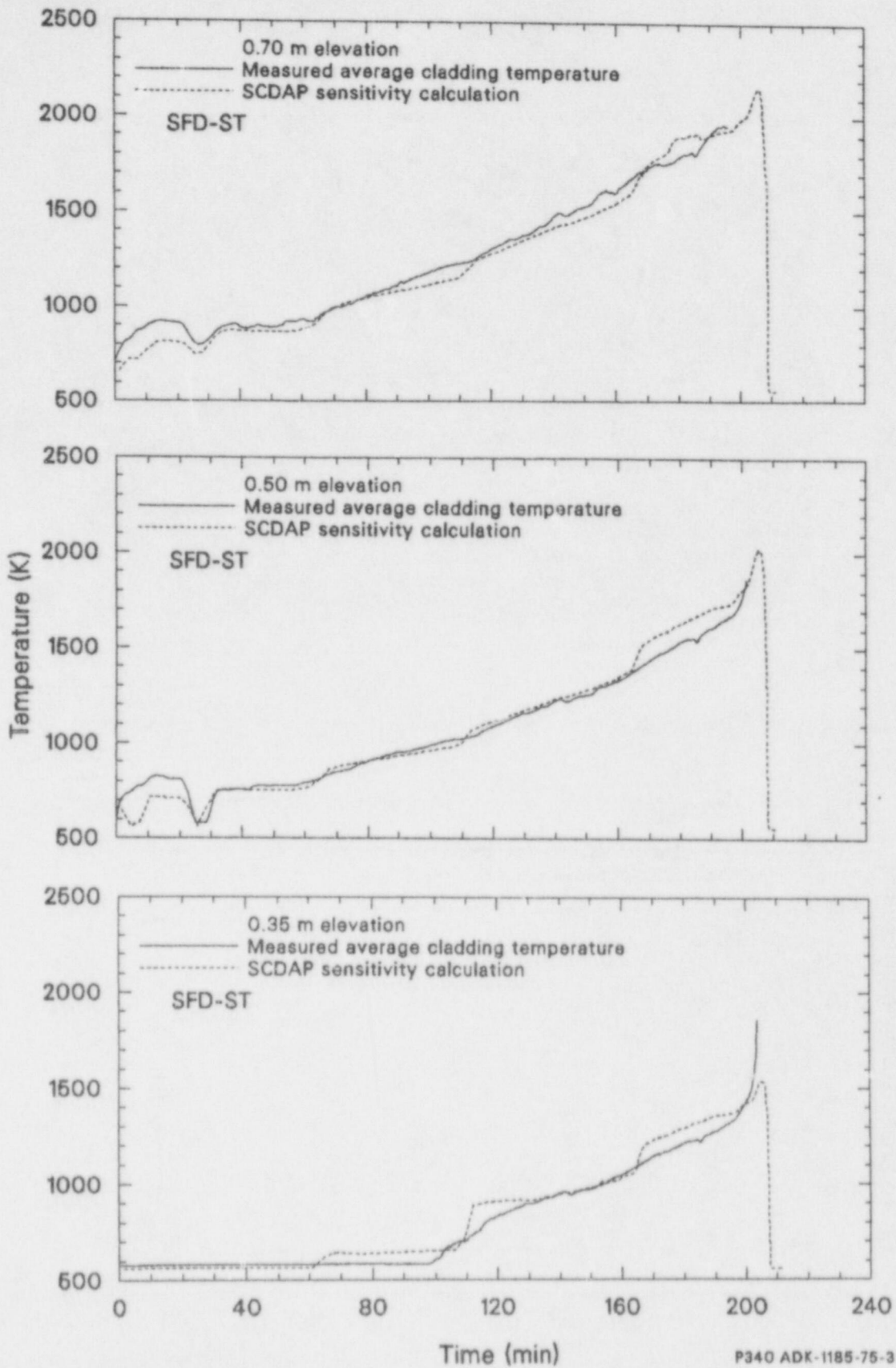


Figure 14. Comparison of the SFD-ST measured and SCDAP-calculated cladding temperatures at three axial elevations.

was greatly underpredicted. About 25-40% of the total hydrogen generation during the SFD-ST experiment can be attributed to oxidation after the initiation of zircaloy melting and relocation, a

regime which is not easily characterized by code models. The SCDAP calculation thus illustrates the difficulties in predicting oxidation behavior once rod geometry has been lost.

## SFD 1-1 TEST RESULTS

This section presents the overall SFD 1-1 test conduct, bundle response with respect to system conditions, fuel rod temperatures, measurements of hydrogen production, and a summary of post-test metallographic findings. SCDAP and MAAP code analysis of bundle thermal-hydraulics and oxidation behavior are also given.

### Test Conduct

Test SFD 1-1, the second test of the PBF-SFD series, was completed on September 8, 1983. This test was similar to SFD-ST; however, because the SFD 1-1 test was designed to simulate conditions of a small-break loss of coolant accident (LOCA), it was run at a much lower rate of makeup coolant flow ( $\sim 0.64$  g/s). As a result, bundle oxidation was generally steam-starved during most of the transient. (Steam starvation calculations are given in Table A-2 of Appendix A.) In addition, the SFD 1-1 test was terminated by a slow cooldown rather than by rapid bundle reflood. Details of the test conduct and overall test behavior are presented in Reference 11.

The SFD 1-1 test bundle geometry was similar to the SFD-ST bundle except for the addition of a bypass tube and temperature profile detector, which were added to the corner regions of the bundle. The temperature detector was intended to measure axial movement of a temperature front along the bundle height; however, it failed during the test so that no data were obtained from this device. A bypass flow tube was introduced into the SFD 1-1 test train for the purpose of ensuring coolant flow past the bundle should total blockage occur upon relocation of molten test debris. The bottom of the bypass tube was at the -0.105-m elevation and was fabricated from  $\text{ZrO}_2$ , with an ID of 4.75 mm and a cross-sectional flow area of  $0.177 \text{ cm}^2$ . Posttest examination of the SFD 1-1 bundle, however, revealed that the bypass tube was also destroyed during the test.

After initial fuel preconditioning and power calibration, the bundle was subjected to a high-temperature transient leading to coolant boiloff and exposure of the test fuel rods to steam, with attendant high-temperature cladding oxidation. Boildown was achieved by a reduction in water inlet flow to approximately  $0.64 \text{ g/s}$  and power ramping from  $\sim 8$  to  $35 \text{ kW}$ . The test was terminated by a gradual decrease in power; fuel cooldown was

accomplished by the addition of argon gas, which also purged fission products and hydrogen from the bundle.

An overview of the thermal-hydraulic behavior of the SFD 1-1 test bundle is presented in Figure 15, where bundle nuclear power, pressure, coolant mass makeup flow rate, and in-bundle liquid level are shown. The two-phase liquid coolant level shown in Figure 15 is based on fission chamber data. The general temperature response of the SFD 1-1 bundle is illustrated in Figure 16, which shows the cladding temperature of Rod 3F at the 0.35-m elevation (up to 2034 s) and the bundle fission power during the transient. The high-temperature transient was initiated at 720 s when the cladding temperature was about 800 K. The bundle nuclear power was slowly increased to maintain a bundle average heatup rate (as measured by 18 cladding thermocouples) of  $0.46 \text{ K/s}$  up to  $\sim 1300 \text{ K}$ . At 1300 K, the bundle average temperature ramp rate had increased to  $1.2 \text{ K/s}$  due to the exothermic oxidation of the zircaloy cladding by steam. When the average bundle temperature had reached 1700 K at about 1950 s, the temperature ramp rate had increased to above  $6.8 \text{ K/s}$ . At about 2000 K ( $\sim 2034 \text{ s}$  for Rod 3F), the thermocouples failed, forming new junctions at unknown lower locations so that further temperature-elevation data are unreliable. The power was held constant at  $\sim 36.4 \text{ kW}$  for 220 s before a power decrease was begun at 2394 s.

Of particular interest to zircaloy oxidation and hydrogen generation is the bundle boildown sequence and zircaloy temperature history. Both the bundle inlet makeup flow and the steam/two-phase interface level were measured indirectly. Makeup coolant flow to the bundle was provided by a positive displacement injection pump, which was calibrated to deliver  $0.6 \text{ g/s}$ . In addition, bypass coolant was supplied to the outer shroud region of the test assembly to ensure that the in-pile test tube (IPT) was maintained at low temperatures ( $\sim 535 \text{ K}$ ). The bypass flow was held constant at  $2.63 \text{ L/s}$  ( $1950 \text{ g/s}$ ). Leakage flow ( $-0.15$  to  $+0.45 \text{ g/s}$ ) from the IPT bypass coolant to the bundle was detected prior to the transient during isothermal subcooled conditions and when the bundle was partially filled with steam. It was not possible to determine the source of the leakage. However, a mass balance<sup>11</sup> of coolant flow through the test apparatus indicated that the nominal flow through the bundle was  $\sim 0.64 \text{ g/s}$  throughout the transient, composed of the pump inlet flow ( $0.6 \text{ g/s}$ ) and an additional  $0.04 \text{ g/s}$  presumed to be leakage. The estimated uncertainty in



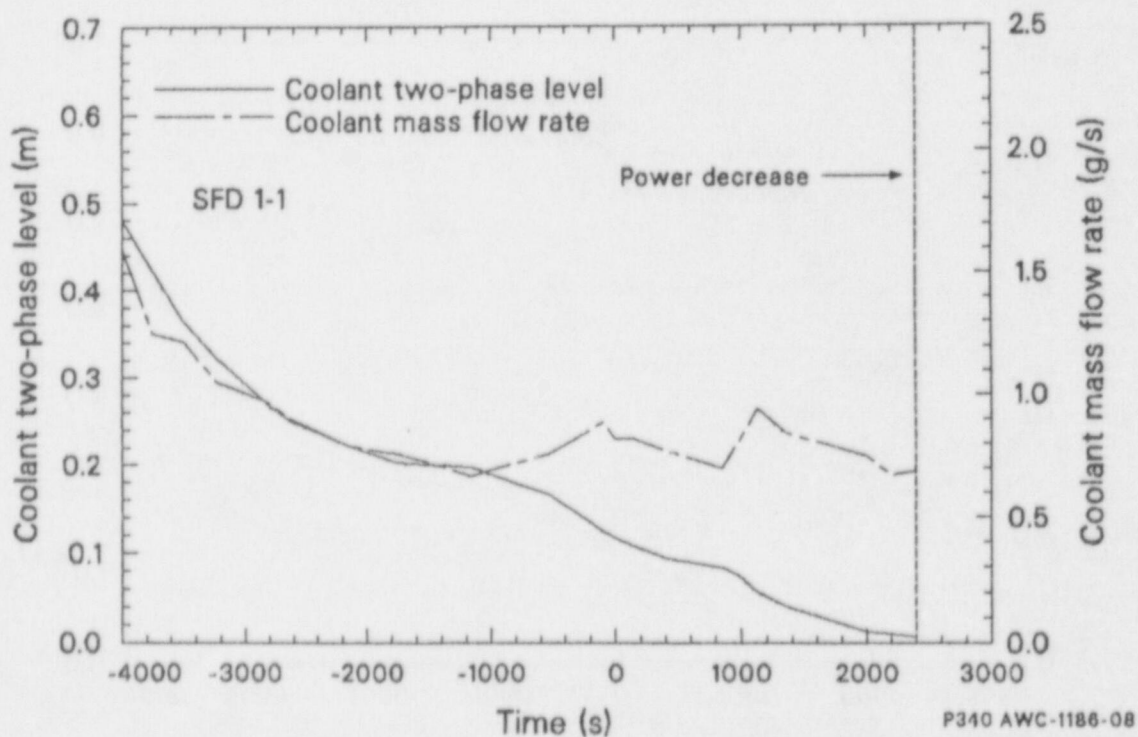
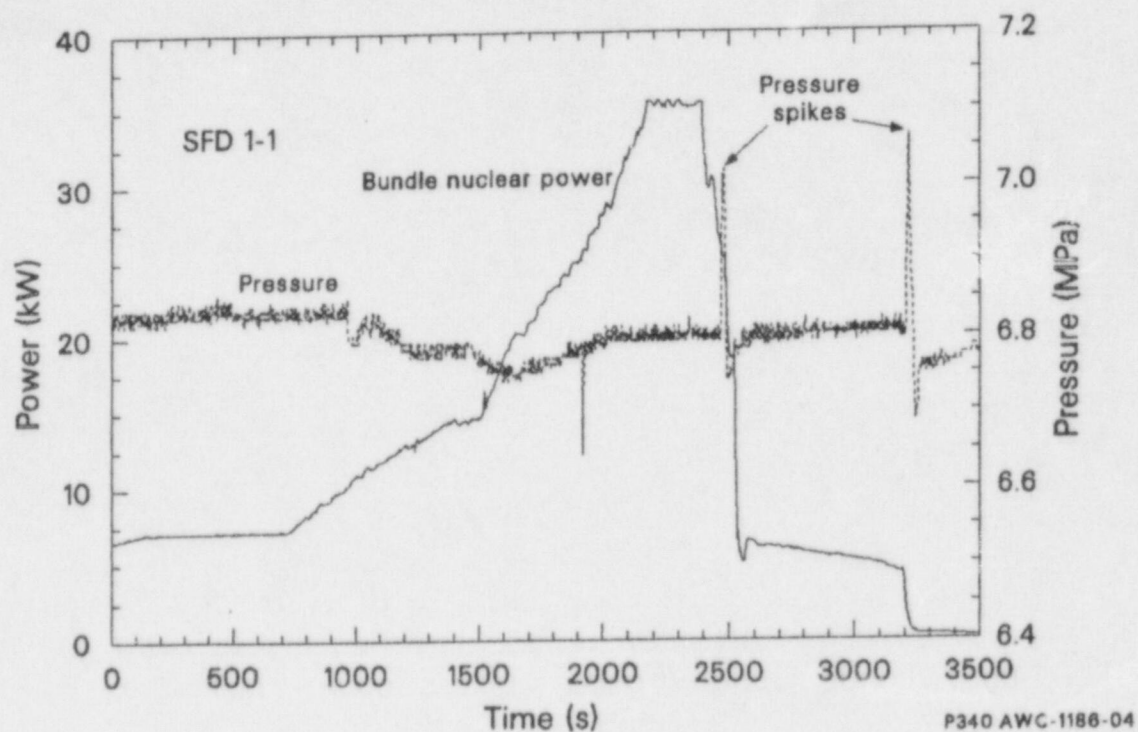


Figure 15. Test SFD 1-1 thermal-hydraulic conditions.

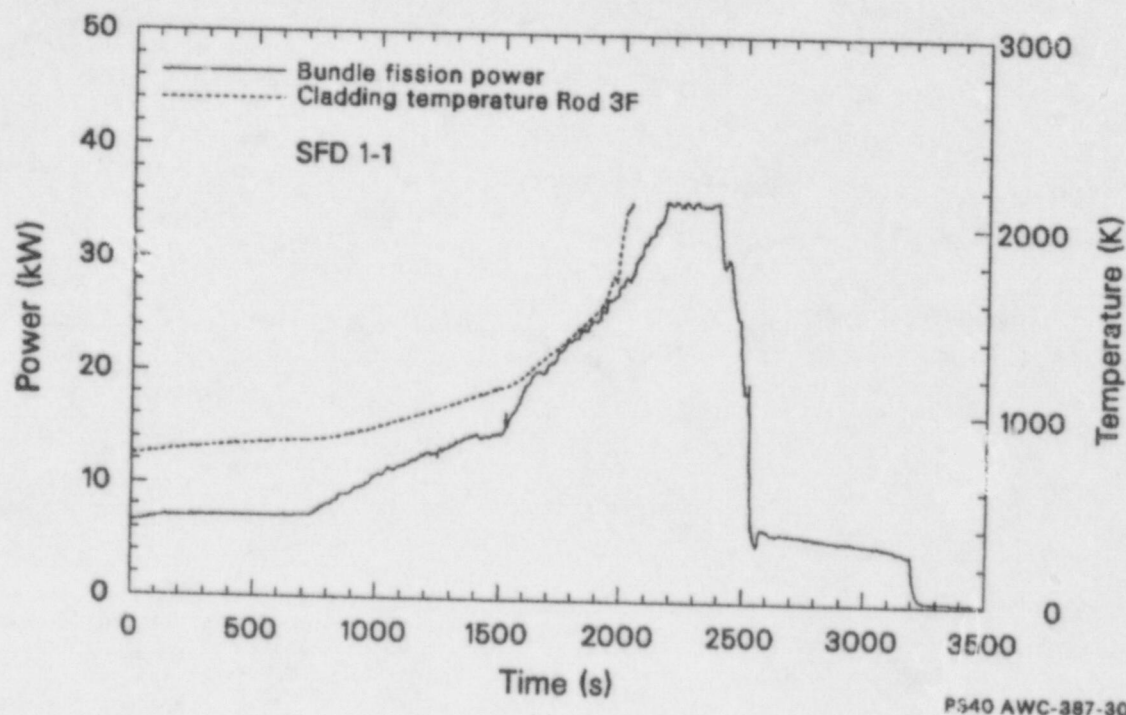


Figure 16. Test SFD 1-1 bundle fission power and cladding temperature histories at the 0.35-m elevation.

the bundle flow is  $\pm 0.06$  g/s, based on the accuracy of the separator flow meter and the calibration of the bundle injection pump.

It should be noted that the uncertainties associated with the boiloff rate and net coolant flow rate during the later stages of the test add to uncertainties in the assessment of a time-dependent oxidation/hydrogen production scenario. In addition to the nominal flow ( $\sim 0.64$  g/s), additional steaming due to debris-coolant interaction or inflow of bypass coolant upon shroud failure could have contributed to enhanced steam boiloff during the test period. At that time, the boil-down level was below the lowest elevation fission chamber ( $-0.02$  m) and bundle geometry changes were occurring. Uncertainties in net steam production rate at this critical time add to the uncertainties in distinguishing specific details of oxidation behavior. Such effects are discussed in the following subsections, relative to their impact on hydrogen generation.

### On-Line Hydrogen Data

As mentioned previously, there is a significant delay time between the measured hydrogen concentration in the hydrogen monitor and the test bundle event that caused it, due to both the  $\sim 50$  m of piping and the separator between the bundle and the

monitor. The addition of nitrogen at the separator and the use of argon gas to sweep hydrogen from the bundle and liquid/vapor separator to the measurement cell also affect delay times and effluent gas concentrations. Thus, hydrogen concentration conditions as measured by the hydrogen monitor are different from those in the bundle. A fluid transport and mixing model was developed to correct for these effects and to infer real-time hydrogen generation characteristics in the bundle from the measured response of the hydrogen monitor. Models used to account for these effects are presented in Reference 11.

The best-estimate hydrogen generation rate corrected by the effluent transit model is plotted in Figure 17. Also plotted is the integrated release value as a function of time. The transit-corrected hydrogen data first show a gradual increase in response between 1400 and 1800 s, which is due to the release of helium from ruptured fuel rods. (The hydrogen monitor is unable to distinguish between hydrogen and helium gas.) The drop at 1800 s indicates that the gap release had terminated at that time. Figure 17 also indicates that hydrogen production continued to increase through the high-temperature portion of the transient to a peak value of 0.09 g/s at 2500 s. It is interesting to note that a hydrogen production rate of 0.09 g/s is

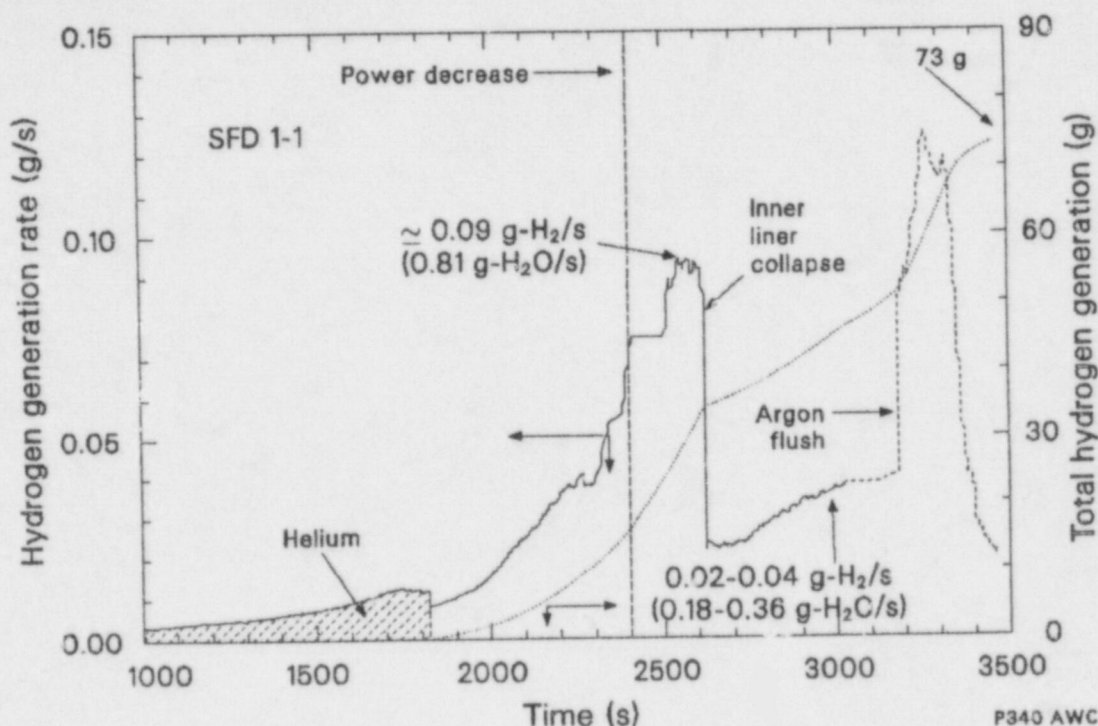


Figure 17. Test SFD 1-1 on-line in-bundle hydrogen generation behavior, adjusted for transport delay to the hydrogen monitor.

equivalent to a steam consumption rate of 0.81 g/s, which is above the nominal inlet coolant flow rate of 0.64 g/s. The difference is considered to be due to enhanced boiloff of water that entered the bundle through the shroud as a consequence of saddle collapse.<sup>11</sup> It is also noted that the hydrogen generation rate dropped sharply at 2600 s.

The drop in hydrogen production at 2600 s is considered due to collapse of the shroud inner liner resulting in a reduced zircaloy surface-to-volume ratio and partial steam bypass around the hot material. A hydrogen generation rate of 0.02 to 0.04 g/s is equivalent to about a 30 to 50% consumption of the nominal makeup flow (0.64 g-H<sub>2</sub>O/s = 0.071 g-H<sub>2</sub>/s). Nevertheless, the SFD 1-1 data indicate only partial reduction in hydrogen generation after loss of rod geometry. Beyond 2600 s, the hydrogen generation rate remained low, between 0.02 and 0.04 g/s, indicating only partial consumption of the nominal bundle makeup flow (i.e. 0.18 to 0.36 g steam consumed per second).

At 3200 s, argon was introduced into the bundle and the apparent hydrogen release rate increased sharply. Although total steam consumption would again be implied by the second burst of hydrogen at 3300 s, this result is questionable in light of the conditions in the bundle at this time. Bundle tem-

peratures were less than 1500 K at 3200 s and oxidation rates should have been low (see following section). The sudden increase in hydrogen release is suspect and may be partially the result of flushing of previously generated hydrogen from the upper plenum to the monitor or possibly due to moisture carryover from the separator upon argon flush. (The hydrogen monitor would be expected to be sensitive to moisture, since the conductivity of water is greater than hydrogen gas.) Likewise, the indicated H<sub>2</sub> pulse could also have been due to release of previously generated hydrogen absorbed in zircaloy metal (hydriding), where a reduction in the H<sub>2</sub> partial pressure upon argon flush may have initiated such release. Any one of these, or a combination of several such factors, could have contributed to the final pulse of hydrogen indicated by the hydrogen monitor data.

Figure 18 shows that two coolant flow paths were used at different times during the experiment. During preconditioning, coolant flowed through the fallback barrier and a check valve into the bypass coolant. For the high-temperature transient, the check valve was closed so that effluent was routed to the sampling and monitoring system via the steam pickup line. As a result, the space above the fallback barrier may have



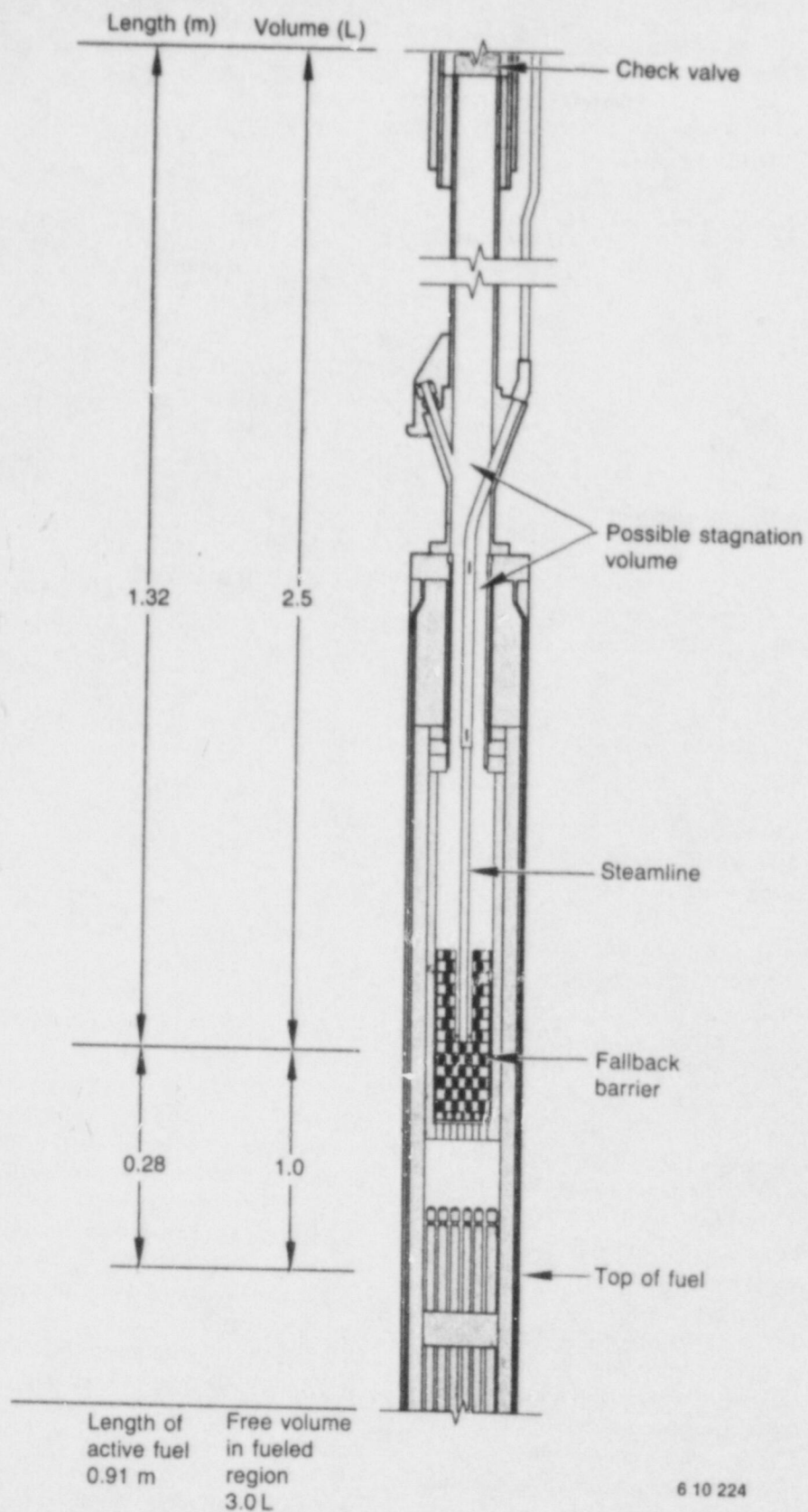


Figure 18. Schematic of SFD 1-1 upper test train showing the stagnant volume which may have retained hydrogen.

become stagnant. Since steam in this space would continuously condense, allowing new gases to enter, this dead space may have contained significant hydrogen. The process of filling this volume with hydrogen is thought to have occurred early in the experiment prior to ~2300 s. However, when the argon flush was introduced into the bundle at 3200 s, mixing and eventual displacement of hydrogen would be expected.

An estimate of the mass of hydrogen associated with filling the 2.5-L dead space above the fallback barrier is presented in Table 5. Although no direct temperature measurements in the region above the bundle were made, it is expected that the temperature would be in the range of that of the coolant bypass, approximately 540 K. This translates to about 7.8 g of hydrogen fill gas, which would be released exponentially with time. Integration of the area of the second peak indicates about 23 g of hydrogen release from 3200 to 3400 s. Because this is about three times that due to purging of hydrogen from above the fallback barrier, continued oxidation of the zircaloy components in the bundle is considered likely even after argon was introduced into the system or until the steam had been completely purged from the bundle. Integration of the hydrogen monitor data indicates a total of 73 g of hydrogen generated during the test after correction for the helium release. This integral value includes

about 8 g of hydrogen believed to have been flushed by argon or due to meter sensitivity to moisture effects.

In addition to the on-line measurement of hydrogen, a gas sample from the collection tank was drawn into an evacuated sample bomb about 24 h after the test transient. Assay of the sample contents was determined by mass spectrometer analysis, indicating  $64 \pm 7$  g of hydrogen in the collection tank. The mass-spectrometer collection tank results for helium and  $N_2$  ( $1.5 \pm 0.4$  g and  $29 \pm 4$  kg, respectively) were compared with the quantities of these gases expected from the known helium fuel rod gas fill and separator nitrogen inflow rates. The expected quantities of helium and  $N_2$  were  $1.71 \pm 0.04$  and about 28.2 kg, respectively. Consequently, 91% of the bundle helium content and 102% of the  $N_2$  supplied to the separator can be accounted for from the collection tank gas sample results. These results indicate that the collection tank gas sample provided a reasonably good indication of the collection tank gas contents. The  $\pm 7$  g uncertainty in the  $H_2$  measurement was assessed from the uncertainties in the measured pressure, volume, and  $H_2$  data. The collection tank measurement of  $64 \pm 7$  g is in reasonable agreement with that amount estimated from the on-line measurement of 73 g. The collection tank result is considered to be the best estimate of total  $H_2$  generation for the SFD 1-1 experiment.

In addition to the measurement of hydrogen release, a perspective of the overall time-dependence of zircaloy oxidation for the SFD 1-1 transient can be obtained from inspection of the cladding thermocouple data.

**Table 5. Estimated mass of hydrogen trapped in dead space above the fallback barrier**

System Parameters:

$$\begin{aligned} P &= 6.9 \text{ MPa} \\ T &= 540 \text{ K} \\ R_u &= 0.0082 \frac{\text{MPa} \cdot \text{liter}}{\text{g mole K}} \\ M &= 2 \text{ g-}H_2/\text{mole-}H_2 \\ R &= R_u/M = 0.0041 \text{ MPa-L/g K} \end{aligned}$$

Calculation:

$$\begin{aligned} \rho &= P/RT \\ \rho &= \frac{6.9 \text{ MPa}}{0.0041 \frac{\text{MPa} \cdot \text{L}}{\text{g} \cdot \text{K}} (540 \text{ K})} = 3.12 \text{ g/L} \\ M &= 3.12 \text{ g/L} \times 2.5 \text{ L} = 7.8 \text{ g-}H_2 \end{aligned}$$

## Thermocouple Data

The cladding thermocouples as a whole provided reliable data up to ~1860 s. Between 1860 and 2060 s, some of the cladding thermocouples shunted at about 2000 K and formed new junctions via relocation. Figure 19 shows comparison plots of the six measured cladding inner surface temperatures and the SCDAP-calculated temperatures at each of the 0.35-m, 0.50-m and 0.70-m elevations up to the time of thermocouple junction relocation. Figure 20 compares the cladding temperature and fuel centerline temperature of Rod 4B at the 0.70-m elevation. The fuel centerline temperature is indicated to be essentially the same as the cladding

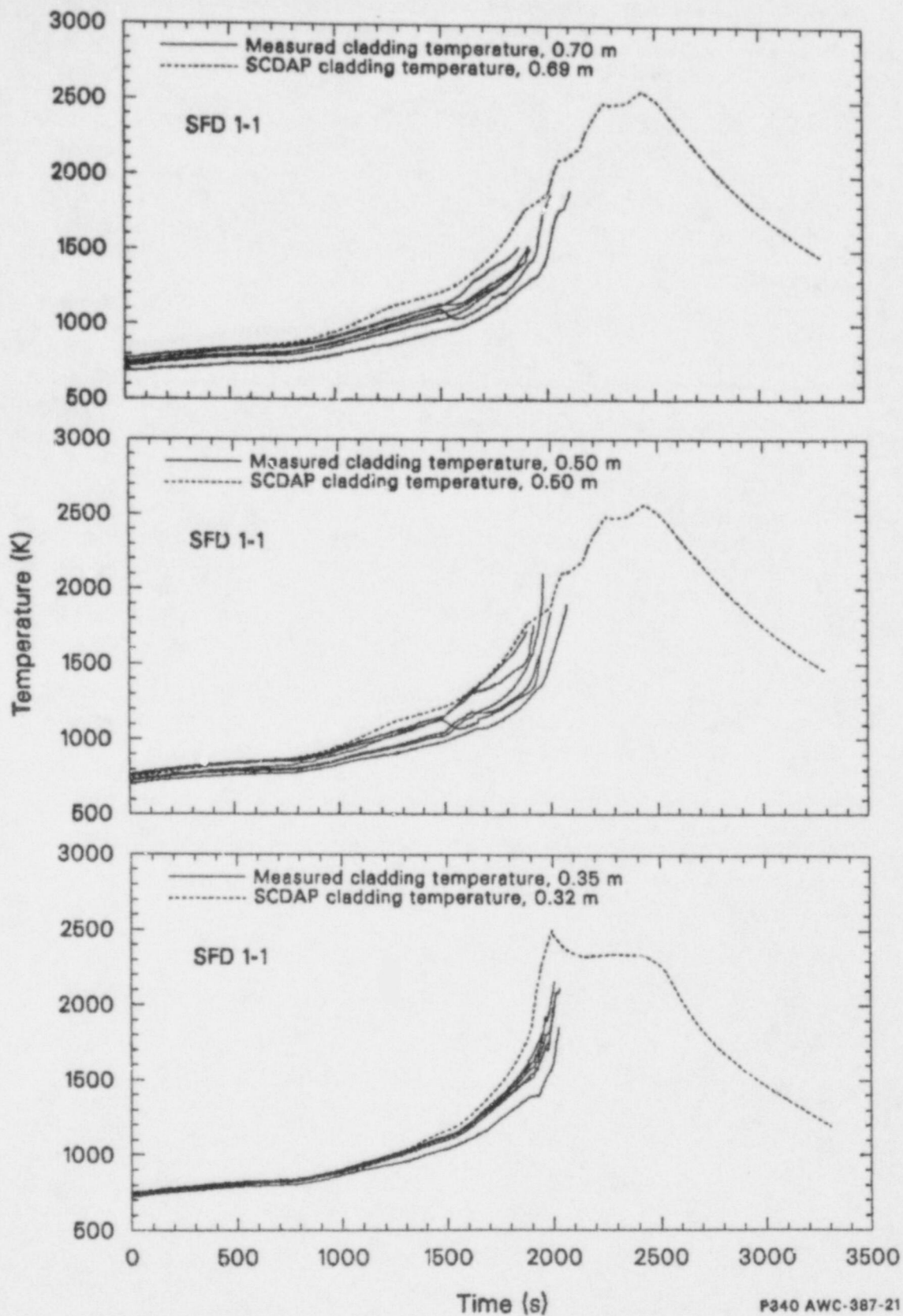


Figure 19. Comparison of the SFD 1-1 measured and SCDAP-calculated cladding temperatures at the 0.35-, 0.5-, and 0.7-m elevations.



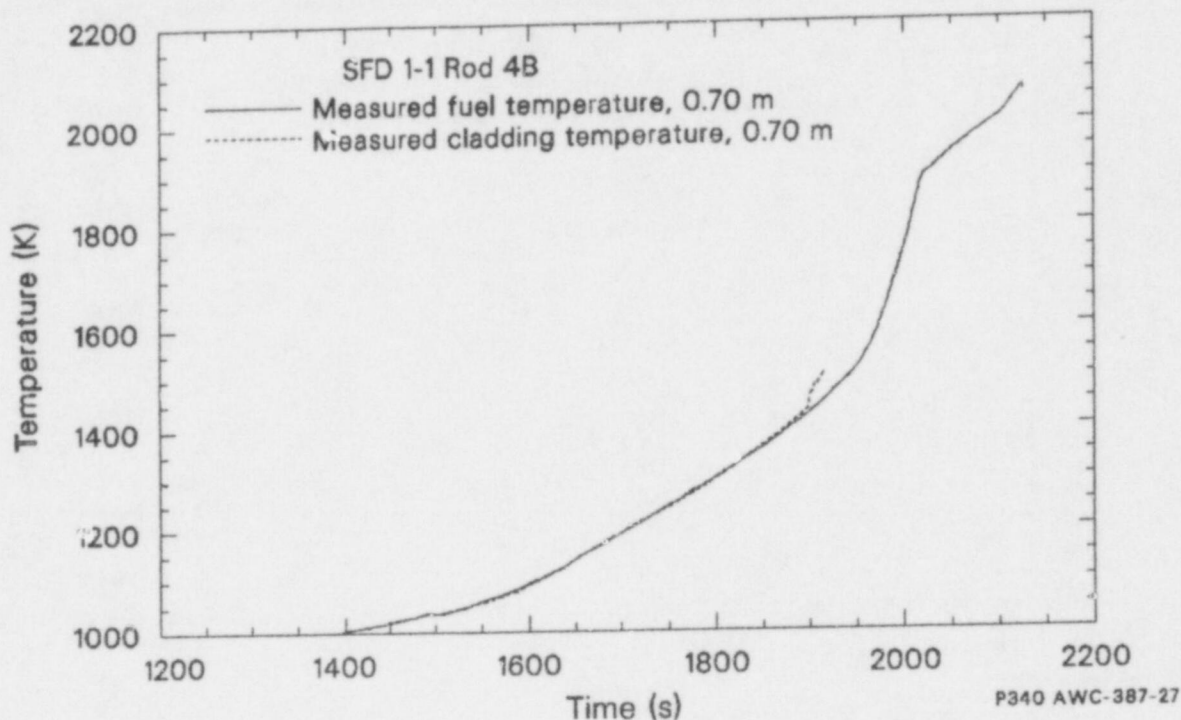


Figure 20. Comparison of the SFD 1-1 measured cladding and fuel centerline temperatures on Rod 4B at the 0.70-m elevation.

temperatures, while the thermocouples were operational. A close examination of the fuel and cladding temperatures for Rod 4B indicates that the fuel temperature exceeded the cladding temperature by less than 5 K up to 1325 K. However, between 1325 K and the temperature at which the thermocouples failed, the cladding temperature exceeded the fuel temperature by up to 50 K, indicating an increasing oxidation rate.

Figure 21 presents the measured cladding temperature response of the peripheral Rod 3F. The onset of rapid heatup is indicated to have first occurred at the 0.35-m elevation, then at the 0.5-m elevation, and then at the 0.7-m elevation. Rapid heatup evidently propagated upwards on the periphery of the bundle. Data from the middle row (Rod 4B) also indicate that the onset of rapid heatup started at lower elevations and moved upwards. However, data from the inner row (Rod 3D) indicate that rapid heatup began at the bundle first at the 0.5-m elevation (at 1900 s) and then propagated downwards. Thus, it appears that rapid heatup began near the radial and axial center of the bundle, propagating downwards and then radially outwards and upwards through the outer regions of the bundle.<sup>11</sup>

## Summary of Posttest Bundle Examination Data

Posttest examination of bundle geometric characteristics and assay of zircaloy oxidation were also conducted and are summarized here. The detailed data are presented in Reference 11.

**Bundle Geometric Characteristics.** Although posttest pressure drop measurements over the bundle length and computerized tomographic reconstruction of the degraded bundle give qualitative information on the extent of flow area degradation, the most reliable blockage data were obtained from posttest examination of the bundle. Eleven metallographic cross-section samples, at the 0.041-, 0.066-, 0.092-, 0.117-, 0.232-, 0.333-, 0.460-, 0.612-, 0.739-, and 0.879-m elevations, were examined to assay for the extent of flow blockage.

Extensive saddle collapse necessitated that the posttest assay of the extent of bundle reconfiguration include allowance for saddle collapse. Ideally, it would be desirable to distinguish between blockage caused by saddle collapse and that due to relocation of molten and solid fuel rod debris. However, because of extensive bundle distortion, this could not be done. The 0.066-m sample shown

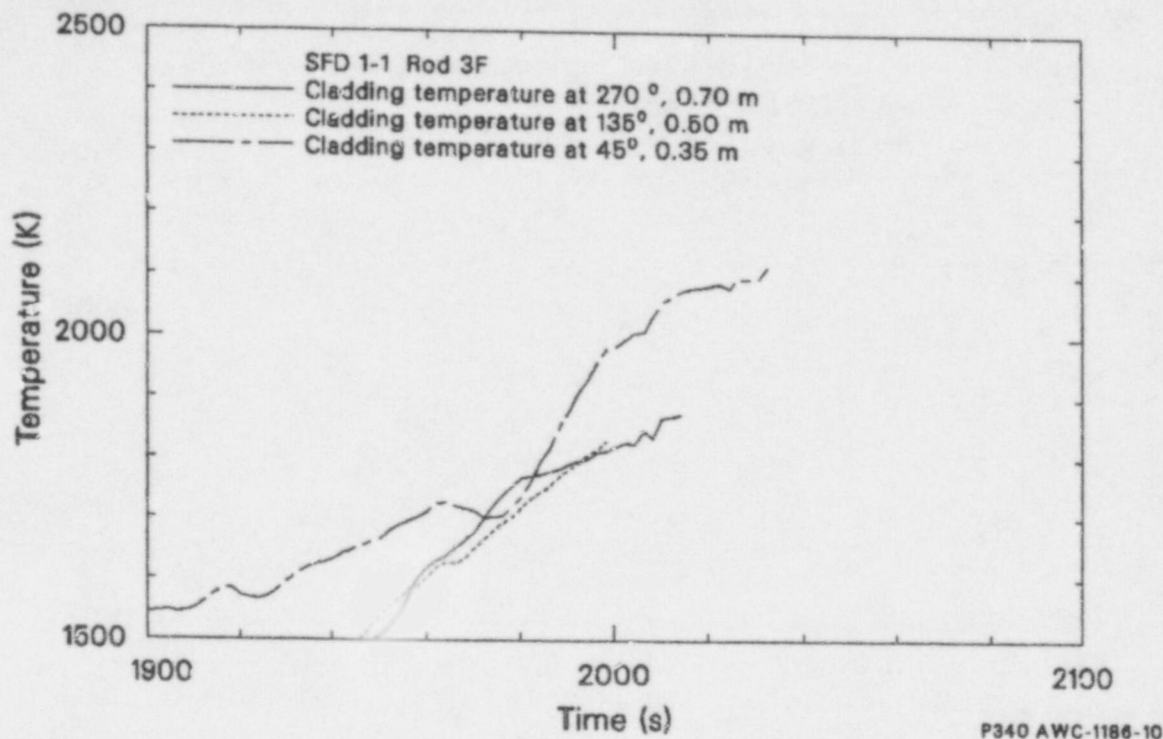


Figure 21. SFD 1-1 measured cladding temperatures on Rod 3F.

in Figure 22 was found to exhibit the highest degree of flow area restriction, with a total blockage area of approximately  $81.6 \text{ cm}^2$  inside the saddle,<sup>11</sup> where the pretest cross-sectional area occupied by various test components (e.g., fuel rods, liner, insulation) was approximately  $86.5 \text{ cm}^2$ . On this basis, the residual posttest open area for coolant flow at the 0.066-m elevation would nominally be  $4.9 \text{ cm}^2$ . However, porosity was found in some of the ceramic melt debris and insulation material, which would increase somewhat the open flow area if such porosity were true flow channels rather than sealed pores. Neglecting porosity effects, the metallographic data indicate a minimum flow area of about  $4.9 \text{ cm}^2$ .

As mentioned in the discussion of the SFD-ST blockage data, although uncertainties exist with respect to the specification of a degraded flow area based on posttest metallographic results, such uncertainties do not alter conclusions regarding steam flow through the degraded SFD 1-1 bundle. Steam venting calculations presented in the Analysis section of this report indicate that a flow area blockage in excess of 98% (residual flow area of  $\sim 0.65 \text{ cm}^2$ ) would be required to inhibit the  $0.64\text{-g/s}$  flow through the degraded SFD 1-1 bundle. Thus, the uncertainty of the nominal degraded flow area can be in the range of  $4.9 \pm 4.25 \text{ cm}^2$  with-

out alteration of the conclusions regarding blockage effects on flow stagnation.

**Bundle Oxidation Characteristics.** There were several components in the test train that had the potential to oxidize and release hydrogen during the transient, namely the fuel rod cladding, the zircaloy saddle, the zircaloy inner liner, the end caps, the fallback barrier, and the fuel. As indicated in Reference 11, large uncertainties exist in the PIE estimate of hydrogen generation. Estimates of total hydrogen generation from these components are given in Table 6. The first column presents the maximum possible  $\text{H}_2$  generation based on the available zirconium, while the second column lists the extent of oxidation for the various components estimated from posttest metallographic examination of the test debris.

As indicated, oxidation of zircaloy in the relocated previously molten debris can be an important contributor to the overall hydrogen generation process, yielding about half the total based upon extrapolation of the metallographic data. The fact that most of the oxidized previously molten debris was found in the lower regions of the bundle is indirect evidence that previously molten relocated

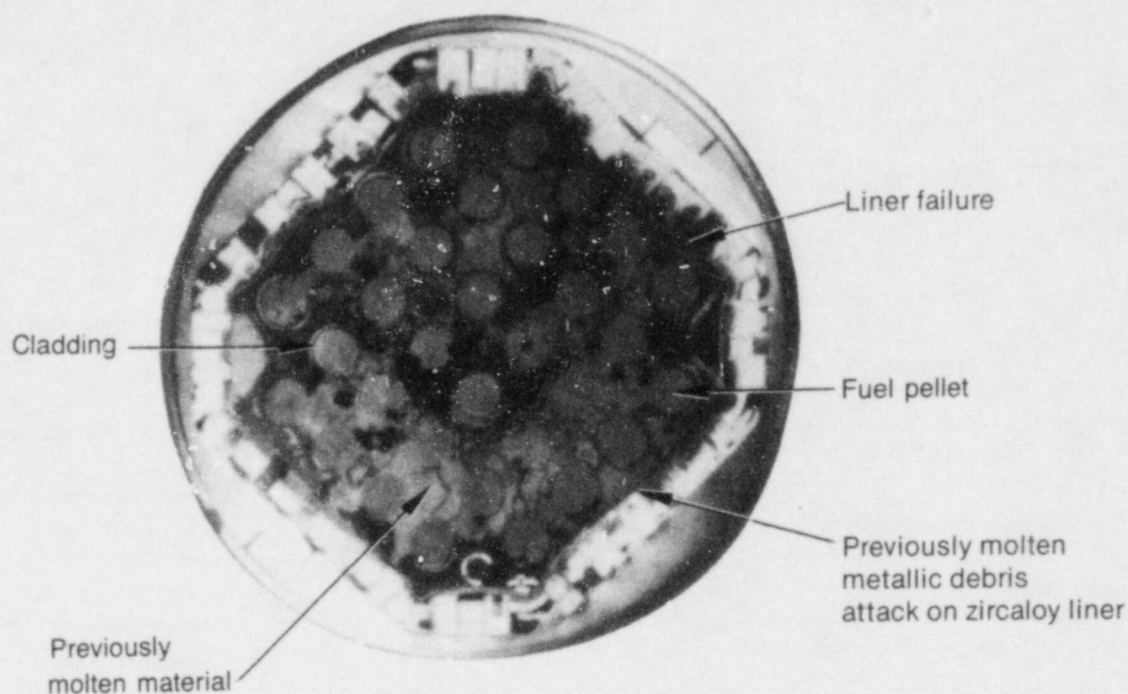


Figure 22. Posttest metallographic cross section of the SFD 1-1 bundle at 0.066 m.

Table 6. Potential sources of hydrogen generation and metallographic results for Test SFD 1-1

Source	Hydrogen Generation (g)	
	Upper Limit	Metallographic Estimate
Intact cladding	155	37.0
Oxidized melt <sup>a</sup>		50.1
Upper end caps	12	2.5
Lower end caps <sup>b</sup>	21	0.0
Shroud inner liner <sup>c</sup>	73	12.3
Lead carriers	6	0.0
Shroud saddle <sup>c</sup>	593	1.6
Fallback barrier <sup>d</sup>	22	0.0
Total	882	103.5

a. Assuming 14% internal porosity in melt.

b. Based on the standard, non-instrumented fuel rod end cap.

c. Based on the region from the bottom of the fuel up to the bottom of the steamline.

d. Portion of the fallback barrier up to the bottom of the steamline.



zircaloy can be a significant contributor to overall hydrogen generation.

Figure 23 illustrates some of the principal observations concerning SFD 1-1 melt debris oxidation. Shown is the metallography of a rod stub (Rod 6D) embedded in previously molten relocated debris at the 0.117-m elevation. The  $\text{UO}_2$  fuel pellet appears to be partially dissolved by previously molten ceramic  $(\text{U,Zr})\text{O}_2$  material, sandwiched between the fuel and still-intact completely oxidized cladding. Since molten  $\alpha\text{-Zr(O)}$  cannot completely reduce  $\text{UO}_2$  to form a ceramic  $(\text{U,Zr})\text{O}_2$  phase, the molten material inside the cladding must have been partially oxidized by steam ingress. Outside the intact cladding is another layer of previously molten ceramic material. The oxidized cladding remnant indicates partial chemical attack at the outside surface by the previously molten material. Since a ceramic  $(\text{U,Zr})\text{O}_2$  material would not dissolve  $\text{ZrO}_2$ , the partial dissolution of the cladding remnant is evidence that the molten debris must have initially been a metallic that began to attack the oxidized cladding and then was subsequently oxidized in place by steam. Both the previously molten ceramic phase inside and outside the cladding are perforated with pores, which would have allowed for steam ingress and oxidation of the previously molten material. This type of oxidation of previously molten debris is mainly evident in the lower regions of the bundle and is associated with relocated metallic melt. Further observations relative to overall SFD 1-1 bundle oxidation behavior are presented in Reference 11. Additional insight into bundle events affecting hydrogen generation was also obtained by test simulation using the SCDAP and MAAP codes.

## Code-Predicted Oxidation Behavior

Analysis of the SFD 1-1 test was also performed with the SCDAP<sup>16</sup> and IDCOR-MAAP<sup>7,17</sup> codes. Here, a summary description is presented of such predictions relative to oxidation and hydrogen behavior.

**SCDAP Predictions.** In an attempt to decouple SCDAP code-predicted oxidation behavior from thermal-hydraulic modeling uncertainties, the measured coolant level shown in Figure 15 was used as a code input parameter. (Additional coding input parameters and assumptions are discussed in Reference 11.) Comparison plots of the measured and SCDAP-calculated cladding temperatures are

shown in Figure 19 for the 0.35-, 0.50-, and 0.70-m elevations. A summary of comparative results is given in Table 7, which indicates that the SCDAP-calculated heatup rate up to 1300 K was about 10% higher than the measured heatup rate. The SCDAP-calculated heatup rate from 1300 to 2000 K, however, was about 36% lower than measured.

As discussed in Reference 11, uncertainties in the actual timing and magnitude of the hydrogen generation rate and the axial distribution of oxidation in the bundle prevent a quantitative assessment of the oxidation and hydrogen generation models in SCDAP. Therefore, SCDAP results are limited to integral comparisons between the measurements and the calculation. The total hydrogen production predicted by SCDAP was 89 g. This value is greater than the collection tank value of  $64 \pm 7$  g. The SCDAP analysis predicted a hydrogen production of 89 g, which is about 40% greater than the nominal collection tank value (considered to be the most accurate data for SFD 1-1). The overprediction of hydrogen production by SCDAP was probably caused by an overprediction of cladding temperatures during heatup. In addition, actual hydrogen generation during the later stages of the test may have been reduced by bypass of the steam around some of the bundle, due to partial flow blockage in the lower bundle region. Channeling of the steam through only part of the bundle would tend to decrease the overall hydrogen production.

The metallographic data indicate essentially complete zircaloy oxidation of the blockage region. Although the SCDAP simulation overpredicts total hydrogen production for the SFD 1-1 test, it underpredicted oxidation of relocated debris by a factor of two and overpredicted oxidation in the upper intact regions of the bundle. Although these two effects tend to cancel each other, the actual SFD 1-1 bundle oxidation characteristics were not well modeled by SCDAP once loss of geometry occurred. This was also the case for the SCDAP prediction for the SFD-ST experiment.

**MAAP Predictions.** The MAAP (Modular Accident Analysis Program) severe accident analysis code<sup>7</sup> has been developed as part of the IDCOR Program. Separate models were developed for BWR cores with canned fuel assemblies versus open lattice PWR geometry. The generalized models are shown schematically in Figure 24. The MAAP zircaloy oxidation model is governed by the Cathcart-Pawel equation for zircaloy temperatures less than 1850 K and the Baker-Just equation for higher temperatures, which would produce similar initial oxidation behavior as SCDAP. However, an important assumption of the MAAP-BWR code is

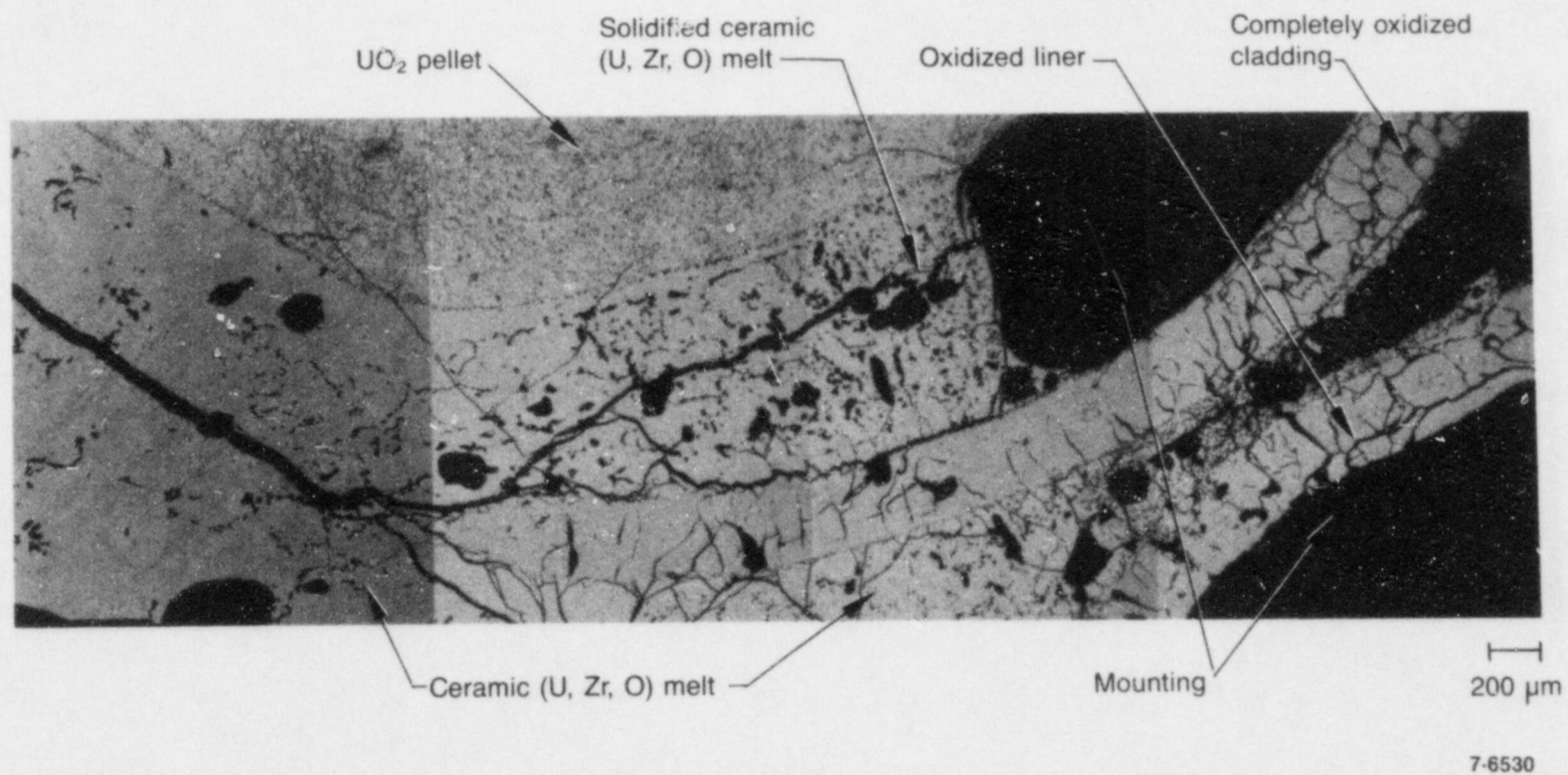


Figure 23. Illustration of deformed Rod 6D SFD 1-1 cladding and liner remnants at the 0.117-m elevation, where the fuel and oxidized cladding are shown to be partially dissolved by the previously molten metallic debris that has been oxidized by steam to a ceramic condition.

Table 7. Comparison of measured and SCDAP-calculated results

Parameter	Elevation (m)	Measured	SCDAP Calculation
Cladding heatup rate from 1000 to 1300 K (K/s)	0.35	0.68	0.79
	0.50	0.61	0.58
	0.70	0.61	0.72
Time to attain 1300 K (s)	0.35	1708	1637
	0.50	1788	1605
	0.70	1812	1579
Cladding heatup rate from 1300 to 2000 K (K/s)	0.35	2.3	2.5
	0.50	2.9	1.7
	0.70	3.4	1.3
Time to attain 2000 K (s)	0.35	2009	1912
	0.50	2033	2024
	0.70	2017	2132
Maximum temperature attained (K) <sup>a</sup>	0.35	2660 ± 10%	2501
	0.50	2435 ± 10%	2566
	0.70	2435 ± 10%	2510

a. Measured maximum fuel rod temperatures were assessed from positron metallography.

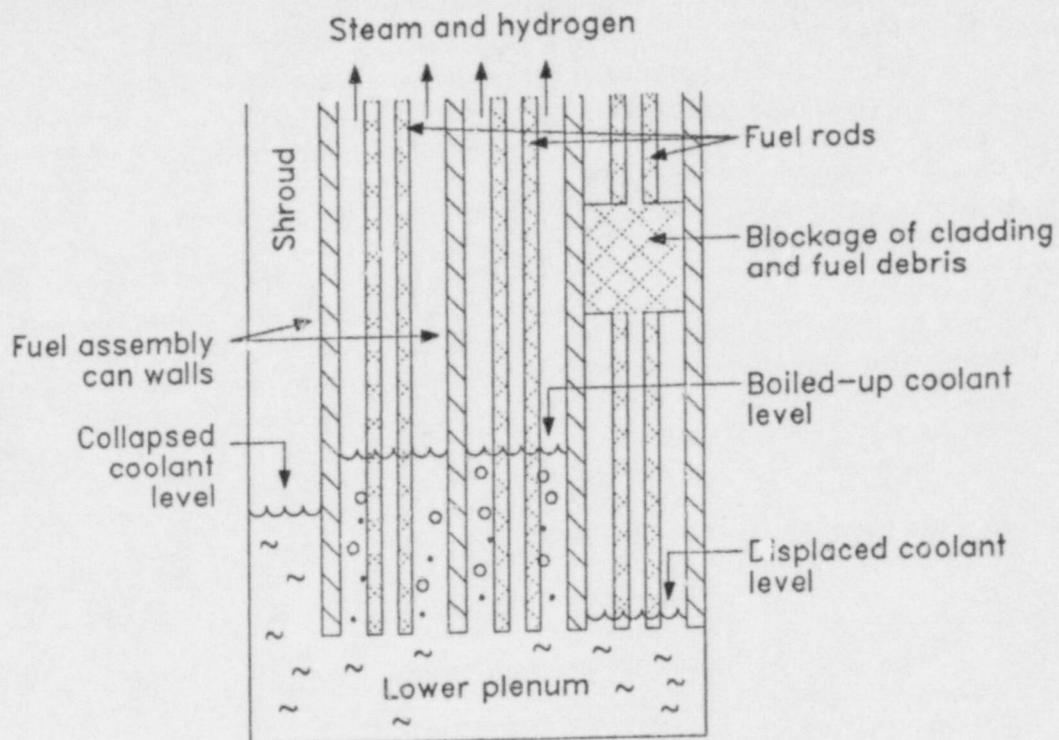
that when the  $\alpha$ -Zr(O)/UO<sub>2</sub> dissolution temperature (2170 K) is reached, downward melt relocation commences which is counteracted by upwardly flowing steam. If the MAAP-BWR levitation (flooding) criterion is not satisfied, blockage formation is assumed and oxidation is substantially reduced or prevented. The conceptual basis for this viewpoint stems primarily from two factors. The first relates to an altered surface area for reaction, where it is argued that loss of rod geometry results in an effective reduction in the zircaloy surface-to-volume ratio and thus diminished oxidation. The second relates to altered thermal-hydraulic conditions, where liquefied fuel-clad material slumping and blockage formation would divert steam flow from the degraded region of the core, thereby inhibiting steam supply and thus oxidation/hydrogen production on a local basis. For both PWR and BWR geometries, the effect of a reduction in zircaloy surface-to-volume ratio would be similar; however, differences exist with respect to the thermal-hydraulic/blockage effect.

As illustrated in Figure 24, for an open-lattice PWR core local blockage can occur when zircaloy melting and relocation commence, causing steam flow to be redistributed to unblocked regions and

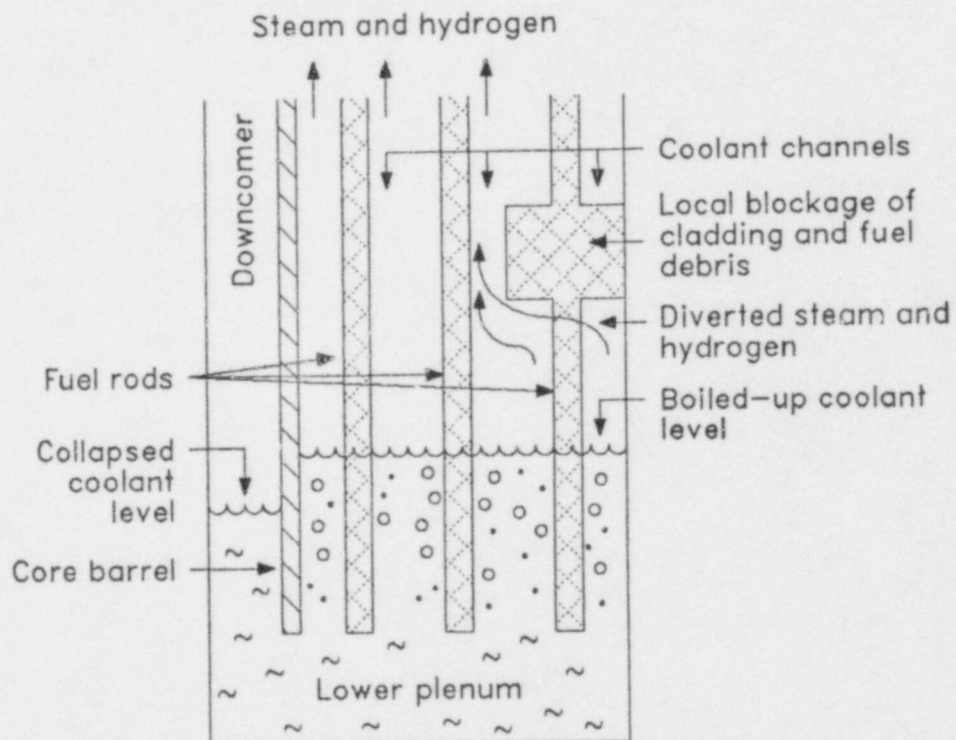
terminating the oxidation process in the blocked node only. For segmented BWR geometry with canned fuel assemblies, clad melting and relocation are assumed "a priori" to lead to a blocked fuel assembly which terminates hydrogen production. As a result, boiloff and further oxidation in the degraded BWR assembly is essentially terminated at the  $\alpha$ -Zr(O)/UO<sub>2</sub> dissolution temperature (2170 K) or zircaloy melting point (~2250 K), although delayed somewhat until levitation effects are overcome.

In the IDCOR analysis of the SFD 1-1 test,<sup>17</sup> the BWR/HEATUP version of the MAAP code was used. The following data were used as input to the MAAP-code analysis: the test bundle and fuel rod geometry, system pressure, inlet flow and temperature, the fission power history, and the axial power distribution. The code output available for comparison with test data is the cladding temperatures before thermocouple melting (~2250 K) and the rate (g/s) and total (g) hydrogen production. The SFD 1-1 fuel bundle was modeled as a single fuel assembly, where the zircaloy liner was treated as the BWR channel wall. The shroud heat losses were modeled by a user-specified heat transfer coefficient. Additional assumptions are that the pressure





MAAP generalized BWR core configuration



MAAP generalized PWR core configuration

P383-KM267-03

Figure 24. Illustration of MAAP core geometry models for BWR and PWR systems.

spikes noted in the test had little impact on overall hydrogen generation and were ignored, and that the inlet flow and its temperature remained constant. The calculation assumed that all steam generated was forced through the bundle and thus available for oxidation.

Figure 25 presents a comparison of the measured versus MAAP-calculated boil-down level for the SFD 1-1 test.<sup>17</sup> The calculation agrees well with the measurement until -15 min, where the measured water level is shown to decrease. This divergence between MAAP-calculated boil-down behavior versus actual measured behavior has a large impact on implications relative to hydrogen generation. The steam generation rate calculated by MAAP is between 0.9 and 1.0 g/s during the 1200 to 2400-s time period of the test, while the measured water level indicates a steaming rate of about 0.64 g/s over the same period. The late boil-down calculated by MAAP, which supplies an overly high steam flow during this critical period of high-temperature cladding oxidation [at 2200 s,  $T_{\text{clad}}$  (MAAP) = 2600 K], results in an overestimate of the hydrogen production; i.e., 110 g calculated by MAAP versus  $64 \pm 7$  g from the collection tank measurement. Two reasons were stated in Reference 7 for this discrepancy: (a) a lower actual steam generation rate, which would have produced approximately 82 g of hydrogen estimated by MAAP; and (b) reduction in the oxidation rate in the degraded SFD 1-1 bundle due to a decrease in the surface-to-volume ratio and potential effects of steam flow diverted away from the relocated zircaloy debris. It was concluded in Reference 17 that if a parallel flow path had existed in the SFD 1-1 bundle, the higher hydraulic resistance in the degraded channel would have diverted steam to an undegraded channel, thereby terminating further oxidation/hydrogen generation in the degraded bundle.

Because the MAAP prediction of 110 g hydrogen was higher than the actual measured hydrogen generation (i.e., hydrogen monitor data  $\sim 73$  g; PIE metallography  $\sim 103$  g; collection tank  $\sim 64$  g), it was postulated<sup>17</sup> that the SFD 1-1 data suggest a reduction in hydrogen generation upon zircaloy melting and relocation. However, several points contradict this contention. First, the MAAP-calculated boil-down history resulted in a higher predicted boil-down steaming rate (0.9 to 1.0 g/s calculated versus  $\sim 0.64$  g/s actual) near the end of the test, when fuel rod temperatures were highest. The overprediction of steam supply results in an overestimate of hydrogen production. When the measured boil-down history was used as input to the code, the predicted total hydrogen generation was reduced to 82 g, which is in closer agreement with the collection tank data ( $64 \pm 7$  g). Secondly, the metallographic data indicate a high degree of oxidation of the previously molten relocated debris in the lower regions of the bundle. Upwards of half of the total amount of oxidation (see Table 6) was found to be associated with oxidation of the melt debris, which contradicts the postulate of diminished oxidation after zircaloy melting. Likewise, a comparison of the on-line thermocouple and hydrogen monitor data (see following section) indicates that most of the SFD 1-1 oxidation occurred at temperatures close to and above the  $\alpha$ -Zr(O)/UO<sub>2</sub> dissolution temperature (2170 K). These data present a good case for extensive oxidation of molten zircaloy during loss of rod geometry.

In the following section, a detailed interpretation of the SFD-ST and SFD 1-1 test data is presented with respect to severe accident hydrogen generation issues.

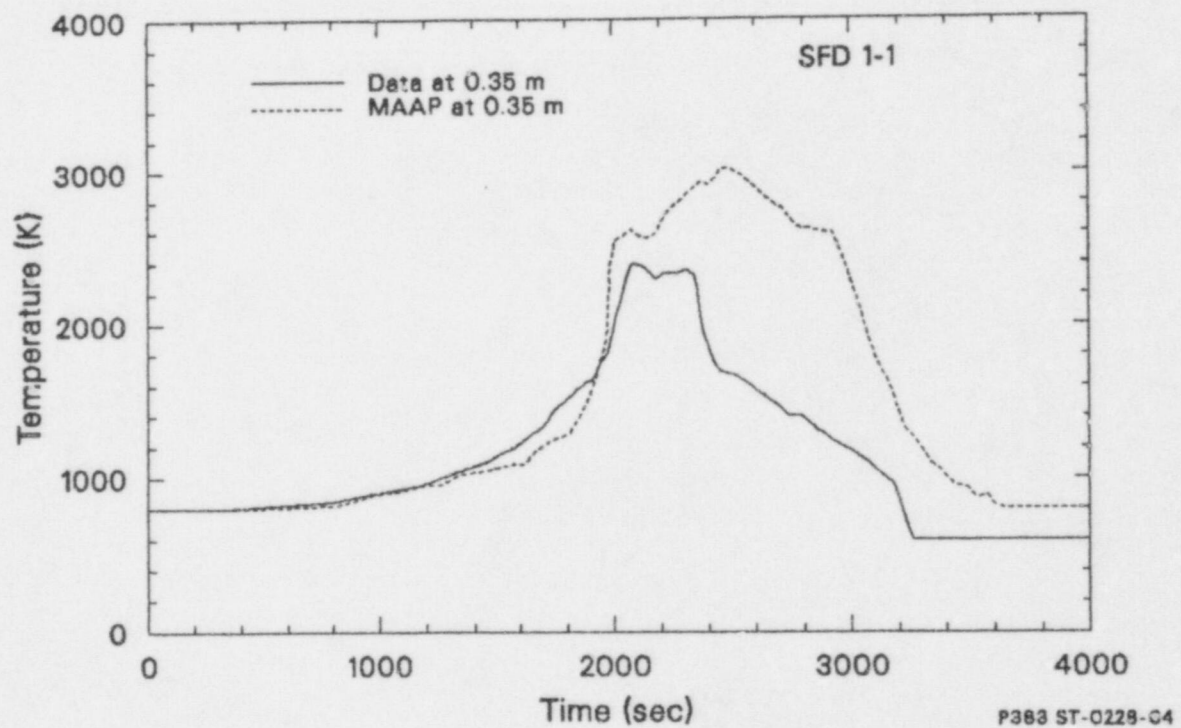
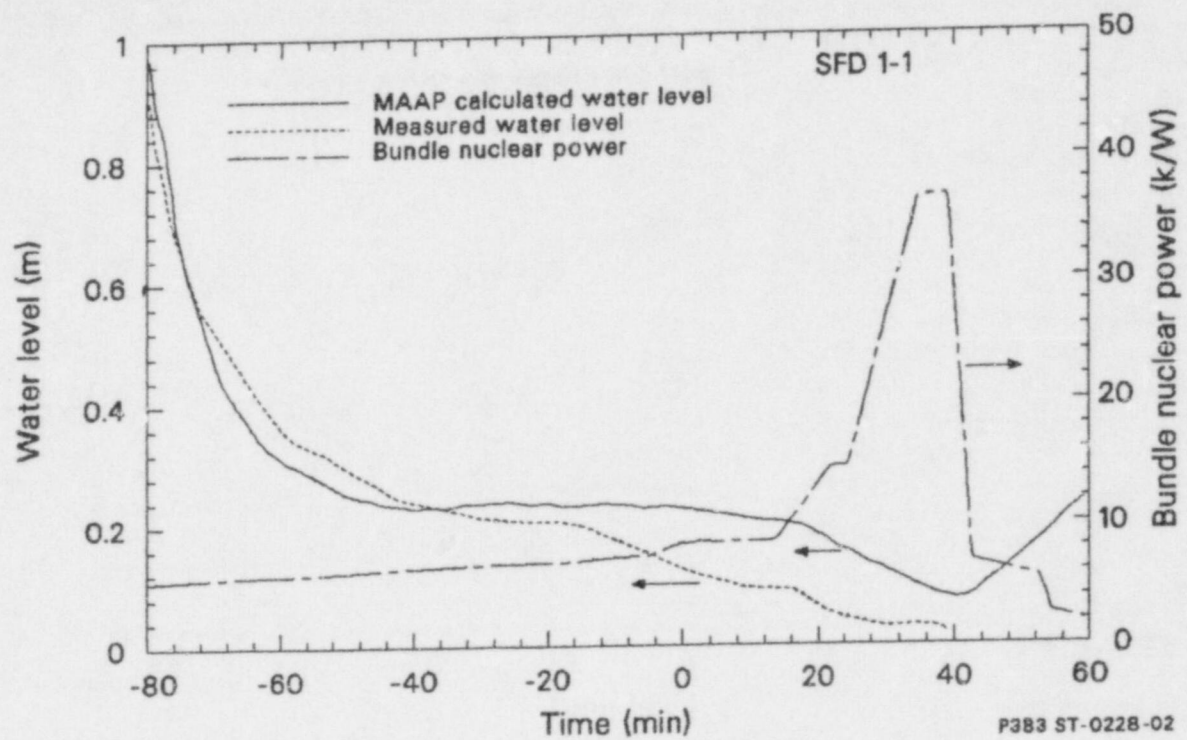


Figure 25. Comparison of SFD 1-1 measured and MAAP-calculated water level and cladding temperatures.

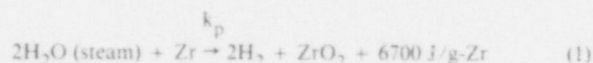


## ANALYSIS OF THE SFD-ST AND SFD 1-1 HYDROGEN GENERATION DATA

As mentioned in the Introduction, the principal outstanding issues related to in-vessel hydrogen generation under severe accident conditions concern high-temperature oxidation behavior, specifically the influence of zircaloy melting and fuel dissolution on oxidation and fuel bundle reconfiguration effects which may divert steam flow from the degraded bundle and alter hydrogen generation characteristics. These issues are discussed here in the context of findings noted from analysis and interpretation of the SFD-ST and SFD 1-1 test data. First, however, a brief overview of hydrogen source term issues is presented.

### Perspective on Hydrogen Source Term Issues

The major in-vessel source of hydrogen generation is due to the reaction of zircaloy cladding with steam. To a lesser degree, oxidation of stainless steel and fuel to a hyperstoichiometric condition can also add to the total hydrogen produced. This report primarily concerns zircaloy oxidation, which is governed by the following chemical equation:



where  $k_p$  is the reaction rate constant. For each mole of zircaloy oxidized, two moles of hydrogen are generated and a significant amount of reaction heat is released (6700 J/g-Zr or 305 kJ/g-O at 1900 K<sup>18</sup>). The TMI-2 inventory of zircaloy cladding (~23,000 kg) can be used to illustrate the energetics and hydrogen generation characteristics of this reaction. Assuming 50% conversion of zirconium to  $\text{ZrO}_2$ , the reaction heat liberated is

$$Q_R \sim (11.5 \text{ E} + 6) (6.3 \text{ E} + 3 \text{ J/g}) = 7.25 \text{ E} + 10 \text{ J} \quad (2)$$

while the corresponding amount of hydrogen generated<sup>a</sup> is

$$m_{\text{H}_2} =$$

$$11.5\text{E} + 6 \text{ g-Zr} \left( \frac{\text{mole-Zr}}{91 \text{ g-Zr}} \right) \left( \frac{2 \text{ mole-H}_2}{\text{mole-Zr}} \right) \left( \frac{2 \text{ g-H}_2}{\text{mole-H}_2} \right) \quad (3)$$

$$= 506 \text{ kg}$$

Because of the potentially large quantity of hydrogen that can be produced and the fact that the reaction heat accelerates core degradation, an understanding of in-core processes affecting zircaloy oxidation is of prime importance. The overall oxidation process is not only affected by chemical kinetics considerations, but also by the availability of steam, the zircaloy surface-to-volume ratio effects, and thermal-hydraulic conditions.

During the early intact-rod geometry phase of the accident, zircaloy oxidation is reasonably well understood. The isothermal reaction process can be expressed in terms of parabolic kinetics, where the mass of zirconium reacted per unit surface area ( $W$ ) is proportional to the square root of time, i.e.

$$W = (k_p t)^{0.5} \quad (4)$$

where

$$t = \text{time, s}$$

$$k_p = \text{parabolic kinetics,} \\ (\text{mg-Zr reacted/cm}^2)^2/\text{s}.$$

Such parabolic kinetics are governed by the oxygen diffusional characteristics, so that the rate constant  $k_p$  (analogous to the diffusion coefficient) can be expressed in terms of the temperature-dependent diffusional properties of the  $\text{ZrO}_2$  surface layer and the oxygen concentration conditions at the exposure surface and the  $\text{ZrO}_2/\alpha\text{-Zr(O)}$  interface.

The temperature-dependence of  $k_p$  can be described by the Arrhenius equation of the form

$$k_p = A \exp(-Q/RT) \quad (5)$$

where

$$A = \text{scaling constant}$$

$$Q = \text{activation energy}$$

$$R = \text{the universal gas constant.}$$

a. Estimates of the total hydrogen mass generated during the TMI-2 accident range between 450 to 580 kg.<sup>1</sup>

Table 8 presents the principal expressions developed for  $k_p$ .<sup>19-23</sup>

Prior to the TMI-2 accident, there had been only limited data reported on zircaloy oxidation kinetics above the 1770-K tetragonal-to-cubic phase transformation of  $ZrO_2$  (see Figure 26a). This phase transition, however, results in a discontinuous increase in the  $ZrO_2$  growth rate, implying oxidation kinetics above 1770 K that may be different than at lower temperatures. Prater and Courtright<sup>22,23</sup> recently investigated the oxidation kinetics of zircaloy-4 in steam at temperatures up to 2670 K. Although the  $ZrO_2$  and  $\alpha$ -Zr(O) layers displayed parabolic growth behavior over the entire temperature range studied, a discontinuity in the oxidation kinetics at 1770 K was found to cause rates to increase somewhat above those previously established by the Baker-Just<sup>21</sup> relationship. The temperature-dependence of the isothermal growth constants above 1770 K for the  $ZrO_2$  layer ( $\delta_o$ ) and the combined  $ZrO_2 + \alpha$ -Zr(O) layers ( $\delta_c$ ) were found to be best correlated by the following equations:

$$\delta_o = 5.46 \exp \left( \frac{-14,210}{T(K)} \right) (\pm 35\%) \text{ cm-s}^{-1/2} \quad (6)$$

$$\delta_c = 2.05 \exp \left( \frac{-11,550}{T(K)} \right) (\pm 42\%) \text{ cm-s}^{-1/2} \quad (7)$$

The  $ZrO_2$  growth rates using the above expressions are compared with those of Cathcart-Pawel<sup>19</sup>, Urbanic-Heidrick<sup>20</sup>, and Baker-Just<sup>21</sup> in Figure 27.<sup>23</sup> Above 1770 K, the Prater-Courtright growth rate is somewhat greater than that reported by Baker-Just, where a discrepancy of about 10%

exists. Nevertheless, general agreement exists on the parabolic nature of oxidation kinetics for solid zircaloy.

Although solid-state, fixed-geometry oxidation behavior is reasonably well understood, such is not the case at zircaloy temperatures exceeding that of  $\alpha$ -Zr(O) melting ( $\sim 2250$  K) and  $\alpha$ -Zr(O)/ $UO_2$  dissolution ( $\sim 2170$  K) (see Figure 26b). Uncertainty exists relative to the oxidation behavior of molten zircaloy, where disruption of the protective oxide layer and fuel dissolution effects can alter overall oxidation characteristics.

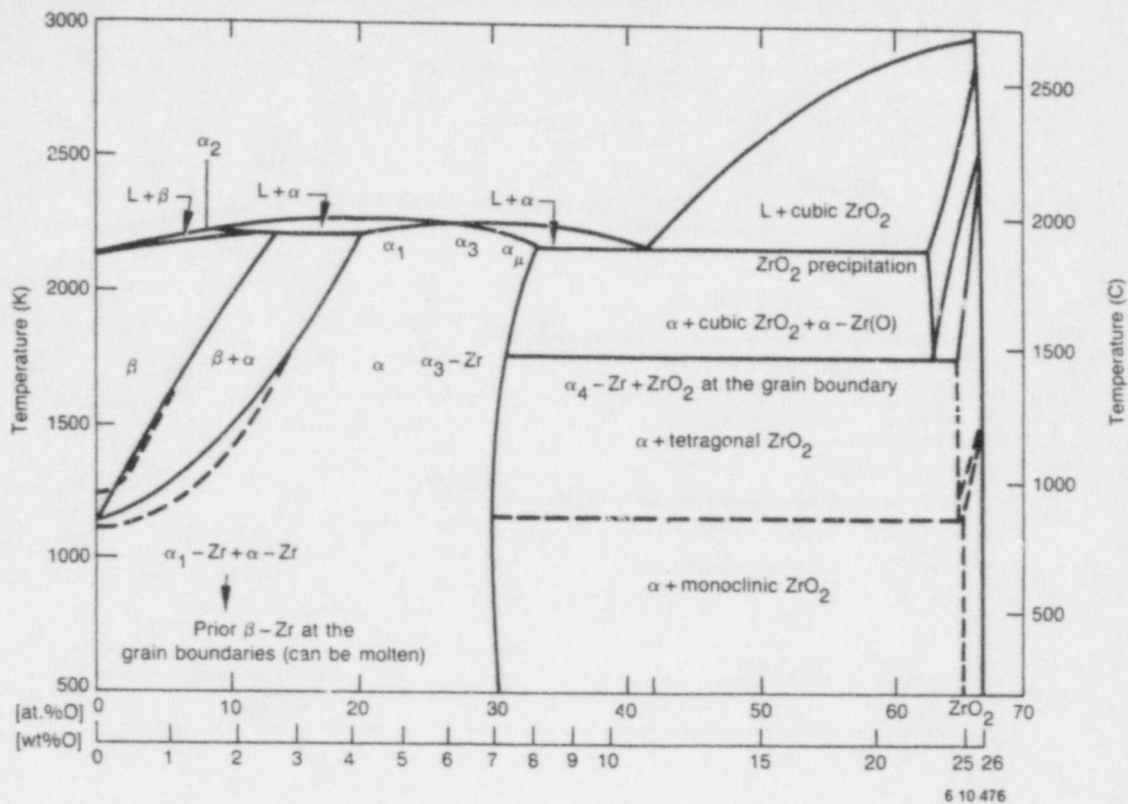
#### Oxidation Behavior of Molten Zircaloy.

Attempts have recently been made to assess the oxidation kinetics of liquid zircaloy by steam, most notably the analytical study of Olander<sup>24</sup> and the experimental investigations of Prater and Courtright.<sup>22,23</sup> In Olander's theoretical study, steam oxidation of molten zircaloy was analyzed as a two-medium [i.e. solid  $ZrO_2$  surface layer and molten  $\alpha$ -Zr(O) interior region], moving-interface diffusion problem. Typical thermophysical property values of the various oxygen-bearing phases of zircaloy are given in Table 9,<sup>25</sup> while oxygen diffusivity (D) correlations are presented in Table 10 and plotted in Figure 28 for  $\alpha$ -Zr(O) and  $ZrO_2$  as a function of temperature.<sup>26-32</sup> Olander's predictions indicate that the oxidation rate would be influenced mainly by the thickness of the  $ZrO_2$  surface layer and the fractional oxygen content of the molten  $\alpha$ -Zr(O) phase. Noting that oxidation kinetics is largely governed by the oxygen diffusional resistance in the  $ZrO_2$  surface layer, the results of Olander's study indicate the following trends. Although the diffusivity of oxygen in liquid  $\alpha$ -zircaloy is unknown, it can be expected to be of similar magnitude as that for solid  $\alpha$ -Zr(O). Thus, if molten  $\alpha$ -Zr(O) is below its oxygen

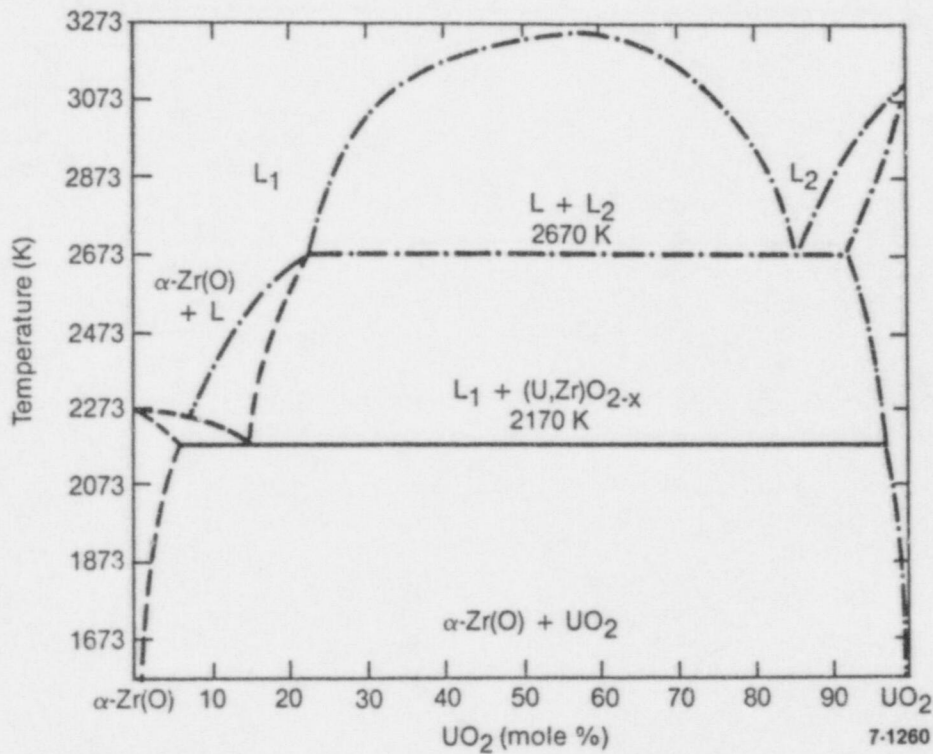
Table 8. Arrhenius correlations for the parabolic rate constant

$k_p$ [(mg-Zr reacted/cm <sup>2</sup> ) <sup>2</sup> /s]	Temperature Range (K)	Reference
$2.94 \text{ E} + 6 \exp(-39,940/RT)$	$T < 1800$	Cathcart-Pawel
$8.79 \text{ E} + 5 \exp(-33,000/RT)$	$T > 1650$	Urbanic-Heidrick
$33.3 \text{ E} + 6 \exp(-45,500/RT)$	$T > 1650$	Baker-Just
$26.8 \text{ E} + 7 \exp(-52,350/RT)$	$T > 1770$	Prater-Courtright

$R = 1.987 \text{ cal/g-mole K}$



(a) Zirconium-oxygen equilibrium phase diagram.



(b) Equilibrium pseudo-binary phase diagram between UO<sub>2</sub> and oxygen-saturated alpha-phase zircaloy.

Figure 26. Zirconium-oxygen equilibrium and pseudo-binary  $\alpha$ -Zr(O)-UO<sub>2</sub> phase diagrams.



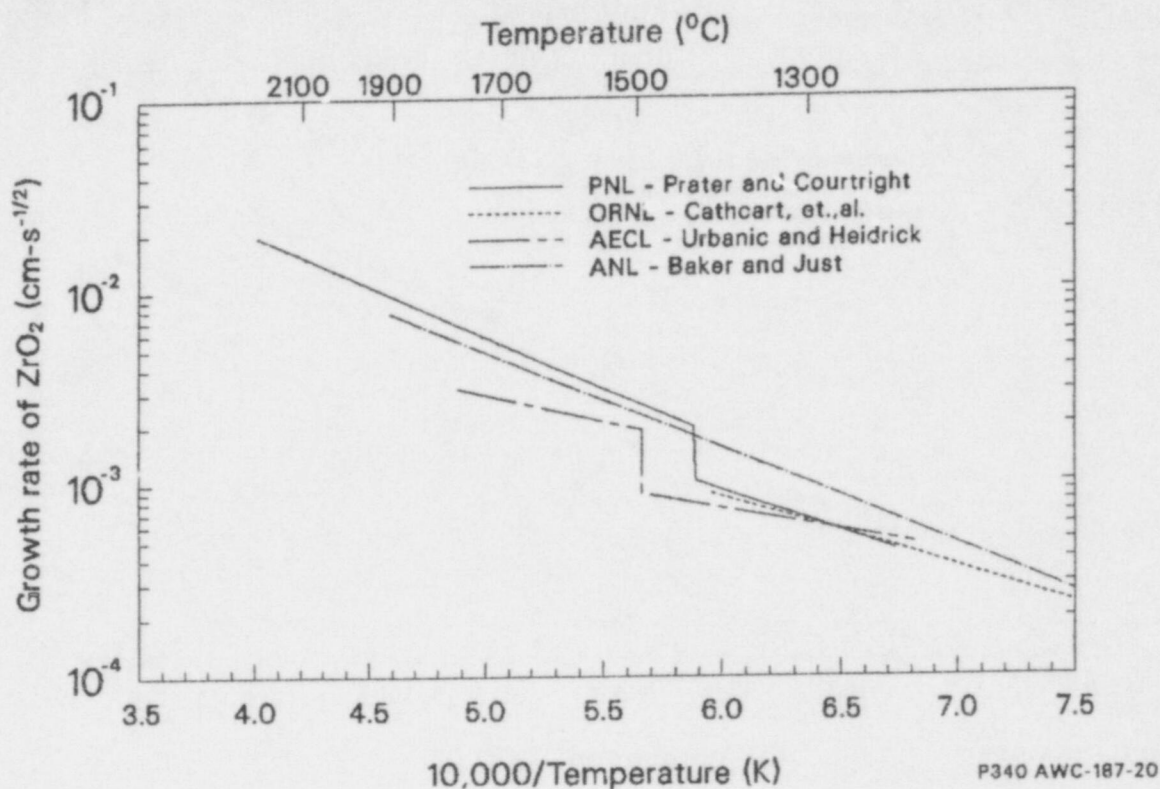


Figure 27. Comparison of parabolic growth-rate constants for oxide-layer growth.

saturation limit (i.e., less than 30 mol.% oxygen), it should partially dissolve  $\text{ZrO}_2$ . As the thickness of the  $\text{ZrO}_2$  layer is reduced, oxidation kinetics would be

accelerated. Once  $\alpha\text{-Zr(O)}$  reaches its saturation limit, dissolution of  $\text{ZrO}_2$  terminates and oxidation kinetics would be controlled by the growth of the  $\text{ZrO}_2$  layer.

**Table 9. Thermophysical properties of zircaloy cladding<sup>25</sup>**

Properties	Alpha-Zircaloy	Beta-Zircaloy	$\text{ZrO}_2$
Density <sup>a</sup> (g/cm <sup>3</sup> )	6.49	6.44	5.82
Specific heat (J/kg · K)	375	650	604.8
Thermal conductivity <sup>a</sup> (W/m · K)	19.6	28.5	2.2
Latent heat of fusion (J/kg)	2.25E + 5	2.25E + 5	7.06E + 5
Melting point (K)	2150	2125.0	2950.0
Boiling point (K)	—	3853.0	4548.0

a. For solid zircaloy at room temperature.

**Table 10. Arrhenius equations for oxygen diffusivity in zircaloy**

Oxygen Diffusion Coefficient	Diffusivity (D) (cm <sup>2</sup> /s)	Temperature Range (K)	Reference
Alpha-zircaloy	$0.196 \exp (-41,000/RT)$	$1273 < T < 1773$	Mallett et al
	$3.923 \exp (-51,000/RT)$	$1273 < T < 1777$	Pawel
	$0.0661 \exp (-44,000/RT)$	$563 < T < 923$	Ritchie/Atrens
	$16.5 \exp (-54,000/RT)^a$	$923 < T < 1773$	Ritchie/Atrens
Beta-zircaloy	$0.0453 \exp (-28,000/RT)$	$1273 < T < 1773$	Domagala/McPherson
	$0.0263 \exp (-28,000/RT)^a$	$1273 < T < 1773$	Perkins
ZrO <sub>2</sub>	$2.88 \times 10^{-4} \exp (-28,000/RT)$	$873 < T < 1123$	Rosa/Hagel
	$0.1387 \exp (-34,680/RT)^a$	$1274 < T < 1777$	Pawel
	$0.9 \times 10^{-3} \exp (-28,700/RT)$	$600 < T < 743$	Smith

a. Preferred expression when several correlations exist for the same temperature range.

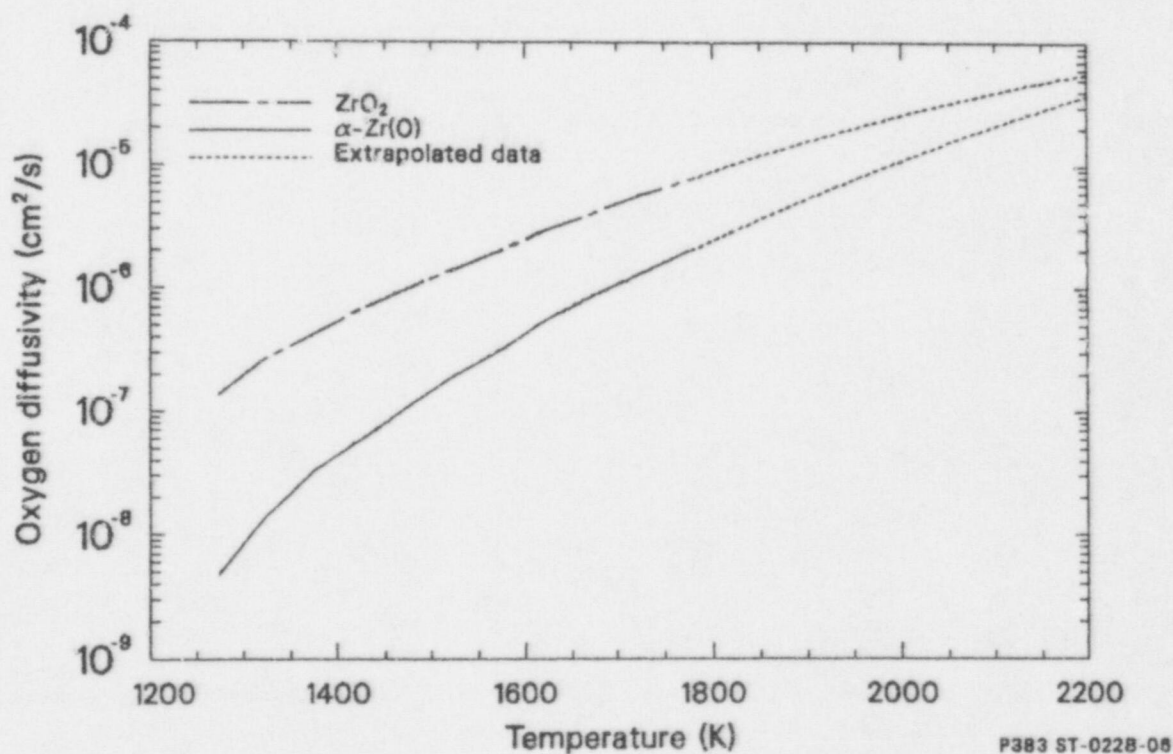


Figure 28. Temperature-dependence of the oxygen diffusivity in α-Zr(O) and ZrO<sub>2</sub> (Reference 27).

However, such observations apply only to the idealized configuration of a solid  $\text{ZrO}_2$  surface that remains fixed to an interior layer of molten  $\alpha\text{-Zr(O)}$ .

The theoretical observations of Olander appear to be in qualitative agreement with recent experimental trends noted by Prater and Courtright.<sup>22,23</sup> Several tests were conducted with zircaloy samples heated above the  $\alpha\text{-Zr(O)}$  melting point. The essential continuity of the oxide growth rate through the melting point of zircaloy supports the viewpoint that diffusion through the protective  $\text{ZrO}_2$  layer represents the rate-limiting step in the oxidation process. The rates observed in the Prater-Courtright study, however, represent oxidation behavior with a protective oxide layer, without breakout of  $\alpha\text{-Zr(O)}$  from the  $\text{ZrO}_2$  protective shell.

As illustrated in Figure 29, once zircaloy melting (2250 K) and fuel dissolution ( $\sim 2170$  K) commence, the destruction of the protective  $\text{ZrO}_2$  layer and attendant exposure of  $\alpha\text{-Zr(O)}$  to steam may tend to initially accelerate the reaction. Exposure of metallic zircaloy melt would thus result in enhanced oxidation, until the protective  $\text{ZrO}_2$  layer is reestablished. On the other hand, molten  $\alpha\text{-Zr(O)}$ -induced dissolution of  $\text{UO}_2$  may result in a reduced zircaloy surface-to-volume ratio, which would tend to decrease the overall reaction process.<sup>33-35</sup> These two competing effects contribute to the complexity of a mechanistic understanding of oxidation once the onset of fuel dissolution has commenced. However, analysis presented in Appendix C indicates that if  $\text{ZrO}_2$  breakup occurs and  $\alpha\text{-Zr(O)}$  is exposed to steam, then the oxidation rate can be expected to be similar to that of oxygen-free zircaloy. The question of molten zircaloy oxidation behavior is a principal area of interest in the evaluation of the PBF SFD-ST and SFD 1-1 data, as is the effects of loss of rod geometry.

**Fuel Bundle Reconfiguration Effects.** As mentioned in the discussion of the IDCOR-MAAP code simulation of the SFD 1-1 test, a governing assumption of the MAAP-BWR code is that when melt relocation occurs, oxidation may be substantially reduced or prevented. The conceptual basis for this assumption is shown in Figure 30. Consider the situation illustrated, where cladding melting and relocation in the center channel leads to a blocked or nearly blocked channel, resulting in pressurization below the blockage region and the attendant potential for diversion of residual water in the bottom of the degraded assembly to adja-

cent unblocked assemblies. As a result, boiloff and further oxidation in the degraded BWR assembly is terminated in the IDCOR MAAP-BWR code once zircaloy melting and downward melt relocation occur. As will be discussed later in this section, nearly total flow area blockage would be required to terminate steam flow through a degraded channel.

## Evaluation of the SFD-ST and SFD 1-1 Test Data

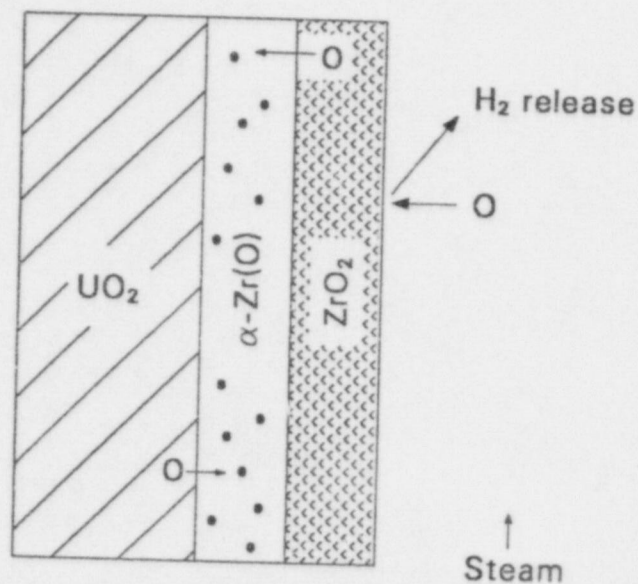
In this section, the effects of (a) zircaloy melting and fuel dissolution on oxidation behavior and (b) fuel bundle reconfiguration effects which may alter steam flow and hydrogen generation characteristics are addressed in terms of the SFD-ST and SFD 1-1 test data.

**Oxidation Behavior of Molten Zircaloy.** To assess the influence that zircaloy melt and fuel dissolution exert on oxidation behavior and hydrogen production, the hydrogen release and cladding thermocouple data for the SFD-ST and SFD 1-1 tests were compared.

As discussed previously, the SFD-ST hydrogen monitor data are reliable only prior to 200 min, since high hydrogen concentrations later in time significantly diminished meter sensitivity.<sup>10</sup> Use of the hydrogen monitor data after 200 min to assess a partition fraction is therefore questionable. The most reliable end-of-test (integral) hydrogen release data for the SFD-ST experiment were obtained from metallographic assay of the test debris, yielding 220 g (+40 g, -88 g) total, of which  $172 \pm 40$  g were due to oxidation of zircaloy test components and the remainder due to fuel oxidation. Based on the metallographic data, the partitioning of  $\text{H}_2$  generation before and after the onset of zircaloy melting/fuel dissolution (2170 K) is assessed as follows.

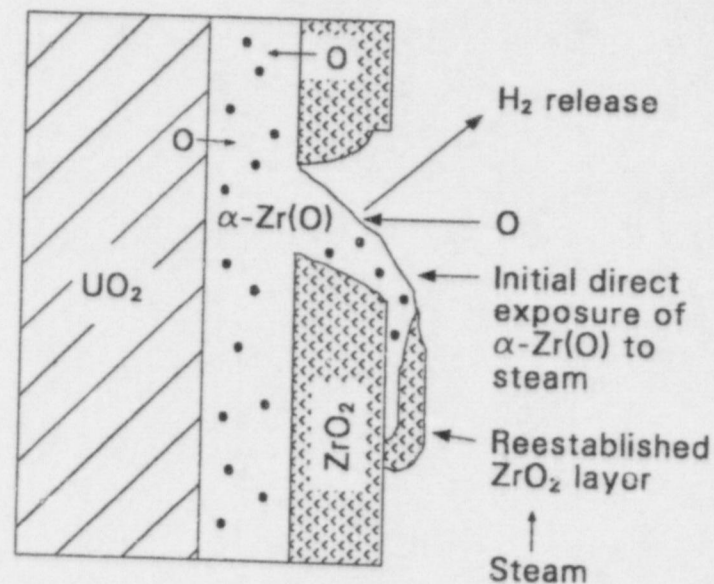
Figure 31 presents an overlay of the thermocouple measurement and the hydrogen monitor/metallography data previously given in Figure 9. Since the hydrogen monitor data are considered accurate to  $\sim 200$  min, and since the  $\alpha\text{-Zr(O)}/\text{UO}_2$  eutectic temperature of 2170 K is reached at about 204 min, the monitor hydrogen generation rate was simply extrapolated to 204 min to assess a  $\text{H}_2$  partition value. Such an extrapolation yields about 130 g  $\text{H}_2$  generation prior to 204 min (2170 K). Using a total (zircaloy plus fuel) metallographic hydrogen generation value of 220 g,








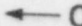
Intact rod geometry

Oxidation rate controlled by oxygen diffusion in thick  $\text{ZrO}_2$  layer



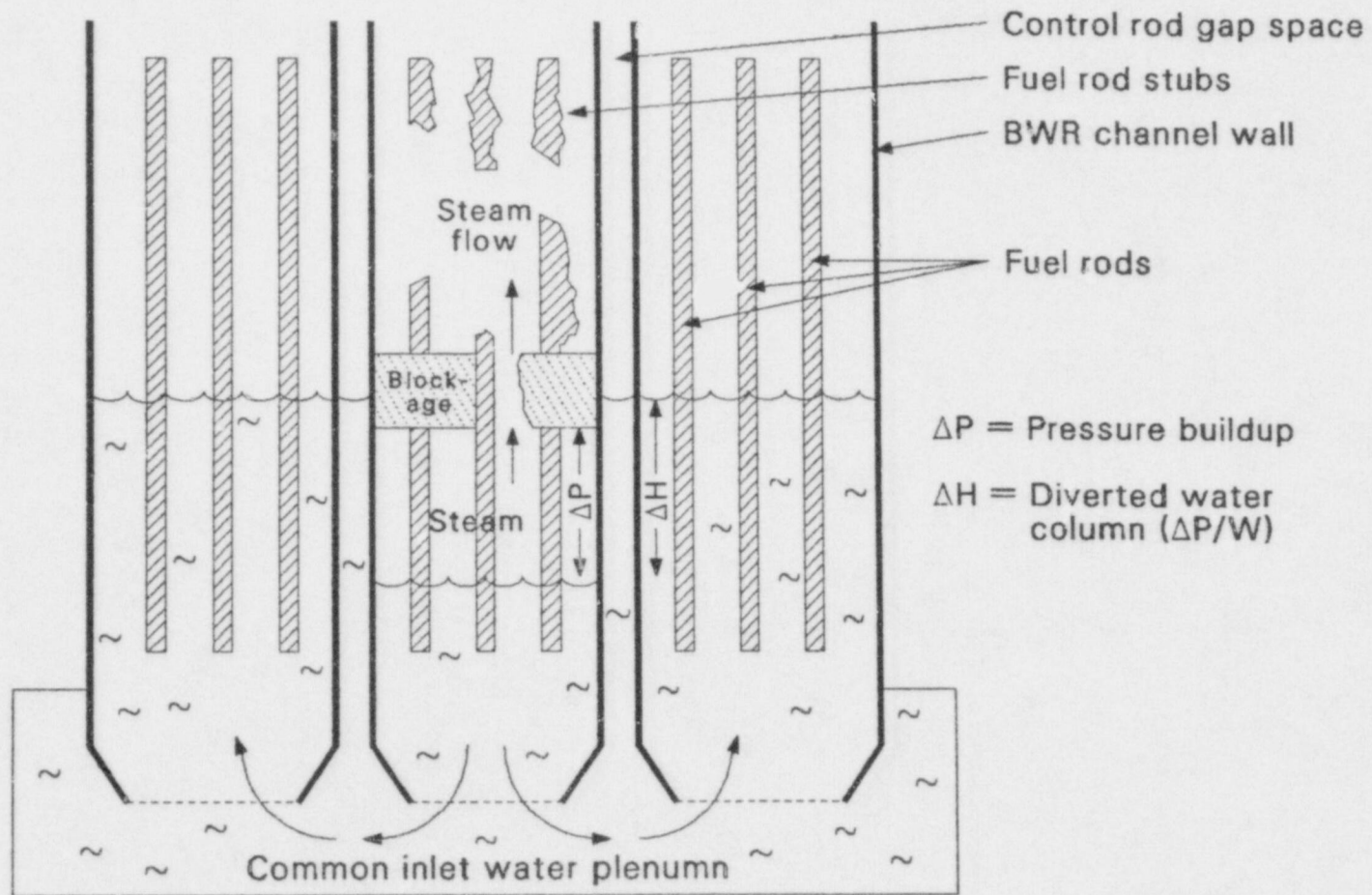
Disrupted rod geometry

Oxidation can be enhanced by direct exposure of  $\alpha\text{-Zr(O)}$  to steam

Legend:   $\text{UO}_2$    $\alpha\text{-Zr(O)}$    $\text{ZrO}_2$    $\text{O}$  Oxygen diffusion

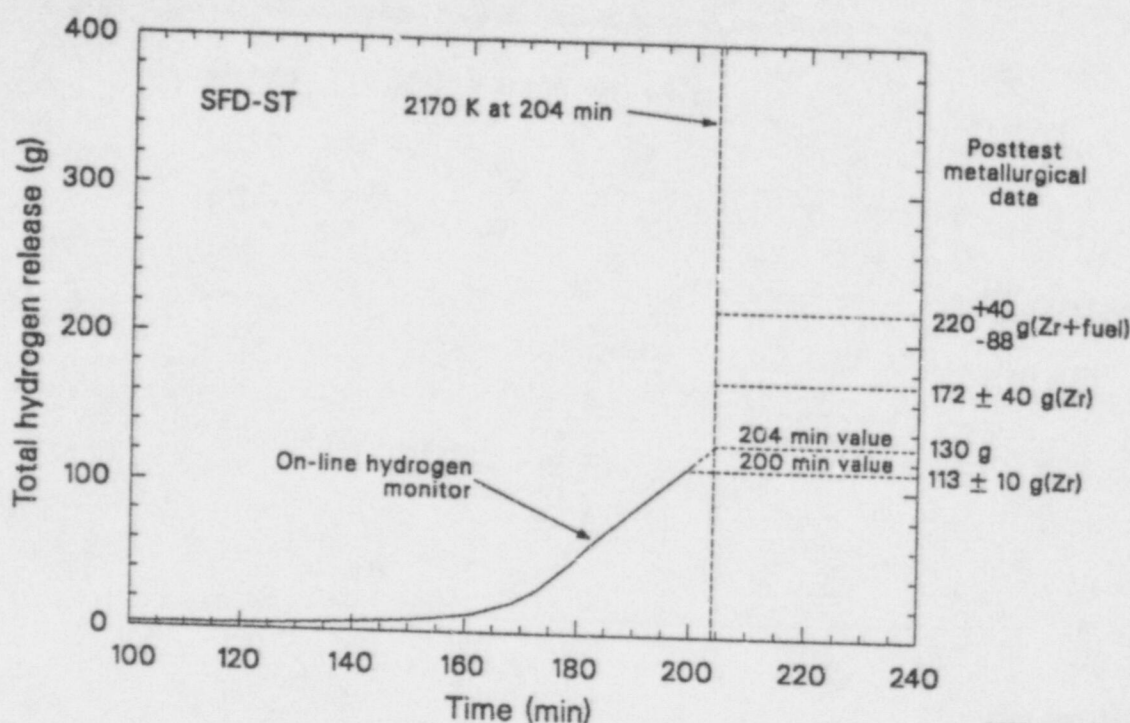
P383-KM257-02

Figure 29. Illustration of potential enhanced oxidation due to exposure of molten  $\alpha\text{-Zr(O)}$  to steam.



P383-KM257-05

Figure 30. Illustration of the IDCOR MAAP-BWR fuel assembly blockage/flow-diversion model.



P392 AWC-387-03

Figure 31. Comparison of the SFD-ST thermocouple and best-estimate  $H_2$  generation data, to assess  $H_2$  partitioning before and after the initiation of  $\alpha$ -Zr(O)/ $UO_2$  eutectic melting at 2170 K.

the partitioning fraction is about 59% before zircaloy melting and 41% after. If only zircaloy oxidation is considered (172 g based on metallographic findings), the partitioning is about 75% below 2170 K and 25% above.

Figure 32 compares the SFD 1-1 on-line measurement of the hydrogen release and cladding thermocouple data at the 0.5-m elevation. Initiation of fuel dissolution (2170 K) is indicated to occur at a test time of approximately 2008 s, with approximately 2 g of  $H_2$  production up to that point in time, based on the hydrogen monitor integral data of 73 g. Allowing that a maximum of 8 g  $H_2$  holdup in the system was generated before fuel dissolution, the partitioning of  $H_2$  is ~14% before and 86% after 2170 K. For a 30-s uncertainty in the transit time, the partitioning is ~15% before and 85% after 2170 K.

Since there remains some doubt about the validity of the second burst of hydrogen generation in the SFD 1-1 test, it is also appropriate to estimate the hydrogen partition fraction for the assumption that the second burst is due to hydrogen monitor sensitivity to moisture carryover, or some other measurement problem, and not a true indication of actual  $H_2$  generation late in the test. Using the col-

lection tank measurement of 64 g nominal total hydrogen production and the hydrogen monitor indication of approximately 10 g hydrogen generation before zirconium melting (8 g of which is due to holdup), a partitioning of about 16% before and 84% after 2170 K is estimated. Thus, the majority of  $H_2$  generation for the SFD 1-1 test is indicated to occur after the onset of fuel dissolution. As discussed previously, posttest metallographic data corroborate the on-line data, where greater than half the hydrogen generation was estimated from metallography to be due to oxidation of previously molten zircaloy-bearing debris.

It should be noted that the comparison of on-line thermocouple and integral hydrogen release data does not yield direct information on the partitioning of hydrogen generation with respect to that amount produced by oxidation of molten zircaloy and that produced from still solid zircaloy. Ideally, it would have been desirable to extract separate measurements of hydrogen released from that portion of the bundle experiencing zircaloy melting and the still solid portion of the bundle, thereby yielding separate measurements of  $H_2$  generated from molten versus solid zircaloy. However, because of the integral nature of the SFD



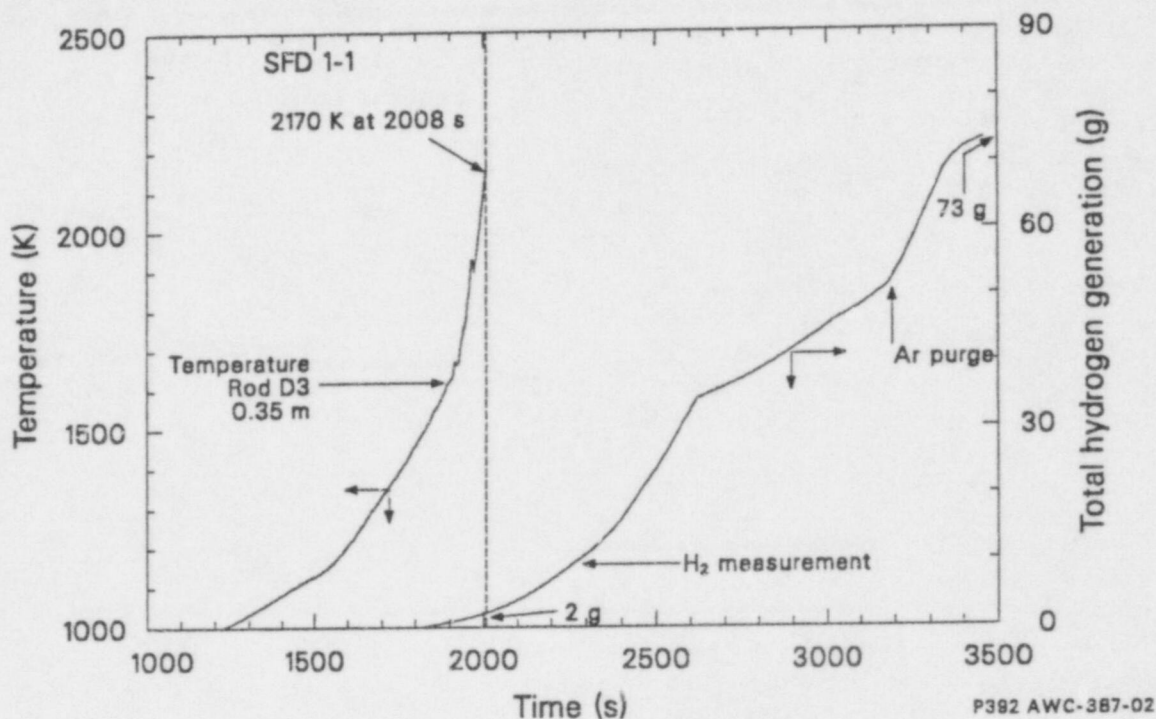


Figure 32. Comparison of the SFD 1-1 thermocouple and on-line  $H_2$  generation data, to assess  $H_2$  partitioning before and after the initiation of  $\alpha$ -Zr(O)/ $UO_2$  eutectic melting at 2170 K.

experiments and the measurement of hydrogen release from the entire bundle, this could not be accomplished. Rather, it was only possible to assess (from thermocouple data) when zircaloy melting first occurred at some location in the bundle and then partition  $H_2$  generation before and after that time. Nevertheless, such a comparison does relate to the IDCOR arguments presented in References 6, 7, and 17 for cutoff or diminished hydrogen production in BWRs upon the onset temperature (2170 K) for molten  $\alpha$ -Zr(O) dissolution of  $UO_2$ . The SFD data indicate that a significant amount of hydrogen generation occurred after 2170 K was reached at some location in the bundle.

The on-line indication of continued  $H_2$  generation after the onset of zircaloy melting is corroborated by posttest metallographic evidence of significant oxidation of previously molten zircaloy test debris. Metallographic examination of the SFD-ST bundle shows clear evidence of extensive molten zircaloy formation and oxidation of such melt. The microstructures were compared to well defined out-of-pile separate-effects microstructures to determine material composition and temperatures required to form the various types of metallic and ceramic debris found. Essentially complete oxidation of previously molten metallic debris to

a ceramic state was observed from inspection of the SFD-ST test debris. Steam-induced oxidation is considered to be the principal cause of transformation of previously molten zircaloy-bearing metallic debris to ceramic debris. Posttest metallographic inspection of the SFD 1-1 test debris also corroborates the on-line data for significant oxidation of previously molten zircaloy. Metallographic assay of the SFD 1-1 bundle indicates that in excess of 50% of the total hydrogen generated in the SFD 1-1 test can be accounted for by oxidation of previously molten zircaloy-bearing debris. Such metallographic data clearly demonstrate that oxidation of relocated material is a significant contributor to the overall  $H_2$  source term.

**Fuel Bundle Reconfiguration Effects in BWRs.** It has been proposed by IDCOR that, for canned BWR fuel assemblies, zircaloy clad melting and loss of rod geometry will lead to liquefied fuel-clad material slumping and bundle blockage.<sup>7</sup> Pressure buildup in the degraded BWR fuel assembly is then postulated to cause diversion of coolant flow to adjacent assemblies, as illustrated in Figure 30. Hydrogen production in the degraded fuel assembly is thereby substantially reduced or terminated in the IDCOR MAAP-BWR code.<sup>7</sup> The validity of this hypothesis hinges on two key

assumptions: (a) a high degree of flow area blockage so that steam pressure buildup below the blockage zone results in coolant diversion, and (b) the channel walls remaining intact so as to inhibit cross-flow communication between fuel assemblies. The SFD-ST and SFD 1-1 test data are examined here relative to these two assumptions.

**Bundle Blockage/Coolant Diversion.** Posttest examination of the SFD-ST and SFD 1-1 test bundles revealed that the maximum flow constriction occurred in the lower region of the bundle as a consequence of freezing of previously molten relocated test debris. As previously noted, posttest assay of the degree of flow area blockage yields information only with respect to the final reconfigured state of the bundle. During actual testing, a different bundle configuration existed as test debris relocated from higher to lower bundle elevations. Likewise, volume contraction on the order to 5 to 20% can be expected upon debris solidification. Thus, the posttest degree of flow area blockage is not necessarily that which existed during testing. However, the extent of flow area blockage during testing cannot be ascertained to any degree of accuracy from the limited on-line data available. The end-of-test blockage data nevertheless should give a reasonable estimate of the maximum extent of blockage, since it presents a picture of cumulative debris relocation for the entire test. Also, the effects of porosity within resolidified debris, which compensate somewhat for volume shrinkage effects, were not included in the posttest assay of residual open flow area. For these reasons, the posttest cross-sectional measurement of blockage is considered the best available estimate of flow area reduction. A nominal minimum posttest flow area of 10.2 cm<sup>2</sup> for SFD-ST and 4.9 cm<sup>2</sup> for SFD 1-1 was found, compared to the nominal flow area of 32.8 cm<sup>2</sup> for the intact bundle.

The question then centers on whether such partial blockages would result in bundle pressurization sufficient to induce significant flow diversion for true BWR geometry. Although in actuality no parallel path for flow diversion existed in the single-bundle SFD experiments, nevertheless one can assess if the degradation of test-bundle flow area would be sufficient to cause bundle pressurization and flow diversion to adjacent channels, had a parallel flow path been present.

An estimate of the differential pressure necessary to force steam flow through the blockage orifice illustrated in Figure 33 can be assessed from consideration of the compressible isentropic flow equations, where the mass flow rate per unit area for subsonic conditions can be expressed as:

$$\dot{m}_0 / A_0 = \left( \frac{P_2}{P_1} \right)^{1/\gamma} \left\{ \frac{2\gamma}{\gamma-1} \rho_1 P_1 g_c \left[ 1 - \left( \frac{P_2}{P_1} \right) \right]^{(\gamma-1)/\gamma} \right\}^{1/2} \quad (8)$$

where

$A_0$  = minimum flow area, cm<sup>2</sup>

$g_c$  = conversion factor, g cm/s<sup>2</sup> dyne

$\gamma$  = isentropic exponent =  $C_p/C_v$

$P_1$  = upstream pressure, dynes/cm<sup>2</sup>

$P_2$  = downstream pressure, dynes/cm<sup>2</sup>

$\rho_1$  = upstream density, g/cm<sup>3</sup>.

Inspection of the above equation indicates that the steam flow rate through the blockage orifice ( $A_0$ ) is governed by the upstream and downstream pressures, the downstream density, and the isentropic exponent. An evaluation of the steam flow capacity (Equation 8) is assessed in Appendix A (Table A-3) at various differential pressures, yielding the following results:

psi	$\Delta P$		$\dot{m}/A_0$ (g/cm <sup>2</sup> s)
	psi	dynes/cm <sup>2</sup>	
5		3.45 E + 05	157
2		1.38 E + 05	100
1		0.69 E + 05	70
0.1		0.69 E + 05	22

Since the posttest indication of the minimum open flow area for the degraded SFD-ST bundle is 10.2 cm<sup>2</sup>, the steam venting capacity through the blockage region at  $\Delta P = 1$  psi is estimated to be approximately 714 g/s. Since the nominal steam production rate for the SFD-ST experiment was only 16 g/s, it can be seen that a differential pressure of less than 1 psi is more than sufficient to cause continued steam venting through the partially blocked SFD-ST bundle. By equating the subsonic mass flow rate to the SFD-ST nominal steam production rate of 16 g/s, the blocked flow area ( $A_b$ ) needed to accommodate this steaming rate can be assessed. Calculations indicate that flow area

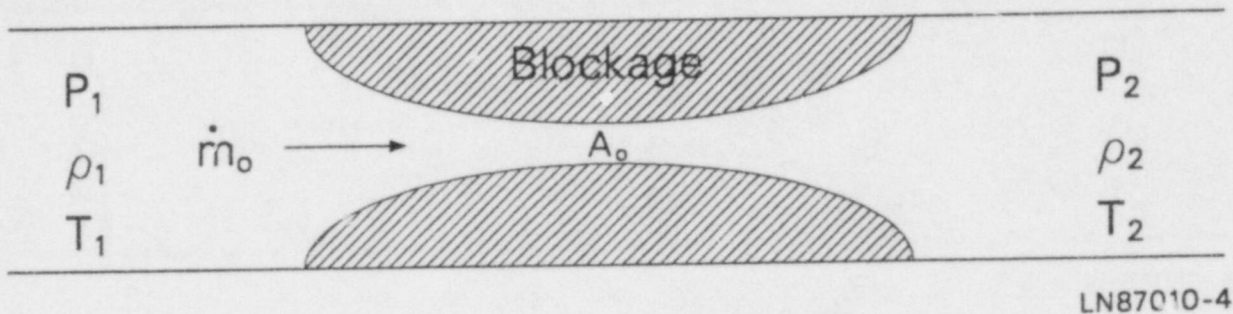


Figure 33. Illustration of isentropic compressible flow through a blockage orifice.

blockages in excess of 98% would be required to cause any appreciable pressurization ( $>1$  psi) at the inlet of the degraded SFD-ST fuel bundle.

Similar results are estimated for the SFD 1-1 test. Noting that the posttest indication of the minimum flow area for the degraded SFD 1-1 bundle was  $4.9 \text{ cm}^2$ , the steam venting capacity at  $\Delta P = 1$  psi is on the order of  $343 \text{ g/s}$ . Since the nominal steam production rate for the SFD 1-1 test was  $0.64 \text{ g/s}$ , a  $4.9\text{-cm}^2$  flow area is more than adequate to accommodate continued steam venting through the partially blocked bundle. Again, calculations indicate that flow area blockages in excess of 98% (nominal flow area =  $32.2 \text{ cm}^2$ , blockage flow area =  $0.32$  to  $0.64 \text{ cm}^2$ ) would be required to cause appreciable pressurization of the SFD 1-1 bundle. Although some uncertainty exists relative to the specification of a degraded flow area from posttest metallographic examinations, such extreme blockage conditions are not justified from the available data for either test.

Figure 34 compares the nominal flow area of the intact bundle ( $A_i = 32.8 \text{ cm}^2$ ), the posttest flow areas in the maximum blockage region of the degraded SFD-ST and SFD 1-1 fuel bundles, and the flow area of the effluent line used to vent steam from the bundle to the effluent collection and monitoring system. Since the inside diameter of the steamline is  $0.643 \text{ cm}$ , its flow area ( $0.324 \text{ cm}^2$ ) is small compared to that of the bundle itself. Clearly the smaller flow area of the off-gassing steamline (or flow control valve) would have governed choked flow conditions, rather than the larger flow area of the partial blockage regions of the degraded SFD-ST and SFD 1-1 test bundles. However, no such choking occurred, as indicated by either the SFD-ST or SFD 1-1 pressure data.

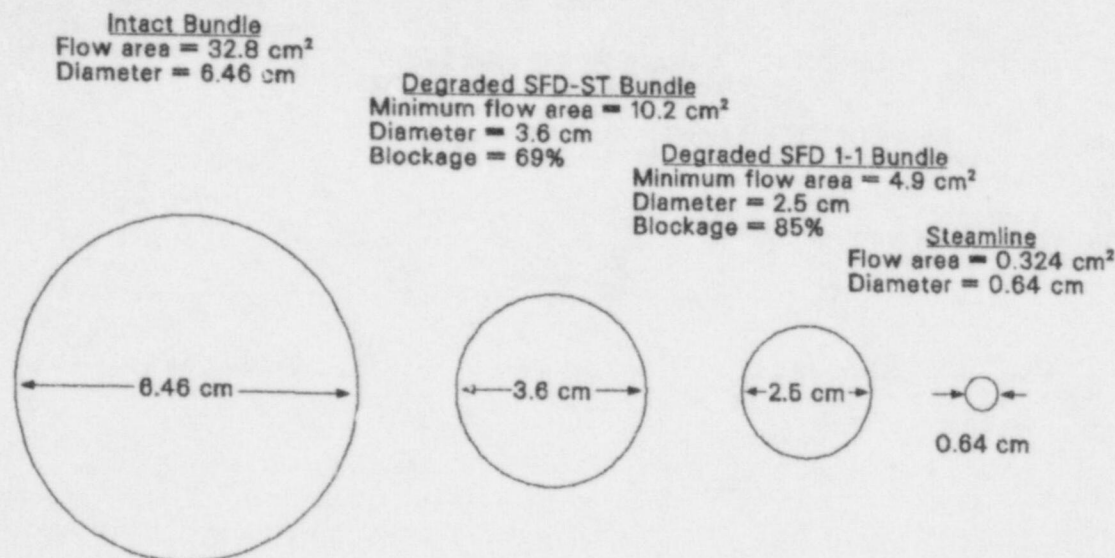
Recently it has been argued<sup>36</sup> that the absence of a parallel flow path in the PBF-SFD tests prevented stable blockage formation. By contrast, for whole-core BWR geometry it is postulated that downward melt

debris relocation will result in debris plugging of the entire fuel assembly flow area, with subsequent surface or crust solidification, which will effectively seal the bundle from further oxidation. In the analysis, it is assumed that a BWR fuel assembly is first completely blocked. Pressure buildup below the refrozen blockage crust is then calculated and compared with the growth rate for crust buildup. Since a BWR core incorporates parallel flow path geometry, pressure relief below the blockage crust is postulated to occur by diverting water to adjacent fuel assemblies, so that stable blockage is predicted to occur. Due to the absence of a parallel flow path for pressure relief in the PBF-SFD tests, it is argued that crust breakup will occur which effectively excludes permanent blockage formation.

The validity of these arguments hinges primarily on the assumed initial condition that the coolant channel is first blocked. If this were not the case, then a flow path would exist for continued steam flow through the bundle and attendant continued oxidation above the blockage region. The primary question centers on whether or not downward melt debris relocation will spread across the entire fuel assembly and completely block the flow area, or whether the debris will relocate and freeze in an asymmetrical incoherent manner, allowing for flow channels and continued steam venting through the degraded bundle.

A first-principles assessment of the geometric conditions for transient melt relocation and solidification in bundle geometry is difficult to predict, due in part to the coupled hydrodynamic and solidification heat transfer aspects of the problem, as well as the difficulty of defining a generic set of boundary conditions. Likewise, non-uniform asymmetric conditions which complicate the analysis may occur. These difficulties aside, an order-of-magnitude assessment of the potential to form flow channels in the melt can be made by consideration of the hydrodynamic aspect of





P340 AWC-187-19

Figure 34. Comparison of flow area degradation in the SFD-ST and SFD 1-1 test bundles.

downward flowing liquid zircaloy exposed to upward steam flow.

Figure 35 illustrates the problem of counter-current flow in which a film of zircaloy melt debris is subjected to gravity-induced drainage and an upward directed shear stress caused by steam flow. As the steaming rate increases, liquid waves appear at the film interface. Eventually the flow becomes chaotic, and liquid droplets will break off the surface. This condition is known as flooding. For counter-current liquid-gas flow, the flooding velocity ( $V_f$ ) can be expressed as:<sup>37</sup>

$$V_f = [g D_e (\rho_l - \rho_g)/\rho_g]^{1/2} \sim [g D_e \rho_l/\rho_g]^{1/2} \quad (9)$$

where

$D_e$  = the equivalent channel diameter, cm

$\rho_g$  = the gas density, g/cm<sup>3</sup>

$\rho_l$  = the liquid density, g/cm<sup>3</sup>

$g$  = the gravitation constant, 980 cm/s<sup>2</sup>.

To assess the diameter of the flow channel at which the onset of flooding will occur in terms of the gas

flow conditions, the continuity equation is applied, i.e.,

$$\dot{m} = \rho_g A_f V_f = \pi P_2 V_f D_g^2/4 \quad (10)$$

where  $\dot{m}$  is the mass flow rate,  $A_f$  is the flow area, and  $V_f$  is velocity. Combining these equations yields the following expression for the channel diameter at which liquid film breakup will occur

$$D_c^5 = \frac{16 \dot{m}^2}{(\pi)^2 \rho_l \rho_g g} \quad (11)$$

Table A-4 of Appendix A presents results for the SFD-ST and SFD 1-1 test conditions. For the SFD-ST nominal steam flow conditions of 16 g/s, an equivalent flow diameter ( $D_e$ ) of less than 1.126 cm is calculated to result in flooding-induced breakup of the melt debris, where the associated flow area ( $A_f$ ) is  $\sim 0.996$  cm<sup>2</sup> and the flooding velocity ( $V_f$ ) is 446 cm/s. For comparative purposes, the nominal open flow area of the undegraded bundle is 32.8 cm<sup>2</sup>, while the sonic velocity of steam at a temperature of 1500 K is approximately 800 m/s. For the SFD-ST flow rate of 16 g/s, the onset of flooding and attendant breakup of a draining liquid film geometry is thus predicted at a factor of 30 reduction in flow area, with the attendant

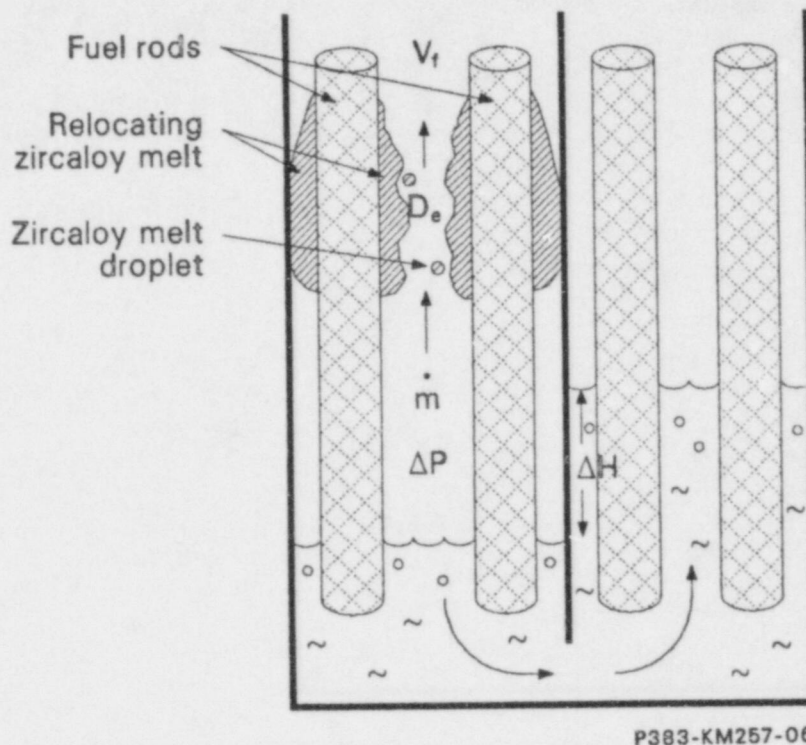


Figure 35. Illustration of flooding-induced breakup of relocating melt debris.

flooding velocity well below sonic conditions. Similar calculational results are obtained for the SFD 1-1 flow rate of 0.64 g/s, where  $D_e = 0.31$  cm,  $A_f = 0.0758$  cm<sup>2</sup>, and  $V_f = 235$  cm/s are estimated.

The question then arises as to whether flooding is first induced, which may inhibit complete sealoff of the flow area, or whether the approach to blockage results in pressure buildup below the constriction sufficient to divert coolant to adjacent channels, thereby diminishing steam flow in the degraded channel so that complete sealoff of the blockage region occurs. To assess this question, an estimate is made of the differential pressure associated with the equivalent channel diameter for flooding, where the equations of compressible isentropic flow (and a two-phase pressure drop correction) are employed. Using the iterative procedure outlined in Table A-5 of Appendix A, a single-phase  $\Delta P$  of 0.35 kPa (0.05 psi) is estimated at the SFD-ST nominal steam flow rate of 16 g/s and  $D_e = 1.125$  cm ( $A_f = 0.994$  cm<sup>2</sup>). Noting that droplet entrainment occurs at the flooding condition, causing an approximate order-of-magnitude increase in the pressure gradient<sup>37</sup> due to the two-phase nature of liquid-droplet/steam flow, a two-phase  $\Delta P$  of 3.45 kPa (0.5 psi) is estimated at the flooding condition. At a coolant specific weight

( $w$ ) of 0.74 g/cm<sup>3</sup> (46 lb<sub>f</sub>/ft<sup>3</sup>) [saturated liquid at 6.9 mPa (1000 psi)], this  $\Delta P$  corresponds to the following flow diversion height ( $\Delta H$ ) had a parallel flow path existed:

$$\Delta H = \Delta P / w = 48 \text{ cm.} \quad (12)$$

For the SFD 1-1 nominal flow condition of 0.64 g/s and  $D_e = 0.31$  cm, a single-phase pressure differential of 0.1 kPa (0.015 psi) is estimated, with an associated two-phase  $\Delta P$  of 1.0 kPa (0.15 psi) and a  $\Delta H$  of about 15 cm (6 in). Such limited flow diversion would appear to be insufficient to terminate boiloff in a full-length [3.66-m (12-ft)] bundle. Thus, it can be argued that flooding-induced breakup of relocating melt debris may tend to inhibit complete flow area blockage before boiloff is terminated by coolant flow diversion.

It should be noted that such flooding arguments are used here for illustrative purposes only and have been applied to an idealized configuration of a liquid film subject to uniform drainage across the entire cross-sectional area of the bundle. In actuality, the debris is probably more accurately described as a slush, composed of  $\alpha$ -Zr(O) melt and partially dissolved solid ZrO<sub>2</sub> and UO<sub>2</sub> ceramic debris. In addition, preliminary data from the NRU full-length [3.66-m (12-ft)] bundle



experiments<sup>38</sup> indicate asymmetric melt drainage conditions, having the cooler side of the bundle open to steam flow, with melt drainage and asymmetric refreezing (on still-intact fuel rods) on the hotter side of the bundle. Such NRU data may therefore indicate length effects on debris relocation which are not evident in the shorter [0.9-m (3 ft)] PBF-SFD tests. Length effects are probably best addressed by the NRU data, which however are preliminary at this time.

It is also noted that in most severe accident analysis codes (e.g., MAAP and SCDAP), only an axial temperature profile within the bundle is considered, so that at a particular elevation potential rod-to-rod azimuthal temperature variations in the bundle are neglected. This assumption of radial temperature uniformity results in a prediction of coherent zircaloy melting within an axial node and the attendant assumption (in MAAP-BWR) of coherent melt relocation, refreezing, and total cross-sectional flow blockage. However, temperature measurements in the steam-starved SFD 1-1 bundle indicate azimuthal temperature variations, which appear to be exacerbated by the autocatalytic nature of the zircaloy cladding oxidation process.

Figure 36 presents a comparison of the SFD 1-1 rod cladding thermocouple data at various rod positions (see Figure 1) at the 0.35-, 0.50-, and 0.70-m elevations. The data indicate that at the same axial elevation/time period, an azimuthal bundle variation in rod temperature of several hundred degrees existed, which appears to escalate to a higher temperature difference. This escalation in asymmetric bundle heating can be attributed to the autocatalytic nature of zircaloy oxidation, which can be visualized as follows. One side of the bundle is initially at a temperature higher than the other side. The bundle is steam-starved, so most of the steam is consumed by the higher-temperature zircaloy cladding. Oxidation drives the hotter zircaloy to higher temperatures, which consumes a greater portion of the steam, driving local temperatures higher, and so on. The autocatalytic nature of zircaloy oxidation may therefore lead to asymmetric bundle heatup, oxidation, and melt formation, which are not predictable with one-dimensional codes.

Arguments have also been made that a true test for simulation of BWR core geometry requires a bypass flow area that is large compared to that of the test bundle, so as to minimize the hydraulic resistance for flow diversion. Consider the two situations illustrated in Figure 37, where both Case 1 and Case 2 have the same bundle cross-sectional

flow area but markedly different bypass areas. Case 1 is typical of a test where the bypass flow area is small compared to that of the bundle, while Case 2 has a relatively large bypass flow area. Thus, the driving pressure ( $\Delta P$ ) necessary to divert an equivalent volume of water ( $\Delta V_1 = \Delta V_2$ ) from the blocked test bundle to the bypass is larger in Case 1 than for Case 2, since the diverted water column height or head is larger in Case 1 ( $\Delta H_1$ ) than Case 2 ( $\Delta H_2$ ). It can therefore be argued that the higher  $\Delta P$  required for Case 1 tends to prevent complete flow area blockage. However, for true BWR geometry a smaller  $\Delta P$  would drive coolant from the degraded bundle to the large bypass area so that blockage is more likely for Case 2. Although such arguments have merit, the fact remains that for either situation a sufficient height of water ( $\Delta H$ ) must be diverted from the degraded bundle such as to terminate boiloff. A coolant diversion height from the bundle of  $\Delta H = 0.3$  m (1 ft) requires a minimum driving pressure (assuming infinite bypass area) of about 2.07 kPa (0.3 psi). As indicated previously, flow blockage in excess of 98% constriction would be necessary to induce such pressurization.

**BWR Channel Box Survival.** The IDCOR BWR coolant flow diversion arguments illustrated in Figure 30 also require that the BWR channel wall remain intact during core degradation. However, recent analysis<sup>39</sup> indicates that oxidation and heatup of a typical BWR zircaloy channel box can be expected to closely follow that of the cladding and that melt failure of the cladding [thickness  $\sim 0.9$  mm ( $\sim 0.037$  in.)] and channel wall [thickness 2.0 mm (0.08 to 0.1 in.)] occurs at about the same time during accident progression.

Evidence for BWR zircaloy channel box oxidation and failure is also noted from the PBF-SFD tests. As shown in Figure 1, the PBF-SFD test bundles were shrouded in a 0.76-mm ( $\sim 0.03$ -in.) thick zircaloy metal liner that was instrumented with thermocouples. A comparison of the shroud liner and radially averaged fuel cladding temperatures for SFD-ST is shown in Figure 38. As indicated, the zircaloy liner temperature followed closely that of the fuel rods, experiencing similar oxidation driven heatup and behavior. Similar oxidation-driven heatup of the SFD 1-1 liner is indicated in Figure 39.

Posttest metallographic examinations of the SFD-ST and SFD 1-1 liner also showed clear evidence of failure due to melting and extensive oxidation of the liner material. Metallographic  $ZrO_2$  and  $\alpha$ -Zr(O) thickness measurements on the SFD-ST



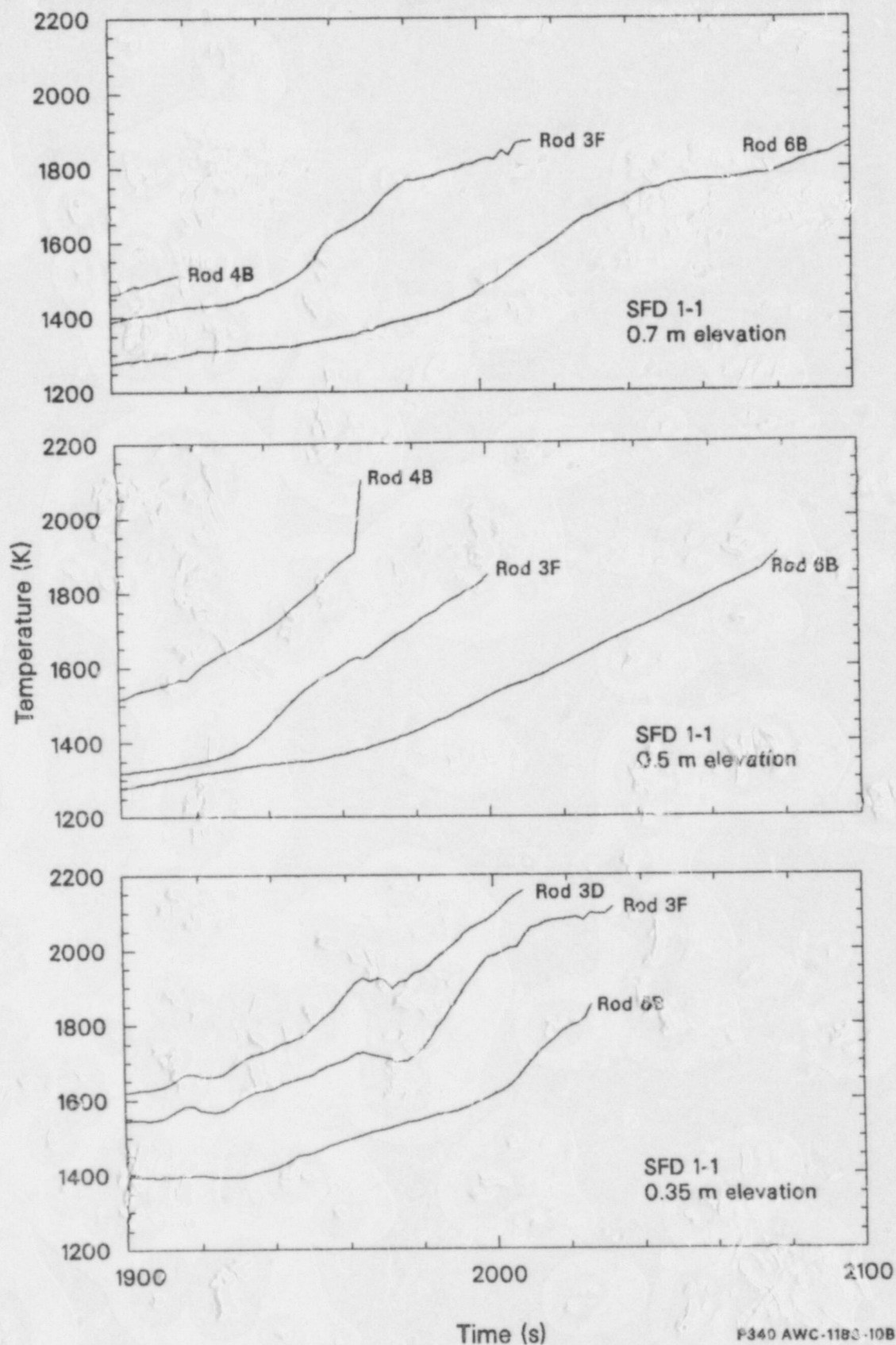
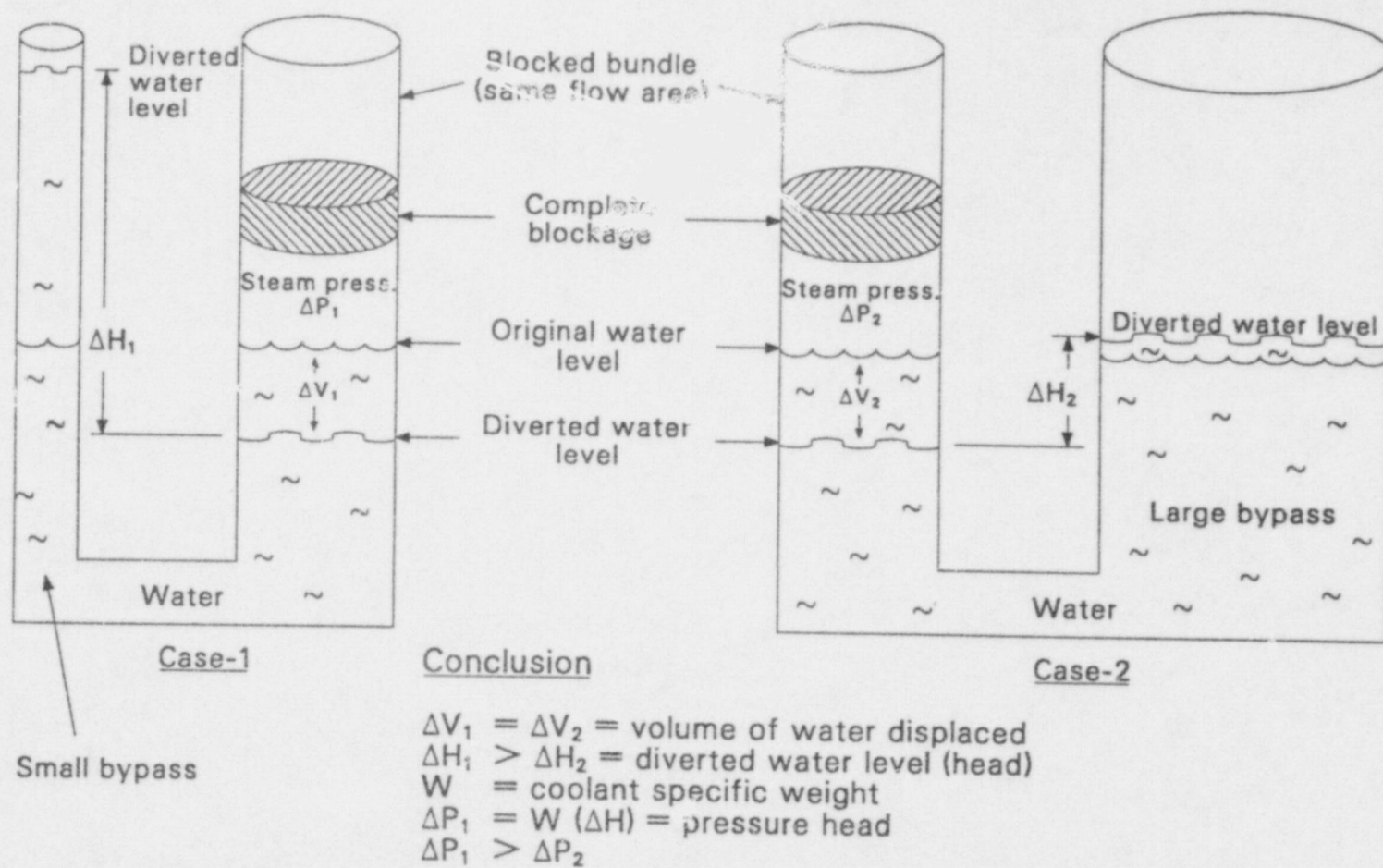


Figure 36. Illustration of asymmetric rod temperature conditions in the SFD 1-1 test bundle.



P383-KM257-07

Figure 37. Illustration of bypass flow area effects on bundle pressurization.

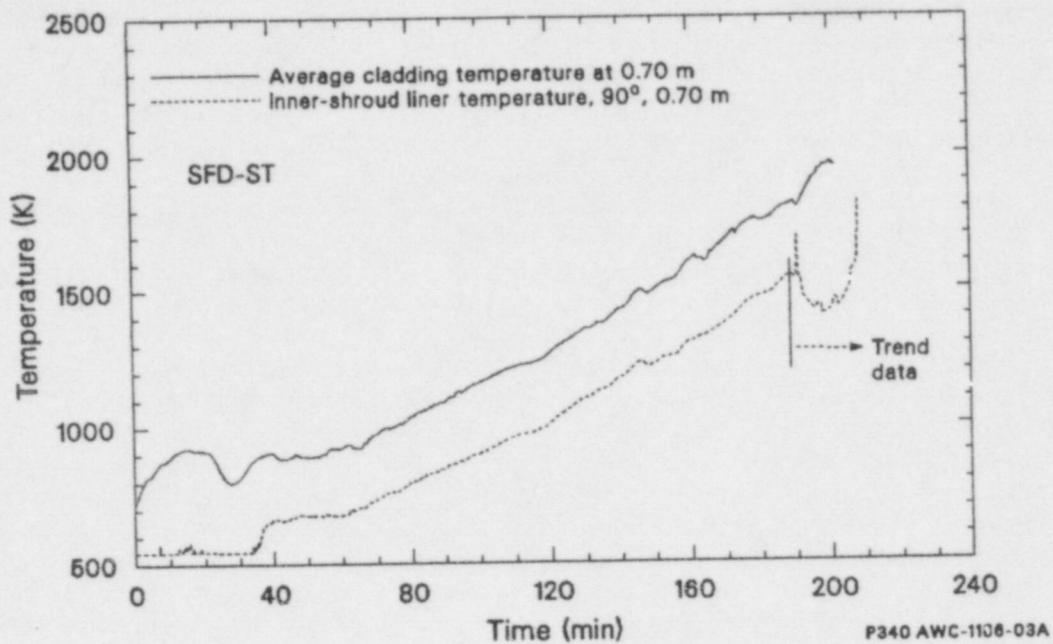


Figure 38. Comparison of SFD-ST shroud liner and radially averaged fuel cladding temperatures at the 0.7-m elevation.

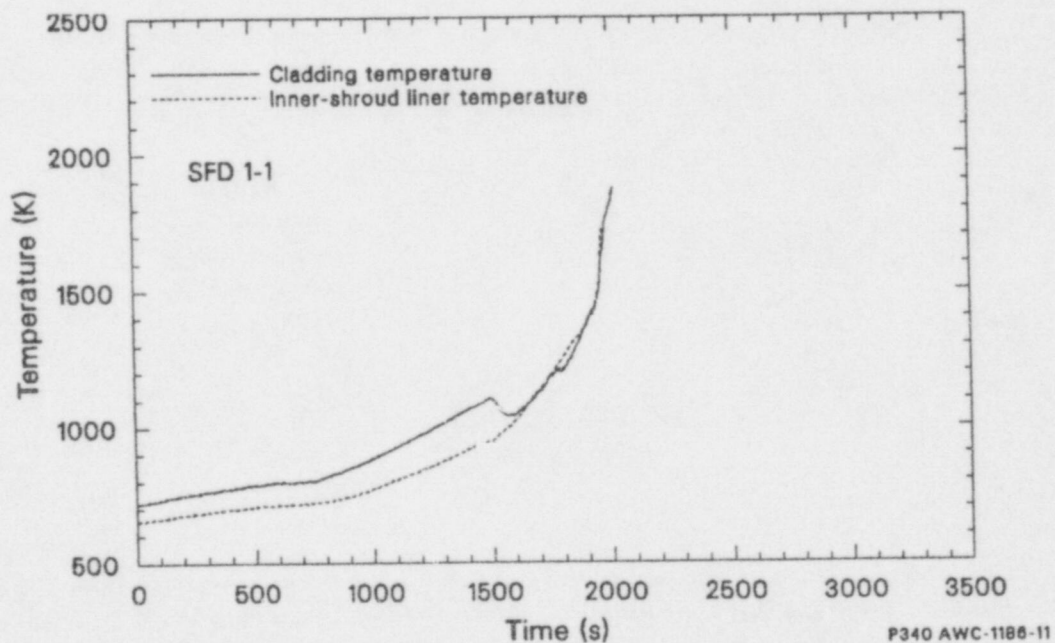


Figure 39. Comparison of SFD 1-1 shroud liner and cladding temperatures at the 0.5-m elevation.



inner liner indicate that approximately 39 g of hydrogen were generated from liner oxidation, compared to a maximum possible of 73 g for complete liner oxidation to  $\text{ZrO}_2$  (see Table 4). The highest degree of liner oxidation occurred above the maximum blockage elevation (0.17 m) as determined from oxide layer thickness measurements (see Ref. 10, Table 5). Extensive liner failure was also noted at essentially all axial locations along the axial length of the bundle.

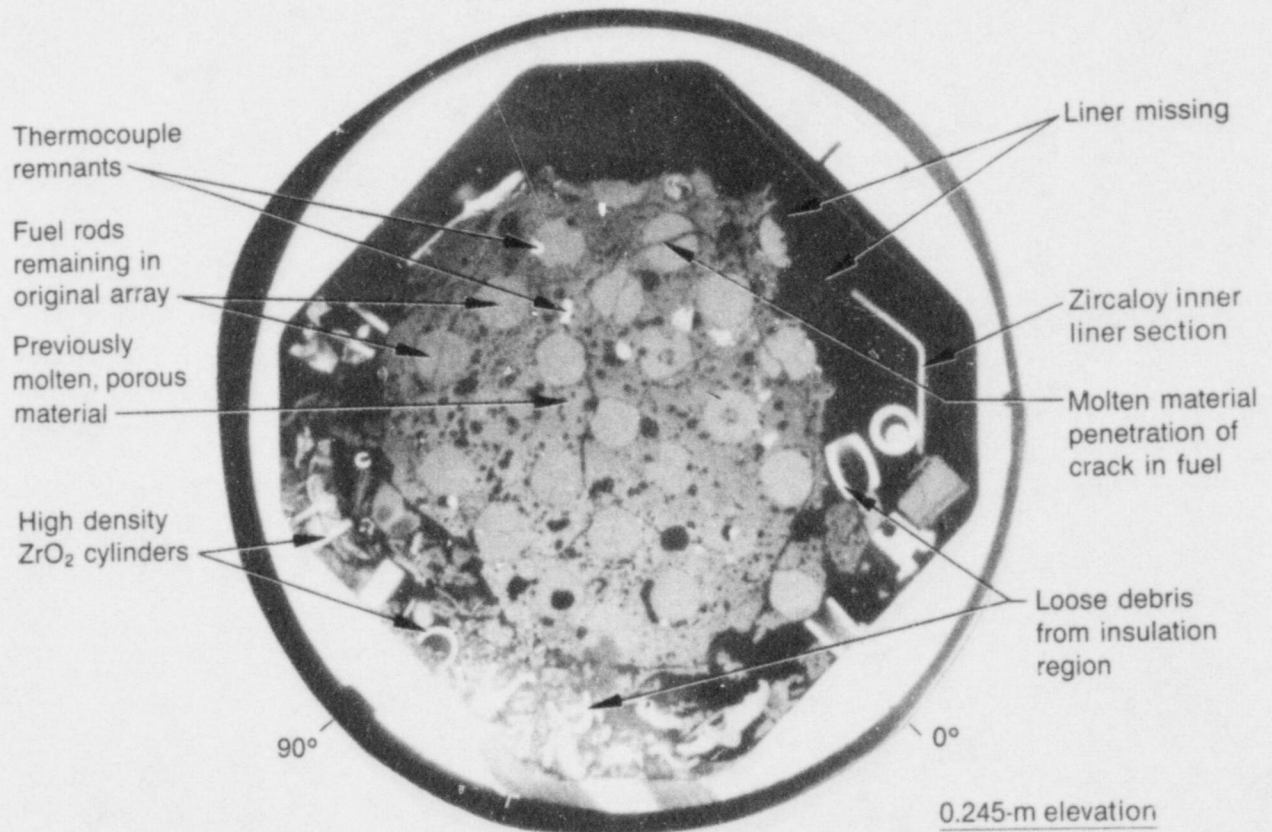
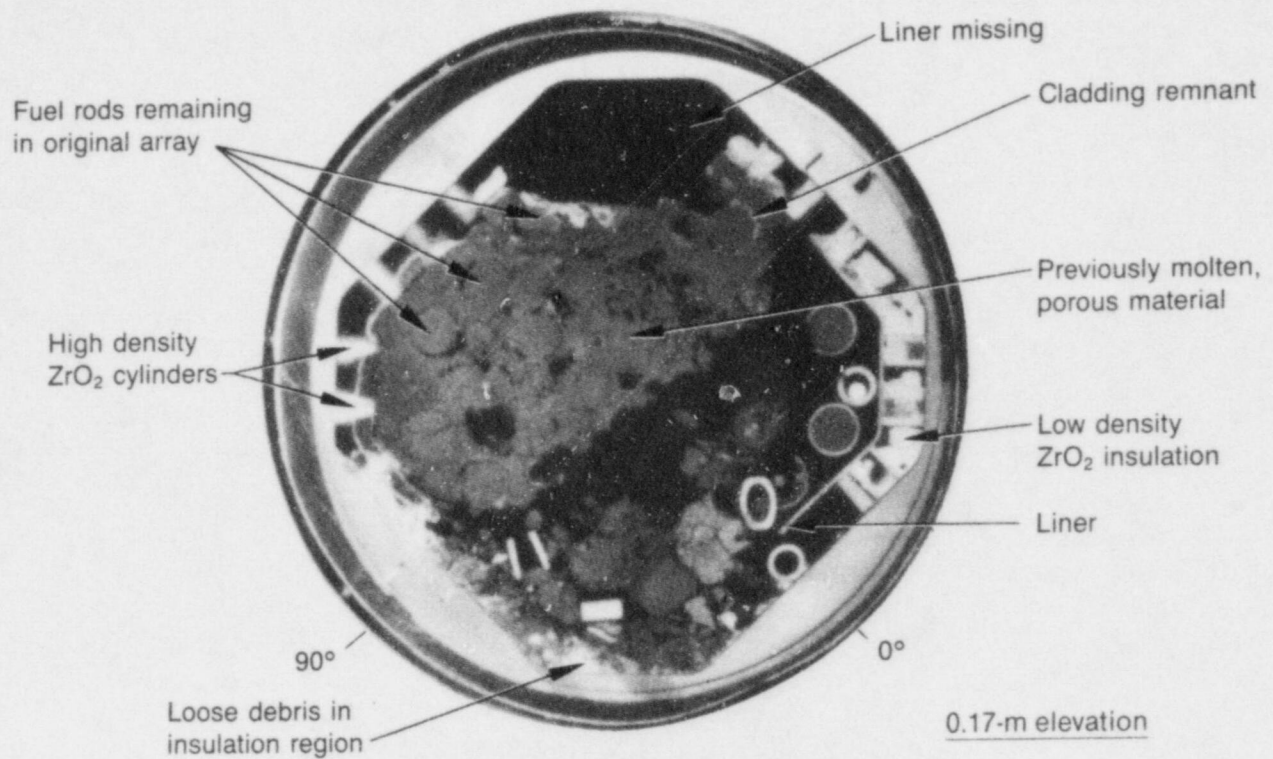
Figure 40 presents metallographic cross sections of the SFD-ST bundle at two axial elevations, indicating extensive liner failure at both sample locations. Posttest metallographic examination of the SFD 1-1 bundle at the elevation of maximum blockage (0.066 m) likewise showed extensive interaction between previously molten test debris and the zircaloy liner.<sup>11</sup> At the 0.066-m cross section, the liner adjacent to fuel rods was essentially completely oxidized. Figure 41 indicates that dissolution of the oxidized liner occurred at the inner surface by attack of previously molten metallic melt. At several circumferential orientations at the 0.066-m elevation, the liner material showed melt failure or was missing (see Figure 22). Oxide layer thickness measurements over the entire bundle length indicated that a total of 12.3 g of hydrogen was generated from liner oxidation, out of a possible maximum of 73 g (see Table 6). Failure of the SFD 1-1 liner was noted at essentially all axial elevations.

The implications of the SFD-ST and SFD 1-1 test data are that survival of a BWR zircaloy channel box cannot be assured, which would largely negate the assumption of segregated BWR assembly geometry upon which the IDCOR-BWR blockage/flow diversion arguments hinge. As illustrated in Figure 42, failure of a BWR channel wall would tend to reestablish flow through a blocked bundle and allow for continued oxidation of rod stubs above the blockage region. Although differences in test conditions and accident sequences can lead to different boiloff and cladding-versus-channel-box oxidation behavior, the fact that the thickness of a typical BWR zircaloy channel box (80 to 100 mils) is only about two to three times that of

the fuel rod cladding indicates that a BWR channel wall may indeed experience failure under severe accident conditions, as the SFD data indicate.

It should be also be noted that recent experimental studies<sup>40</sup> have been performed to investigate BWR control rod behavior for severe accident coolant-boiloff conditions. Results indicate early failure of the stainless-steel clad  $\text{B}_4\text{C}$  cruciform control rods due to B-Fe eutectic melting at about 1520 K (1250°C). The resultant iron-rich melt was also found to dissolve the zircaloy channel box by Fe-Zr eutectic melt formation at about 1570 K (1300°C), providing yet another means for channel box failure.

In summary, the analysis of the SFD-ST and SFD 1-1 test data with respect to the effects of loss of rod geometry on potential flow diversion for BWR conditions indicates that essentially complete flow area blockage (>98%) would be required to cause choked flow and bundle pressurization. Such extreme blockage conditions are not supported by the SFD bundle examination results. Analysis also indicates that counter-current steam flow may tend to cause hydrodynamic breakup of relocating molten zircaloy, which may prevent complete flow area blockage of the fuel assembly or induce asymmetric melt drainage conditions. Likewise, asymmetric bundle heatup conditions were noted, which may induce incoherency of zircaloy melting and debris relocation. Evidence was also presented indicating that oxidation-driven heatup of a BWR assembly channel box can be expected to follow closely that of the fuel rod cladding so that channel box survival cannot be assured. These findings therefore call into question the IDCOR-BWR contention that cladding melting and attendant loss of rod geometry result "a priori" in blocked BWR fuel assemblies with intact channel box walls, with coolant flow diversion from the degraded assembly and termination of hydrogen production. Further discussion of the implications of the SFD-ST and SFD 1-1 test data on severe accident hydrogen generation source term issues is given in Reference 41.



7-6525

Figure 40. Metallographic cross sections of the SFD-ST bundle at the 0.17- and 0.245-m elevations indicating liner failure above and at the maximum blockage location.

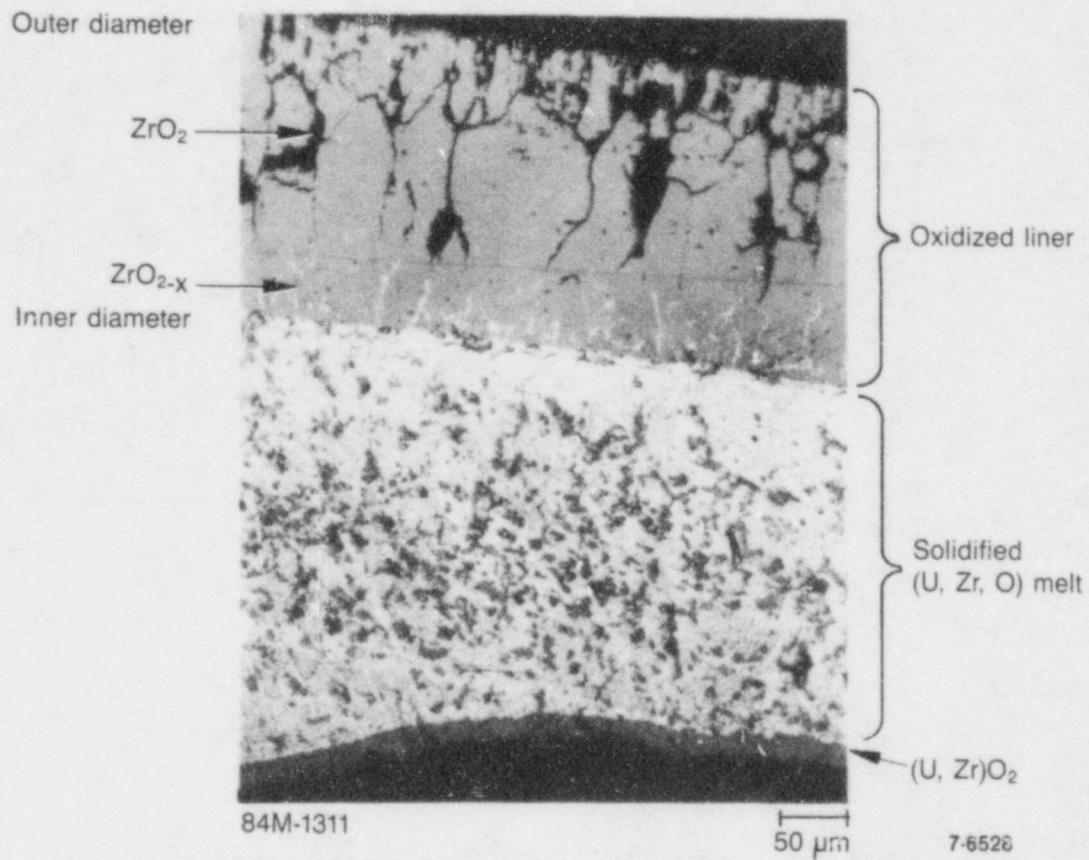
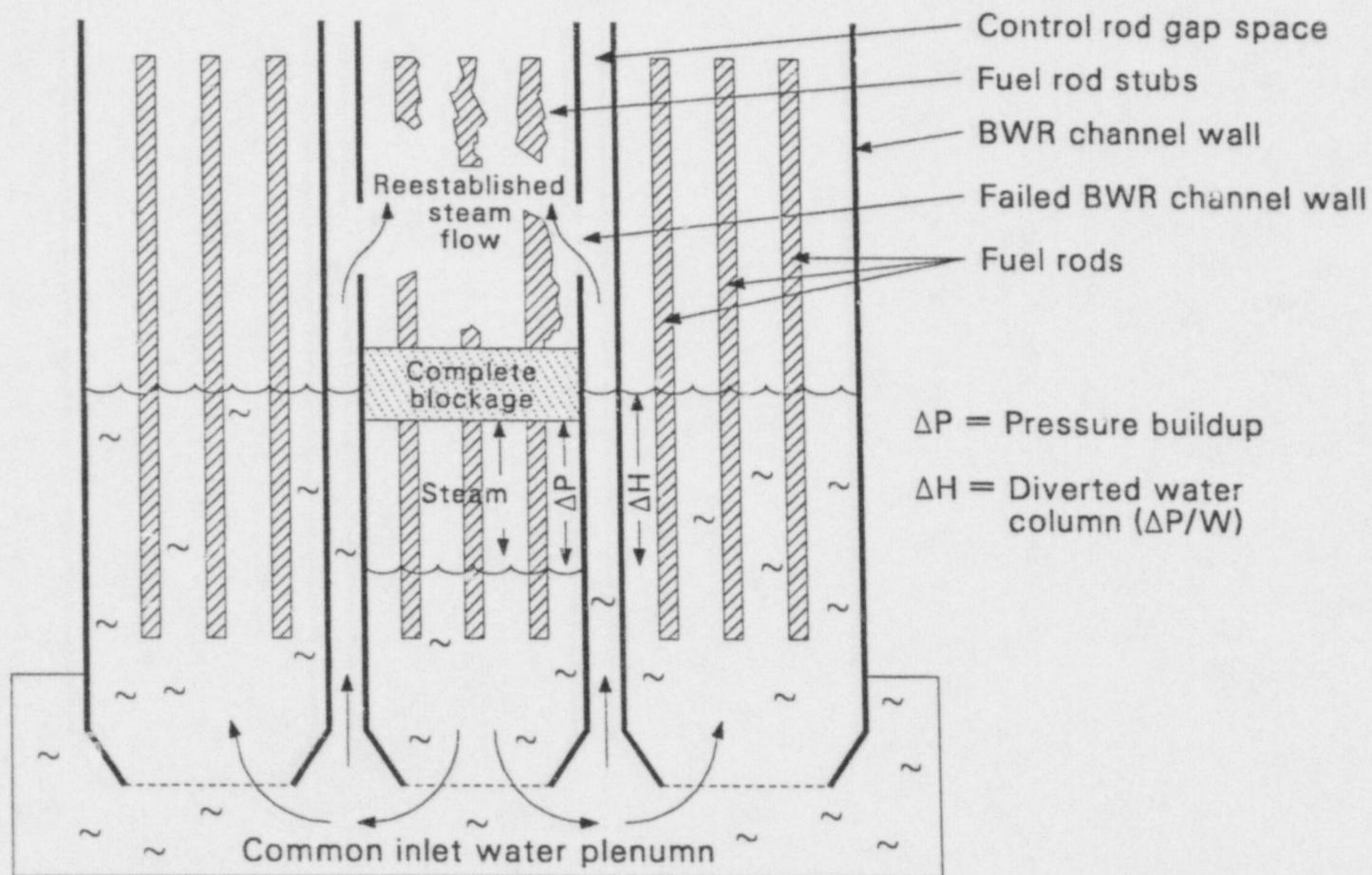


Figure 41. Dissolution of the oxidized SFD 1-1 liner on the inner surface by a metallic (U,Zr,O) melt at the 0.066-m elevation.





P383-KM257-04

Figure 42. Illustration of reestablished steam flow through a failed channel wall in a degraded/blocked BWR fuel assembly.

## SUMMARY AND CONCLUSIONS

The overall objective of the PBF-SFD test series was to contribute to the understanding of LWR severe accident behavior, with particular emphasis on fuel degradation behavior, hydrogen generation, and fission product release. In this report, the SFD-ST and SFD 1-1 data relative to zircaloy oxidation and hydrogen generation were presented, and implications to the understanding of in-vessel processes affecting hydrogen generation under severe accident conditions were assessed. The principal findings can be summarized as follows.

During the intact-rod geometry phase of the test, zircaloy oxidation is reasonably well understood. Within the uncertainties of test boundary conditions (e.g., coolant liquid level, bundle nuclear power, shroud heat losses), cladding temperatures as predicted by SCDAP using parabolic oxidation kinetics were in reasonable agreement with the SFD-ST and SFD 1-1 thermocouple data. The cladding thermocouples were sheathed in zircaloy and could accurately measure temperatures only up to about 2200 K before they failed. At about the same temperature,  $\alpha$ -Zr(O) melting and dissolution attack of  $\text{UO}_2$  (2170 K) will commence, so that oxidation behavior of zircaloy melt must be deduced from less-certain on-line hydrogen collection and posttest metallographic data. Measurement uncertainties and loss of rod geometry complicate the interpretation of test behavior after temperatures of  $\sim 2170$  K are reached. Nevertheless, the on-line hydrogen generation and posttest metallographic data indicate some common observations for both the SFD-ST and SFD 1-1 tests.

In both experiments, posttest metallographic examinations revealed that previously molten metallic debris oxidized by reacting with steam during and following melt debris relocation. A comparison of the on-line hydrogen release and clad thermocouple data also indicate continued and significant hydrogen generation after cladding temperatures in excess of 2170 K had been achieved.

Test specific data are summarized in Table 11. The large difference in the total amount of hydrogen generated for the SFD-ST and SFD 1-1 tests is attributed to differences in steam supply conditions. For the steam-rich SFD-ST environment, significantly more hydrogen was generated as would be expected. Metallographic data indicated extensive evidence of oxidation of previously molten, zircaloy-bearing debris. Fuel oxidation was also evident from metallographic examination of the SFD-ST fuel debris. No

fuel oxidation was observed, however, for the steam-starved SFD 1-1 test.

With respect to in-vessel processes affecting the hydrogen source term for severe accident conditions, the SFD-ST and SFD 1-1 data indicate the following trends. Concerning the issue of oxidation behavior after the onset of zircaloy melting and fuel dissolution (2170 K), posttest metallographic data indicate significant oxidation of previously molten zircaloy in both the SFD-ST and SFD 1-1 tests. Likewise, a comparison of on-line hydrogen release and cladding thermocouple data indicates significant hydrogen production after the temperature for Zr/ $\text{UO}_2$  eutectic melting (2170 K) was achieved. For Test SFD-ST, 25-40% of the total hydrogen produced is estimated to have occurred after a temperature of 2170 K was reached in the test bundle. For the SFD 1-1 test, approximately 85% of the total hydrogen generated is indicated to have occurred after onset of eutectic melting. Thus, the on-line hydrogen release and posttest metallographic data are consistent and indicate continued oxidation of molten zircaloy bearing test debris. Arguments for cutoff or significantly diminished hydrogen generation upon zircaloy melting and fuel dissolution are not supported by the SFD-ST and SFD 1-1 test data.

The difference in partitioning of  $\text{H}_2$  generation between the two tests (60-75% before 2170 K for SFD-ST and 15% before 2170 K for SFD 1-1) is largely related to steam supply conditions. For the steam-rich SFD-ST experiment, oxidation over the entire bundle occurred during heatup. For the steam-starved SFD 1-1 test, oxidation was limited to a local region of the bundle during initial heatup, leaving a large portion of zircaloy relatively unoxidized after 2170 K was reached, and thus available for later oxidation. Since the SFD 1-1 steam supply conditions are more typical of what would be expected for decay-heat-induced core boiloff conditions, the hydrogen partitioning for SFD 1-1 is considered more typical of what can be expected for small-break-LOCA-initiated severe accidents.

With respect to melt debris relocation/blockage/coolant conversion effects in BWRs, analysis of the SFD-ST and SFD 1-1 test data indicates that essentially complete flow area blockage (>98%) would be required to cause choked flow and bundle pressurization. Such extreme blockage conditions are not supported by the on-line data or posttest bundle examinations. Analysis also indicates that

**Table 11. Summary of zircaloy oxidation and hydrogen generation behavior noted in the PBF SFD-ST and SFD 1-1 experiments**

Parameters	Source of Data or Analysis	SFD-ST	SFD 1-1
Test environment	-Nominal makeup flow -Nominal heating rate -Measured oxidation-driven heat rate above 1700 K	~16 g/s (steam rich) ~0.13 K/s ~3 K/s	~0.64 g/s (steam starved) ~0.30 to 0.9 K/s > 6.8 K/s
Hydrogen generation	-Hydrogen monitor data -Collection tank data -Metallographic data (total) Zircaloy cladding Other bundle zircaloy UO <sub>2</sub>	375 ± 140 g Not available 220 g 112 g 60 g 48 g	73 g 64 ± 7 g 103.5 g 37 g 66.5 g (includes melt) 0
Metallurgical findings on zircaloy oxidation characteristics	-Metallographic data	Essentially complete oxidation of previously molten zircaloy debris  High degree of oxidation of still-intact zircaloy cladding  Partial oxidation of fuel to a hyperstoichiometric condition (U <sub>4</sub> O <sub>9</sub> + UO <sub>2</sub> + )	Essentially complete oxidation of previously molten zircaloy debris  Partial oxidation of still-intact zircaloy cladding  No fuel oxidation
Partitioning of H <sub>2</sub> generation relative to onset of zircaloy melting/fuel dissolution at 2170 K	-Comparison of cladding thermocouple and H <sub>2</sub> generation data	~25-40% after onset of Zr/UO <sub>2</sub> dissolution	~84-86% after onset of Zr/UO <sub>2</sub> dissolution
Bundle reconfiguration characteristics	-Flow area of intact bundle -Metallographic examination minimum flow area	~32.8 cm <sup>2</sup> ~10.2 cm <sup>2</sup>	~32.8 cm <sup>2</sup> ~4.9 cm <sup>2</sup>

counter-current steam flow may tend to cause hydrodynamic breakup of relocating molten zircaloy, thereby delaying complete blockage or inducing an asymmetrical melt relocation/blockage configuration. Asymmetric bundle heatup conditions were also noted, that may induce corresponding asymmetry in zircaloy melt relocation. The fact that complete flow area blockage did not occur in the SFD-ST and SFD 1-1 tests does not prove that complete blockages in BWR fuel assemblies can never occur. Nevertheless, the SFD-ST and SFD 1-1 data do call into question the IDCOR assumption that complete flow area blockages always occur in BWRs upon melt relocation.

Evidence was also presented indicating that oxidation-driven heatup of a BWR assembly channel box can be expected to follow closely that of the fuel rod cladding, based upon a comparison of the SFD-ST and SFD 1-1 bundle liner versus cladding thermocouple measurements. The SFD metallographic examinations also indicate extensive failure of the zircaloy liner. The implications of the SFD test data are that survival of a BWR zircaloy channel box cannot be assured. These results contradict the IDCOR assumption that blockage of individual BWR assemblies would result in flow diversion and termination of H<sub>2</sub> production in degraded BWR fuel assemblies.



## REFERENCES

1. M. P. Sherman et al., *The Behavior of Hydrogen During Accidents in Light Water Reactors*, NUREG/CR-1561, SAND 80-1495, August 1980.
2. *Analysis of the Accident at TMI-2*, EPRI Report NSAC-80-1, March 1979.
3. B. G. Levi, "Cause and Impact of Chernobyl Accident Still Hazy," *Physics Today*, July 1986, pp. 17-21.
4. T. S. Kress, "The Chernobyl Accident Sequence," *Nuclear Safety*, 28, 1, January-March 1987, pp. 1-9.
5. W. R. Butler, C. G. Tinker, and L. S. Rubenstein, "Regulatory Perspective on Hydrogen Control for LWR Plants," *Proc. of the Workshop on the Impact of Hydrogen on Water Reactor Safety, Vol. 1, Albuquerque, NM, January 26-28, 1981*; NUREG/CP-2017, August 1981.
6. R. E. Henry, et al., "Evaluations of Hydrogen Generation During Core Heatup with an Intact Geometry," *Proc Intern. Mtg. on LWR Severe Accident Evaluation, Cambridge, MA, August 28-September 1, 1983*, TS 16.2.
7. J. R. Gabor and R. E. Henry, "The MAAP-BWR Severe Accident Analysis Code," *Proc. Intern. Mtg. on LWR Severe Accident Evaluation, Cambridge, MA, August 28-September 1, 1983*, TS-10.3.
8. J. T. Larkins and M. A. Cunningham, *Nuclear Power Plant Severe Accident Research Plan*, NUREG-0900, 1983.
9. M. Silberberg, et al, "The USNRC Severe Fuel Damage Research Program," *Proc. Intern. Mtg. Thermal Nuclear Reactor Safety, Chicago, IL, August 29-September 2, 1985*, pp. 1844-1853.
10. A. D. Knipe, S. A. Ploger, and D. J. Osetek, *PBF Severe Fuel Damage Scoping Test—Test Results Report*, NUREG-CR-4683, EGG-2413, August 1986.
11. Z. R. Martinson, D. A. Petti, and B. A. Cook, *PBF Severe Fuel Damage Test 1-1 Test Results Report*, NUREG/CR-4684, EGG-2463, October 1986.
12. P. Hofmann, *Transient Temperature UO<sub>2</sub>/Zry-4 Interaction Experiments Under Oxidizing Conditions*, KfK-2440, 1985.
13. P. Hofmann, H. J. Neitzel, "Experimental and Theoretical Results of Cladding Oxidation Under Severe Fuel Damage Conditions," *7th Intern. Conf. on Zirconium in the Nuclear Industry, Strasbourg, France, June 24-27, 1985*.
14. D. R. Olander, "Oxidation of UO<sub>2</sub> by High-Pressure Steam," *Nuclear Technology*, 74, August 1986, pp. 215-217.
15. D. W. Akers, *TMI-2 Core Debris Grab Samples: Examination and Analysis*, EGG-TMI-6853, 1985, pp. 75-76.
16. C. M. Allison, E. R. Carlson, and R. H. Smith, "SCDAP: A Computer Code for Analyzing Light Water Reactor Severe Core Damage," *Proceedings of the International Meeting on Light Water Reactor Severe Accident Evaluation, Cambridge, Massachusetts, August 28-September 1, 1983*.

17. A. Sharon, J. R. Gabor, and R. E. Henry, "Simulation of the Severe Fuel Damage Tests (SFD) Using the Modular Accident Analysis Program (MAAP)," *Proc. Intern. Mtg. on Thermal Reactor Safety, San Diego, CA, February 2-6, 1986*.
18. D. R. Olander, "Heat Effects in Zircaloy Oxidation by Steam," *J. Electrochem. Soc.*, **131**, 9, September 1986, pp. 2161-2169.
19. J. V. Cathcart and R. E. Pawel, *Zirconium Metal-Water Oxidation Kinetics: IV. Reaction Rate Studies*, ORNL-NUREG-17, August 1977.
20. V. F. Urbanic and T. R. Heidrick, "High-Temperature Oxidation of Zircaloy-2 and Zircaloy-4 in Steam," *J. Nucl. Mater.*, **75**, 1978, pp. 251-261.
21. L. Baker and L. C. Just, *Studies of Metal-Water Reactions at High Temperature: III. Experimental and Theoretical Studies of Zirconium-Water Reaction*, ANL-6548, 1962.
22. J. T. Prater and E. L. Courtright, *High Temperature Oxidation of Zircaloy-4 in Steam and Steam-Hydrogen Environments*, NUREG/CR-PNL-5558, September 1985.
23. J. T. Prater and E. L. Courtright, "Oxidation of Zircaloy-4 In Steam at 1300 to 2400°C," *Proceedings 7th International Conference on Zirconium in the Nuclear Industry, Strasbourg, France, June 24-27, 1985*.
24. D. R. Olander, "Oxidation of Liquid Zircaloy by Steam," *J. Nucl. Materials*, **119**, 1983, pp. 245-250.
25. M. S. El-Genk, "Molten Fuel Radial Motion and Cladding Melting during a PCM Event in LWRs," *J. Nucl. Engr. Design*, **54**, 1979, p. 349.
26. M. W. Mallett, W. M. Albrecht, P. R. Wilson, "The Diffusion of Oxygen in Alpha and Beta Zircaloy 2 and Zircaloy 3 at High Temperatures," *J. Electrochemical Society*, **(106)**, 1959, pp. 181-184.
27. R. E. Pawel, *Zirconium Metal-Water Oxidation Kinetics: Oxygen Diffusion in Oxide and Alpha Zircaloy Phases*, ORNL/NUREG-5, October 1976.
28. I. G. Ritchie and A. Atrens, "The Diffusion of Oxygen in Alpha-Zirconium," *J. Nucl. Mater.*, **67**, 1977, pp 254-264.
29. R. F. Domagala and D. J. McPherson, "System Zirconium-Oxygen," *Transactions of the American Institute of Mining, Metallurgical, and Petroleum Engineers*, **200**, 1954, pp 238-246.
30. R. A. Perkins, *Zirconium Metal-Water Oxidation Kinetic II, Oxygen-18 Diffusion in Beta-Zircaloy*, ORNL/NUREG/TM-10, July 1976.
31. C. J. Rosa and W. C. Hagel, "Oxygen-Ion Diffusivity in Hypostoichiometric  $ZrO_2$ ," *J. Nucl. Mater.*, **27**, 1968, pp 12-20.
32. T. Smith, "Diffusion Coefficients and Anion Vacancy Concentrations for the Zirconium-Zirconium Dioxide System," *J. Electrochemical Society*, **112**, 1965, p. 560.
33. P. Hofmann, D. K. Kerwin-Peck, "UO<sub>2</sub>/Zry Chemical Interactions under Isothermal and Transient Temperature Conditions," *J. Nucl. Mater.*, **124**, 1984, pp. 80-119.
34. A. W. Cronenberg, M. S. El-Genk, "An Assessment of Oxygen Diffusion during UO<sub>2</sub>-Zircaloy Interaction," *J. Nucl. Mater.*, **78**, 1978, pp. 390-407.

35. D. R. Olander, "The  $\text{UO}_2/\text{Zry}$ -Chemical Interactions," *J. Nucl. Mater.*, 115, 1983, pp. 271-285.
36. A. Sharon, "Comparison Between the PBF-SFD Fuel Bundle and a BWR Channel Behavior in Degraded Conditions," *Proc. 24th National Heat Transfer Conf.*, Pittsburgh, PA, August 9-12, 1987.
37. G. B. Wallis, *One-Dimensional Two-Phase Flow*, McGraw Hill, New York, 1969, pp. 336-338.
38. D. Lanning, N. Lombardo, and F. Panisko, *Full-Length High-Temperature Tests: Final Safety Analysis for FLHT-4 Experiment*, PNL-5869, August 1986.
39. R. Chambers, "Hydrogen Production and Core Damage Analysis of BWR High Pressure Boiloff," *Proc. 14th NRC Water Reactor Safety Research Information Meeting*, Gaithersburg, MD, October 27-30, 1986.
40. S. Hagen and P. Hofmann, "Behavior of  $\text{B}_4\text{C}$  Absorber Rods Under Severe Fuel Damage Conditions," *Proc. NRC Severe Fuel Damage Program Review Mtg.*, Rockville, MD, October 21-24, 1986.
41. A. W. Cronenberg, D. J. Osetek, and R. W. Miller, "Zircaloy Oxidation/Hydrogen Generation Behavior During Severe Accident Conditions," *Proc. 24th National Heat Transfer Conf.*, Pittsburgh, PA, August 9-12, 1987.



**APPENDIX A**  
**ILLUSTRATIVE CALCULATIONS**

## **APPENDIX A**

### **ILLUSTRATIVE CALCULATIONS**

Detailed calculations of various parameters used in the assessment of Tests SFD-ST and SFD 1-1 are given in Tables A-1 through A-5.

**Table A-1. Estimated steam-starvation height for the SFD-ST test conditions**

Governing Equations:

Assume no prior oxide layer buildup, so that the oxidation rate at a particular temperature can be expressed in terms of parabolic kinetics where

$$m_R = \text{mass zircaloy reacted} = A_R [k_p t]^{0.5}$$

$$dm_R/dt = \text{mass reaction rate} = A_R (k_p^{0.5}/2t^{0.5})$$

$$L = (dm_R/dt)(2t^{0.5}/k_p^{0.5})/NC$$

where

$A_R$  = NCL = surface area for reaction,  $\text{cm}^2$

$C$  = outside cladding circumference, cm

$N$  = number of reactive fuel rods

$L$  = steam starvation height, cm

$T$  = zircaloy temperature, K

$k$  = reaction rate constant,  $(\text{mg-Zr}/\text{cm}^2)^2/\text{s}$

Baker-Just =  $33.3 \text{ E} + 06 \exp(-45,500/1.987 T)$

Prater-Courtright =  $26.8 \text{ E} + 07 \exp(-52,350/1.987 T)$

$t$  = reaction time, s

Surface Area for Reaction:

Assume that zircaloy liner oxidation is small compared to that of the cladding, thus

$$A_R \sim 32 \text{ rods} \times (\pi \text{ OD}) \times L$$

$$\text{OD} = 9.63 \text{ mm} = 0.963 \text{ cm}$$

$$A_R = 96.8 (L) \text{ cm}^2$$

Calculation of  $m_R$ :

At the nominal makeup flow rate of 16.0 g/s, the equivalent Zr reaction rate is:

$$\frac{dm_R}{dt} = \left( \frac{16.0 \text{ g-H}_2\text{O}}{\text{s}} \right) \times \left( \frac{\text{mole-H}_2\text{O}}{18 \text{ g-H}_2\text{O}} \right) \times \left( \frac{1 \text{ mole-Zr}}{2 \text{ moles-H}_2\text{O}} \right) \times \left( \frac{91.2 \text{ g-Zr}}{\text{mole-Zr}} \right)$$

$$= 40.5 \text{ g-Zr reacted/s} = 40.5 \text{ E} + 03 \text{ mg-Zr/s}$$

Calculation of  $L$  ( $t = 1 \text{ s}$ ):

T (K)	Baker-Just		Prater-Courtright	
	$k_p [(\text{mg-Zr}/\text{cm}^2)^2/\text{s}]$	L (m) (at 1.0 s)	$k_p [(\text{mg-Zr}/\text{cm}^2)^2/\text{s}]$	L (m) (at 1.0 s)
1300	0.746	9.7	0.423	12.9
1500	7.810	3.0	6.310	3.3



**Table A-2. Estimated steam starvation height for the SFD 1-1 test conditions**

Governing Equations (see Table A-1):

$$m_R = \text{mass zircaloy reacted} = A_R [k_p t]^{0.5}$$

$$dm_R/dt = \text{mass reaction rate} = A_R (k_p^{0.5}/2t^{0.5})$$

$$L = (dm_R/dt)(2t^{0.5}/k_p^{0.5})/NC$$

Calculation of  $m_R$ :

At the nominal makeup flow rate of 0.64 g/s the equivalent Zr reaction rate is:

$$\begin{aligned} \frac{dm_R}{dt} &= \left( \frac{0.64 \text{ g-H}_2\text{O}}{\text{s}} \right) \times \left( \frac{\text{mole-H}_2\text{O}}{18 \text{ g-H}_2\text{O}} \right) \times \left( \frac{1 \text{ mole-Zr}}{2 \text{ moles-H}_2\text{O}} \right) \times \left( \frac{91.2 \text{ g-Zr}}{\text{mole-Zr}} \right) \\ &= 1.62 \text{ g-Zr reacted/s} = 1.62 \text{ E} + 03 \text{ mg-Zr/s} \end{aligned}$$

Calculation of L (t = 1 s):

T (K)	Baker-Just		Prater-Courtright	
	$k_p[(\text{mg-Zr}/\text{cm}^2)^2/\text{s}]$	L (m) (at 1.0 s)	$k_p[(\text{mg-Zr}/\text{cm}^2)^2/\text{s}]$	L(m) (at 1.0 s)
1300	0.746	0.39	0.423	0.51
1500	7.81	0.12	6.31	0.13

**Table A-3. Assessment of the differential pressure for steam removal capacity through a constricted orifice**

Governing Equation (Subsonic Flow):

$$\dot{m}_0/A_0 = \left(\frac{P_2}{P_1}\right)^{1/\gamma} \left\{ \frac{2\gamma}{\gamma-1} \rho_1 P_1 g_c \left[ 1 - \left(\frac{P_2}{P_1}\right) \right]^{(\gamma-1)/\gamma} \right\}^{1/2}$$

Parameter Values:

$$P_1 \sim P_2 = 1000 \text{ psi} = 6.895 \text{ E} + 07 \text{ dynes/cm}^2$$

$$P_1 = \text{saturated steam density at } P_1 = 0.036 \text{ g/cm}^3$$

$$\gamma = \text{steam isentropic exponent} = 1.25$$

$$g_c = 1.0 \text{ for cgs system (g-cm/s}^2 \text{ dynes)}$$

Calculation of Critical Pressure Ratio, F:

$$F = \left( \frac{2}{\gamma+1} \right)^{\gamma/(\gamma-1)} = (0.889)^{5.0} = 0.555 \text{ (subsonic flow)}$$

Calculation of Constants:

$$2\gamma/\gamma-1 = 10.0$$

$$\rho_1 P_1 g_c = 0.036 (6.895\text{E} + 7) (1) = 0.2482 \text{ E} + 7 \text{ g}^2/\text{s}^2 \text{ cm}^4$$

$$a_1 = 2(\gamma/\gamma-1) \rho_1 P_1 g_c = 2.482 \text{ E} + 7 \text{ g}^2/\text{s}^2 \text{ cm}^4$$

$$B = P_2/P_1$$

$$\dot{m}_0/A_0 = B^{1/\gamma} [a_1 (1-B^{\gamma-1/\gamma})]^{1/2}$$

Calculation:

<u>P (psi)</u>	<u>B = P<sub>2</sub>/P<sub>1</sub></u>	<u>B<sup>1/γ</sup> = B<sup>0.8</sup></u>	<u>B<sup>γ-1/γ</sup> = B<sup>0.2</sup></u>	<u><math>\dot{m}_0/A_0</math> (g/cm<sup>2</sup>s)</u>
1005.0	0.9950	0.9960	0.9990	157
1002.0	0.9980	0.9984	0.9996	100
1001.0	0.9990	0.9992	0.9998	70
1000.1	0.9999	0.9999	0.99998	22

**Table A-4. Estimate of the flooding conditions for breakup of a liquid zircaloy film**

Governing Equations:

$$D_c^5 = 16 \dot{m}^2 / \pi^2 \rho_l \rho_g g$$

$$V_f = [g D_c \rho_l / \rho_g]^{1/2}$$

Parameter Values

$$\rho_l = \text{molten zircaloy density} = 6.5 \text{ g/cm}^3$$

$$\rho_g = \text{saturated steam density at 6.9 MPa} = 0.036 \text{ g/cm}^3$$

$$g = \text{gravitation constant} = 980 \text{ cm/s}^2$$

$$\dot{m} = \text{nominal steam flow rate (g/s)}$$

$$D_c^5 = 1.65 \text{E-}03 \dot{m}^2 / \rho_l \rho_g = 7.069 \text{E-}03 \dot{m}^2$$

Computational Results

<u>Test</u>	<u><math>\dot{m}</math> (g/s)</u>	<u><math>D_c</math> (cm)</u>	<u><math>A_f = \frac{\pi}{4} D_c^2 \text{ (cm}^2\text{)}</math></u>	<u><math>V_f</math> (cm/s)</u>
SFD-ST	16.00	1.126	0.9957	446
SFD 1-1	0.64	0.311	0.0758	235



**Table A-5. Assessment of single-phase differential pressure for steam removal capacity through the constricted region of the SFD-ST bundle**

Governing Equation:

$$\dot{m}_0/A_0 = \left(\frac{P_2}{P_1}\right)^{1/\gamma} \left\{ \frac{2\gamma}{\gamma-1} \rho_1 P_1 g_c \left[ 1 - \frac{P_2}{P_1} \right]^{(\gamma-1)/\gamma} \right\}^{1/2}$$

Parameter Values:

$$\dot{m}_0 = 16 \text{ g/s}$$

$$A_0 = 0.9957 \text{ cm}^2 \text{ (Table A-4)}$$

$$P_1 \sim P_2 = 1000 \text{ psi} = 6.895(10^7) \text{ dy/cm}^2$$

$$\rho_1 = \text{saturated steam density at } P_1 = 0.036 \text{ g/cm}^3$$

$$\gamma = \text{isentropic exponent} = 1.25$$

Calculation of Constants:

$$2\gamma/\gamma-1 = 10.0$$

$$\rho_1 P_1 g_c = 0.036 (6.895 \text{ E} + 07) (1) = 0.2482 \text{ E} + 07 \text{ g}^2/\text{s}^2 \text{ cm}^4$$

$$(2\gamma/\gamma-1) \rho_1 P_1 g_c = 2.482 \text{ E} + 07 \text{ g}^2/\text{s}^2 \text{ cm}^4$$

$$B = P_2/P_1$$

$$a_1 = \dot{m}_0/A_0)^2 / (2\gamma/\gamma-1) P_1 \rho_1 g_c = 1.04 \text{ E} - 06$$

$$a_1 = B^{2/\gamma} [1 - B^{1/\gamma}] = B^{1.6} - B^{1.8}$$

Calculation:

$B = P_2/P_1$	$B^{1.6}$	$B^{1.8}$	$a_1$	$P_1 \text{ (psi)}$
0.99990	0.999840	0.999820	2.0 E-05	1000.10
0.99995	0.999920	0.999910	1.0 E-05	1000.05
0.99999	0.999984	0.999982	2.0 E-06	1000.01

**APPENDIX B**

**DISCUSSION OF FLOW PERTURBATIONS  
DURING THE SFD-ST TRANSIENT**

## APPENDIX B

### DISCUSSION OF FLOW PERTURBATIONS DURING THE SFD-ST TRANSIENT

Pressure and coolant flow variations occurred during the Severe Fuel Damage Scoping Test (SFD-ST) which could have affected overall bundle oxidation and attendant hydrogen generation behavior. The most significant thermal-hydraulic events occurred at the time of shroud failure (184 to 185 min) and relocation of molten material (204 to 206 min). The impact of these flow perturbations on steam supply to the bundle and attendant oxidation/hydrogen production characteristics is considered here.

#### Flow Perturbation from 184 to 185 Min

Figure B-1 compares the differential temperature in the bypass coolant and the output of the shroud melt-through detector, indicating shroud failure at about 184 min into the SFD-ST transient. At the time of shroud failure, a sharp reduction in the two-phase/steam interface elevation (based on fission chamber data) occurred, as shown in Figure B-2, indicating enhanced boiloff. Coolant flashing due to a temporary reduction in bundle pressure caused by shroud failure is considered the likely cause for enhanced boiloff. Such increased steaming resulted in temporary cooling of the bundle, as indicated by a drop in fuel rod temperatures as shown in Figure B-3. However, since the fuel rod temperatures were below 1900 K at this time, shroud failure and its attendant effects on bundle thermal-hydraulic behavior had little impact on overall hydrogen generation characteristics for the SFD-ST experiment. This is evident in Figure B-3, where thermocouple signals are shown to recover at a test time of about 185.5 min, with a subsequent rise in temperatures at later times when the oxidation process was accelerated at higher cladding temperatures. Likewise, the on-line hydrogen measurement, shown in Figure B-4, indicated no apparent alteration of the hydrogen release rate at 184 min. Thus, the flow perturbation at the time of shroud failure had essentially no impact on overall hydrogen generation behavior.

#### Flow Perturbation from 202 to 206 Min

Figure B-5 shows an overlay plot of the differential pressure measurement over the bundle length (via sensors located at the -0.3- and +1.77-m elevations), the separator pressure, and the inlet flow rate at a time just after shroud failure (184 to 185 min) until completion of the rapid cooldown phase. The bundle differential pressure is shown to steadily increase following shroud failure (184 min) until about 203 min. The differential pressure then decreased during the next minute before increasing again until reactor scram. The coolant inlet flow rate is shown to decrease slightly from about 0.02 L/s at 200 min to about 0.017 L/s at 204 min. The separator pressure is shown to increase gradually during the period 140 to 200 min, then increase more rapidly at about 203 min.

A probable explanation for the temporary flow reduction noted at the separator (at 204 min) is by activation of the pressure differential check valve upstream of the separator. As illustrated in Figure 1 (see Introduction), the steamline between the separator and condenser contains a pressure differential activated check valve, which prevents effluent flow-back into the bundle. This check valve had a set differential pressure of approximately 0.22 psi. A slight increase in separator differential pressure would have initiated check valve closure at 204 min, resulting in separator flow stagnation. If bundle blockage had occurred, then a sharp reduction in the bundle inlet flow would have been indicated; and steam flow through the bundle would have been cut off, thereby terminating oxidation-driven bundle heatup and hydrogen release. As shown in Figures B-4 and B-5, this was not the case. Thus, the most consistent postulate which accounts for flow stagnation to the separator, but does not violate other on-line measurements, is for check valve closure.



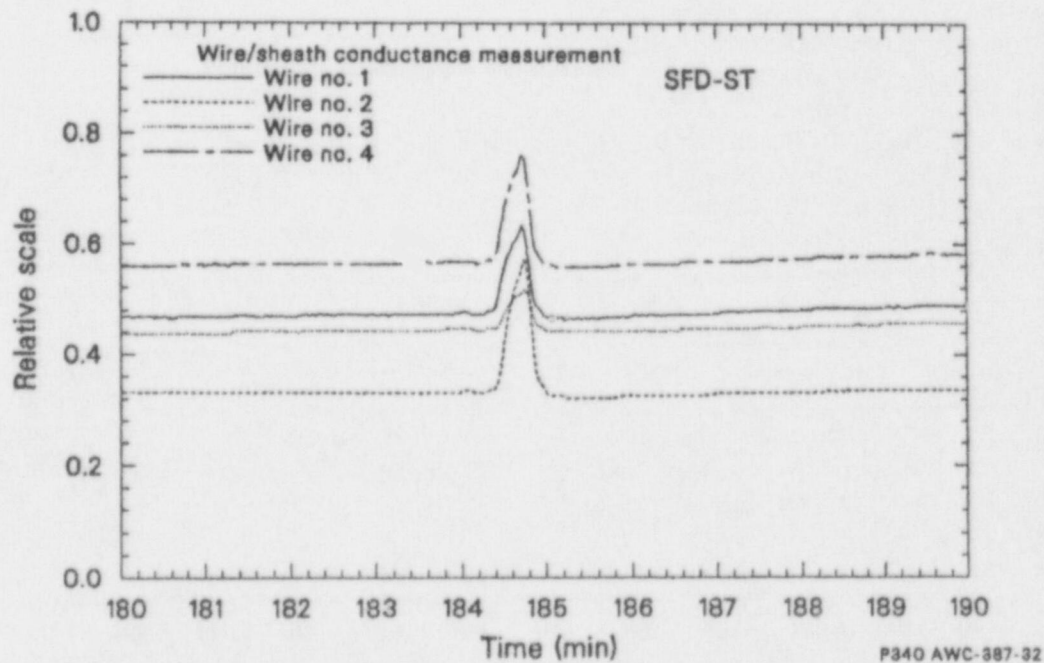
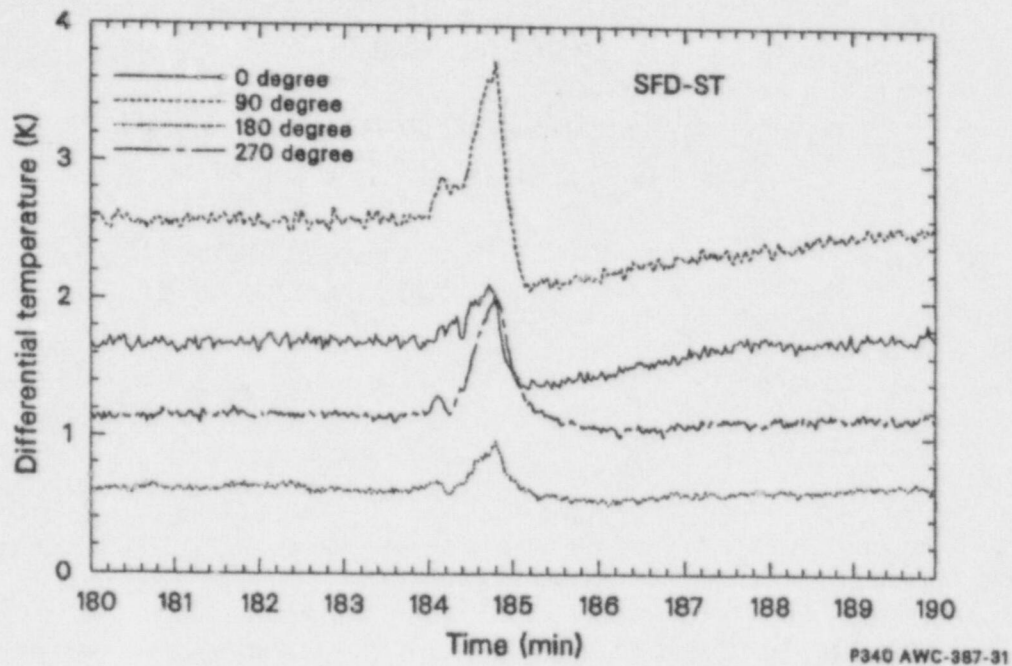


Figure B-1. Comparison of the SFD-ST bundle differential temperature and signal from melt-through detector.

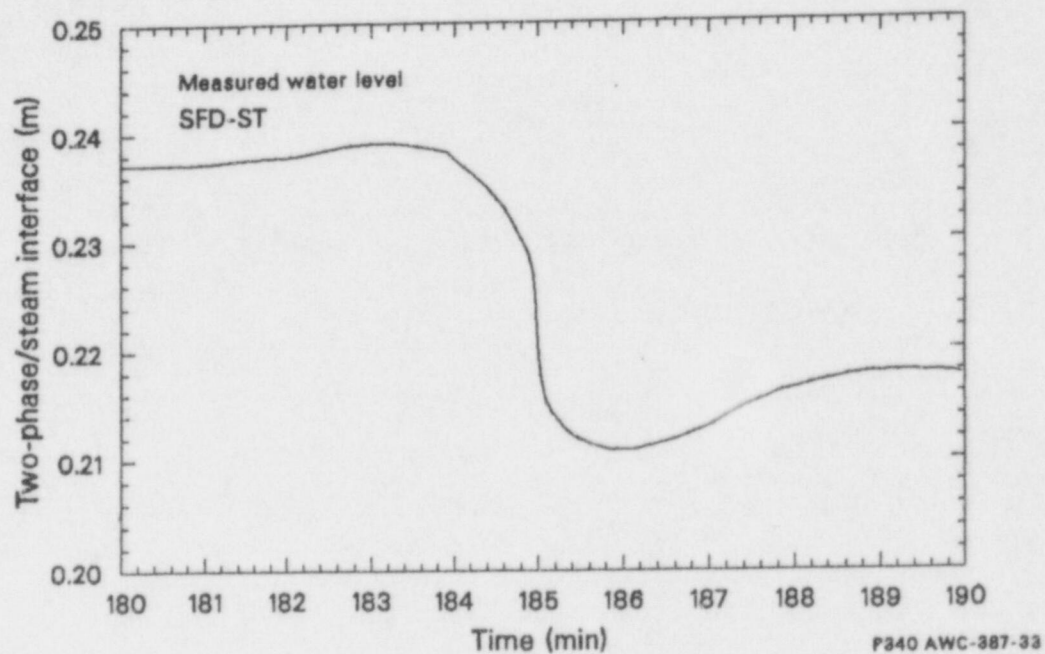


Figure B-2. The SFD-ST two-phase/steam interface level at the time of shroud failure.

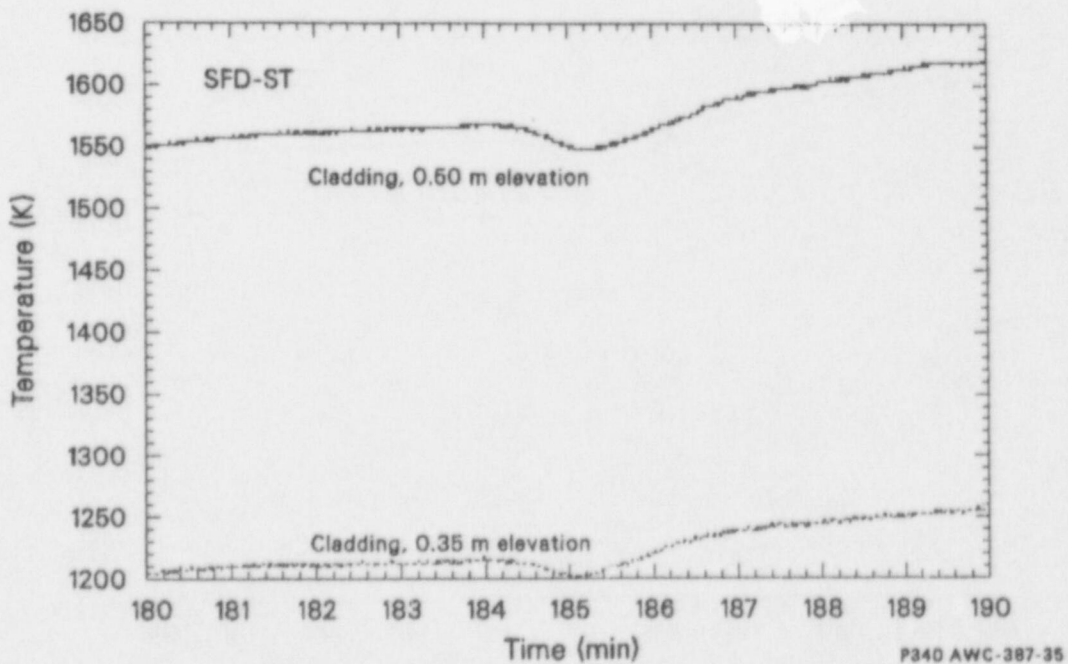
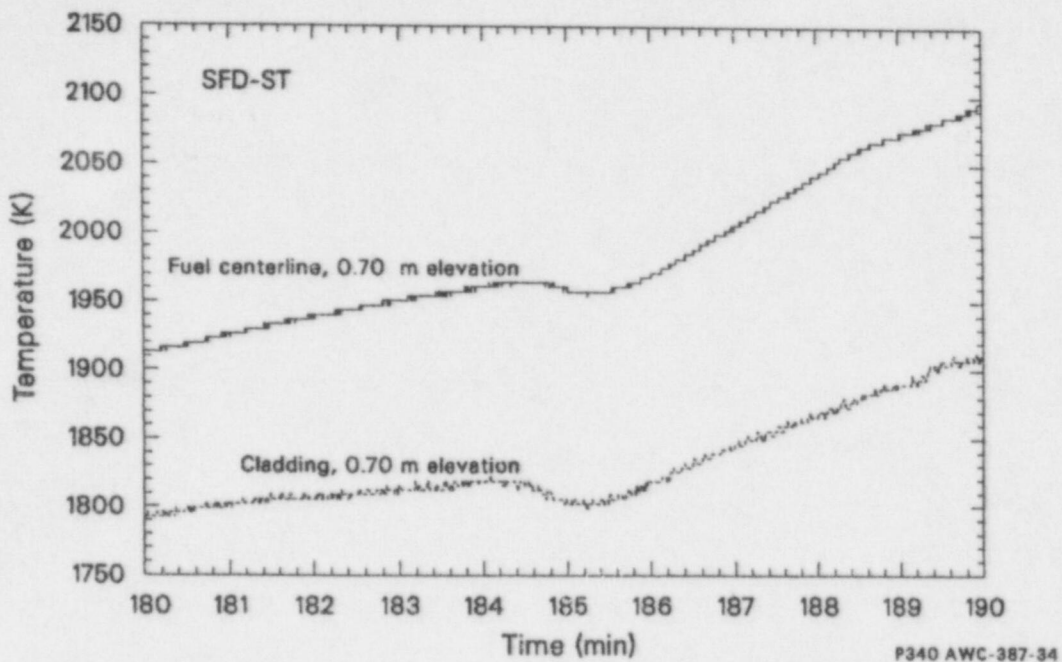


Figure B-3. SFD-ST Rod 3D thermocouple response at the time of shroud failure.



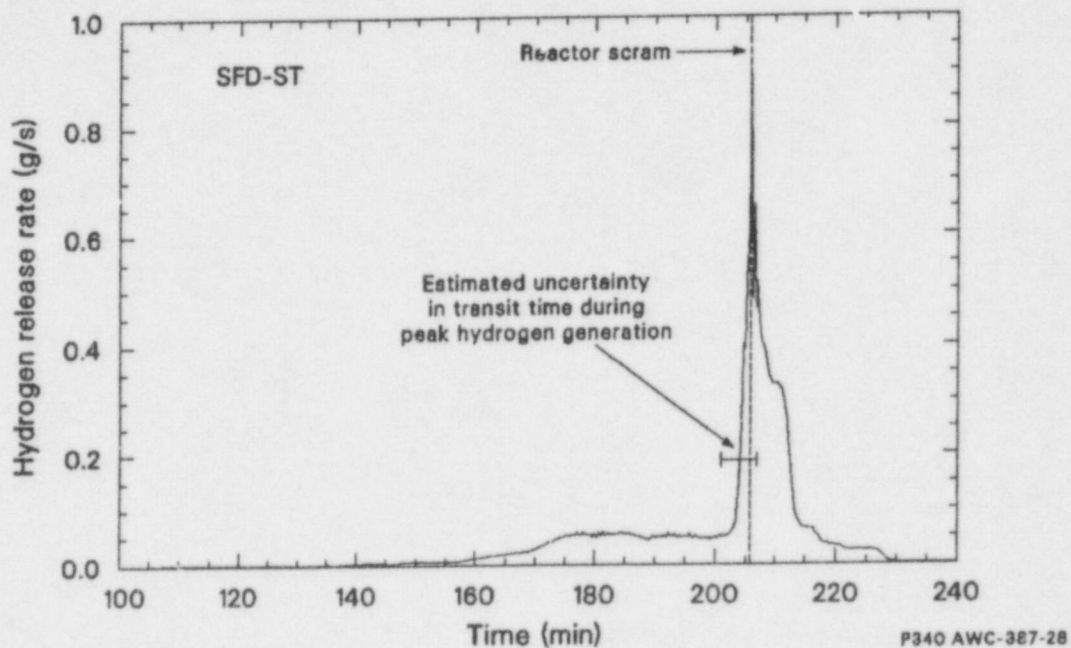


Figure B-4. SFD-ST measured on-line hydrogen release rate.

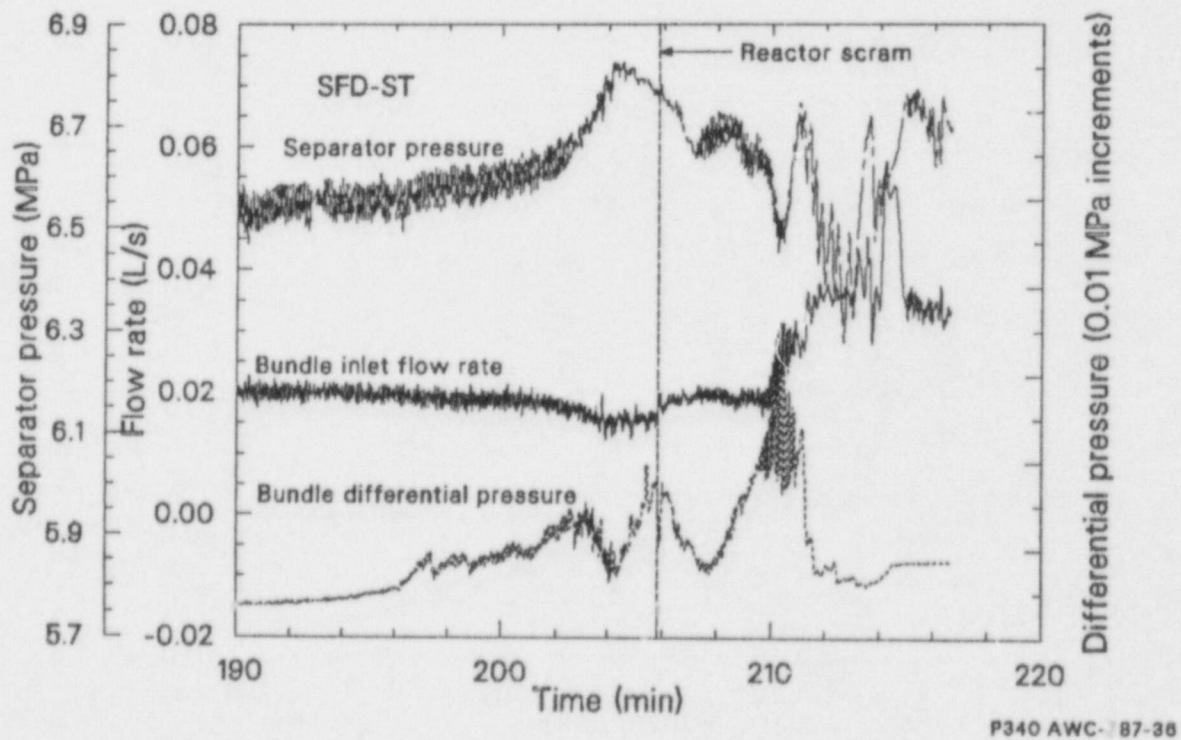


Figure B-5. Bundle differential pressure, inlet flow rate, and separator pressure during the final phase of the SFD-ST transient.

**APPENDIX C**  
**OXIDATION OF RELOCATED ZIRCALOY MELT**

## APPENDIX C

### OXIDATION OF RELOCATED ZIRCALOY MELT

As discussed in the main report, uncertainties exist relative to the oxidation behavior of molten zircaloy, particularly if breakout from the protective  $\text{ZrO}_2$  surface layer occurs. Here an attempt is made to assess oxidation rate behavior of relocated metallic  $\alpha\text{-Zr(O)}$  by steam.

Figure C-1 shows a section of a fuel rod where zircaloy clad melting has resulted in breakout of molten  $\alpha\text{-Zr(O)}$  and melt relocation at a lower elevation. The upper diagram in Figure C-1 depicts a fuel element at the time of zircaloy melting. It is assumed that a specified length ( $L$ ) of molten  $\alpha\text{-Zr(O)}$  relocates to the new configuration at a lower elevation (bottom of Figure C-1). The bulk of the resolidified melt consists of  $\alpha\text{-Zr(O)}$  containing the same concentration of oxygen that was contained in the  $\alpha\text{-Zr(O)}$  part of the cladding just prior to melting. The lower diagram in Figure C-1 depicts the reconfigured, previously molten  $\alpha\text{-Zr(O)}$  material as a refrozen annulus surrounding intact cladding. The reconfigured cladding presents a smaller surface area to the ambient steam, but oxidation continues due to exposure to steam. Neglected in the present analysis are the effects of dissolution of the  $\text{ZrO}_2$  shards carried by the relocating  $\alpha\text{-Zr(O)}$  melt and dissolution of the  $\text{ZrO}_2$  scale on the cladding originally at the relocation position.

Direct exposure of metallic  $\alpha\text{-Zr(O)}$  to steam will result in reestablishment of the protective  $\text{ZrO}_2$ , so that the oxygen diffusion problem, illustrated in Figure C-2, is quickly established. For this configuration, it is interesting to compare the growth rate of the  $\text{ZrO}_2$  oxide layer for different initial oxygen concentration conditions of the relocated  $\alpha\text{-Zr(O)}$  melt. In other words, a comparison is made of the  $\text{ZrO}_2/\alpha\text{-Zr(O)}$  interface velocity ( $V_\delta$ ) for different initial oxygen concentrations ( $C_0$ ) in the  $\alpha\text{-Zr(O)}$  layers. A rigorous solution to the diffusion problem presented in Figure C-2 can be obtained using the methodology outlined in References C-1 and C-2. However, for present purposes, a simplified approximation is adequate.

At the time of molten  $\alpha\text{-Zr(O)}$  relocation ( $t = 0$ ), the oxide skin thickness is zero, so that the instantaneous growth rate approaches infinity,

$$V_\delta = (d\delta/dt)_{t=0} = \infty \quad (\text{C-1})$$

Thus, a singularity exists at  $t = 0$ . Following the methodology outlined in Reference C-2, the short-time solution for  $\delta$  and  $V_\delta$ , however, can be approximated as:

$$\delta(t) = 2\lambda(D_2 t)^{0.5} \quad (\text{C-2})$$

$$V_\delta(t) = \lambda(D_2/t)^{0.5} \quad (\text{C-3})$$

where  $\lambda$  is the growth constant defined by the physical properties and boundary conditions of the problem. The above expression for  $\delta$  is analogous to the thermal penetration distance of a moving boundary solidification problem, where  $\lambda$  is similar to the dimensionless solidification constant. For the present problem, the dimensionless growth constant ( $\lambda$ ) is proportional to the ratio of the concentration conditions and diffusivities of the  $\text{ZrO}_2$  and  $\alpha\text{-Zr(O)}$  layers (see Reference C-2) and can be approximated as:

$$\lambda = \frac{(C_a - C_b)D_1^{0.5} + (C_c - C_0)D_2^{0.5}}{(C_b - C_c)D_2^{0.5}} = \frac{x + y}{z} \quad (\text{C-4})$$

where

$$x = (C_a - C_b) D_1^{0.5}$$

$$y = (C_c - C_0) D_2^{0.5}$$

$$z = (C_b - C_c) D_2^{0.5}$$

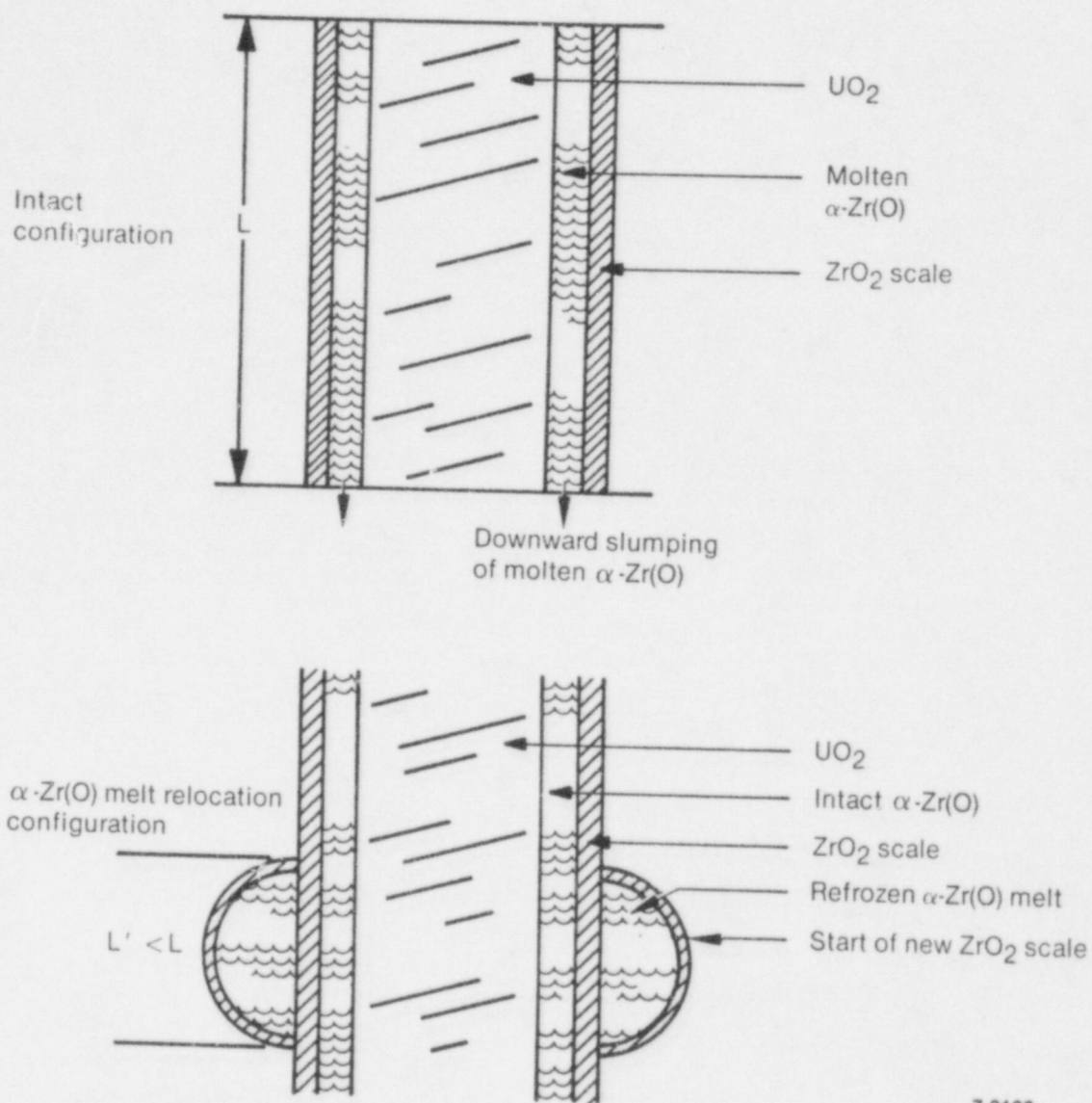
Equation C-4 can be expressed as the ratio of the growth constant ( $\lambda$ ) as a function of the fraction of oxygen saturation in  $\alpha\text{-Zr(O)}$ , that is as a function of  $C_0/C_c$ , i.e.,

$$\frac{\lambda}{\lambda_0} = \frac{x + y}{x + y_0} \quad (\text{C-5})$$

where the subscript zero denotes  $C_0 = 0$  (i.e., oxygen-free  $\alpha\text{-Zr}$ ).

Table C-1 presents calculational results at 1573 K and 1777 K, based on concentration values and diffusivities given in References C-1 and C-3.





7-3122

Figure C-1. Intact section of cladding before  $\alpha\text{-Zr(O)}$  melting and relocated refrozen  $\alpha\text{-Zr(O)}$  at lower elevation.

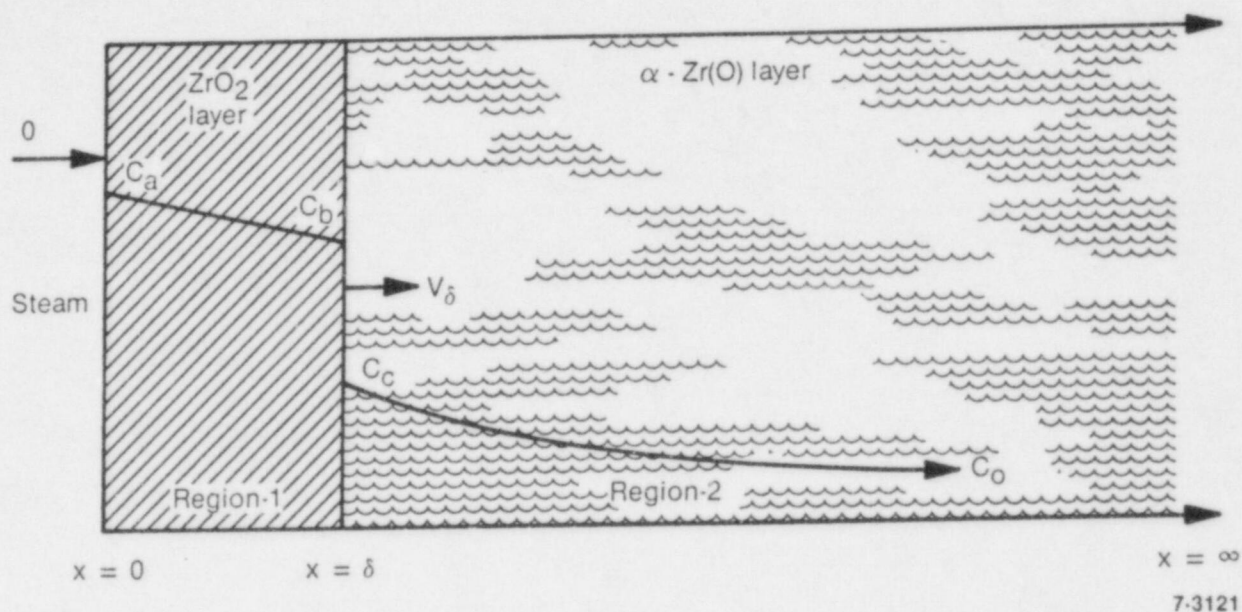


Figure C-2. Illustration of oxygen diffusion problem for oxidation of relocated  $\alpha$ -Zr(O).

Table C-1. Evaluation of the effect of oxygen content on the growth rate constant

Property Values:

$C_a$	=	0.094 atom-O/cm <sup>3</sup> (Ref. C-1)
$C_b$	=	0.086 atom-O/cm <sup>3</sup> (Ref. C-1)
$C_c$	=	0.029 atom-O/cm <sup>3</sup> (Ref. C-1)
$D_1(1573 \text{ K})$	=	2.0 E-06 cm <sup>2</sup> /s (Ref. C-1)
$D_2(1573 \text{ K})$	=	3.2 E-07 cm <sup>2</sup> /s (Ref. C-1)
$D_1(1777 \text{ K})$	=	7.75 E-06 cm <sup>2</sup> /s (Ref. C-3)
$D_2(1777 \text{ K})$	=	2.04 E-06 cm <sup>2</sup> /s (Ref. C-3)

Calculated Results:

$C_0$	$C_0/C_c$	$\lambda/\lambda_0$ (1573 K)	$\lambda/\lambda_0$ (1777 K)
0.0	0.0	1.00	1.00
0.0145	0.5	0.70	0.68
0.029	1.0	0.41	0.35

The predicted results indicate that the effect of prior oxygen content of the relocated  $\alpha$ -Zr(O) is small. For example, at 1573 K a 50% saturation condition ( $C_0/C_c = 0.5$ ) yields a growth rate constant that is approximately 70% of that for zero initial oxygen in the relocated  $\alpha$ -Zr(O) melt. Even for fully saturated  $\alpha$ -Zr(O) ( $C_0/C_c = 1$ ), the growth rate is indicated to be 40% of that for oxygen-free zircaloy. The same trend is noted using diffusivity

values given in Reference C-3 at 1777 K. Although the methodology employed is an approximation to a complex diffusion problem with a nonlinear boundary condition, it nevertheless illustrates that breakout and relocation of  $\alpha$ -Zr(O) melt from the protective  $ZrO_2$  layer can be expected to result in oxidation kinetics similar to that of relatively oxygen-free zircaloy until a new  $ZrO_2$  protective layer is established.

## References

- C-1. D. R. Olander, "Heat Effects in Zircaloy Oxidation by Steam," *J. Electrochem. Soc.*, 131, 9, September 1984, pp. 2161-2169.
- C-2. A. W. Cronenberg and M. J. El-Genk, "An Assessment of Oxygen Diffusion During  $UO_2$ -Zircaloy Interaction," *J. Nucl. Mater.*, 78, 1978, pp. 390-407.
- C-3. R. E. Pawel, *Zirconium Metal-Water Oxidation Kinetics: Oxygen Diffusion in Oxide and Alpha Zircaloy Phases*, ORNL/NUREG-5, 1976.



NRC FORM 335 (2-84) NRCM 1102 3201, 3202 SEE INSTRUCTIONS ON THE REVERSE		U.S. NUCLEAR REGULATORY COMMISSION <b>BIBLIOGRAPHIC DATA SHEET</b>		1. REPORT NUMBER (Assigned by TDC add Vol. No. if any) NUREG/CR-4866 EGG-2499	
2. TITLE AND SUBTITLE An Assessment of Hydrogen Generation for the PBF Severe Fuel Damage Scoping and 1-1 Tests				3. LEAVE BLANK	
5. AUTHOR(S) August W. Cronenberg, Richard W. Miller, Daniel J. Osetek				4. DATE REPORT COMPLETED MONTH: April YEAR: 1987 6. DATE REPORT ISSUED MONTH: April YEAR: 1987	
7. PERFORMING ORGANIZATION NAME AND MAILING ADDRESS (Include Zip Code) EG&G Idaho, Inc. Idaho Falls, ID 83415				8. PROJECT/TASK/WORK UNIT NUMBER 9. FUND OR GRANT NUMBER A6321	
10. SPONSORING ORGANIZATION NAME AND MAILING ADDRESS (Include Zip Code) U.S. Nuclear Regulatory Commission Washington, D. C. 20555				11a. TYPE OF REPORT Research b. PERIOD COVERED (Inclusive dates)	
12. SUPPLEMENTARY NOTES					
13. ABSTRACT (200 words or less) <p>An evaluation of zircaloy oxidation and hydrogen generation data is presented for the first two severe fuel damage (SFD) tests, SFD-ST and SFD 1-1, conducted in the PBF at the INEL. The report presents an assessment of data in terms of the influence of zircaloy melting on oxidation behavior and fuel bundle reconfiguration effects which may alter steam flow and hydrogen generation characteristics.</p> <p>A comparison of the H<sub>2</sub> generation and cladding thermocouple data indicates that a significant amount of hydrogen was produced after the initiation of zircaloy melt-induced fuel dissolution (<math>\geq 2150</math> K). Posttest metallographic observations corroborate the trend of the on-line data. Analyses also indicate that essentially complete flow area blockage (&gt;98%) would be required to diminish steam flow through the degraded test bundle, reducing hydrogen production. Neither on-line data nor posttest examination of the SFD-ST and SFD 1-1 fuel bundles indicates that such extreme flow area blockages occurred.</p> <p>For the steam-rich SFD-ST experiment, UO<sub>2</sub> fuel oxidation was also observed, possibly accounting for ~20% of the total hydrogen production. Fuel oxidation has also been noted from retrieved TMI-2 core debris samples. Thus, oxidation of UO<sub>2</sub> to a hypostoichiometric condition may add to the total hydrogen burden for severe accidents.</p>					
14. DOCUMENT ANALYSIS - KEYWORD DESCRIPTORS PBF, SFD-ST, SFD 1-1, hydrogen generation				15. AVAILABILITY STATEMENT	
16. IDENTIFIERS (OPEN ENDED TERMS)				16. SECURITY CLASSIFICATION (This page) Unc1. (This report) Unc1.	
				17. NUMBER OF PAGES	
				18. PRICE	

120559078877 1 1AN1R3  
US NRC-BARM-ADM  
DIV OF PUB SVCS  
POLICY & PUB MGT BR-PDR NUREG  
#-501  
WASHINGTON DC 20555

**EG&G Idaho**  
**P.O. Box 1625**  
**Idaho Falls, Idaho**  
**83415**